Development of Micromachined Field Ionization Tips for Use As An Integrated Gas Detector In a Micromachined Gas Chromatography System

By

Bahram Ghodsian

B.ENG. in Electronic and Electrical Engineering (Hons.)
University of London, U.K., 1991

M.A.Sc. in Electrical Engineering,
University of British Columbia, Canada, 1993

A THESIS SUBMITTED IN PARTIAL FULFILLMENT OF

THE REQUIREMENTS FOR THE DEGREE OF

DOCTOR OF PHILOSOPHY

in the

SCHOOL OF ENGINEERING SCIENCE

© Bahram Ghodsian

SIMON FRASER UNIVERSITY

December 1997

All rights reserved. This work may not be
reproduced in whole or in part, by photocopy or
other means, without permission of the author.

National Library of Canada

Acquisitions and Bibliographic Services

395 Wellington Street
Ottawa ON K1A 0N4
Canada

Bibliothèque nationale du Canada

Acquisitions et services bibliographiques

395, rue Wellington
Ottawa ON K1A 0N4
Canada

Your file Votre référence

Our file Notre référence

The author has granted a non-exclusive licence allowing the National Library of Canada to reproduce, loan, distribute or sell copies of this thesis in microform, paper or electronic formats.

L'auteur a accordé une licence non exclusive permettant à la Bibliothèque nationale du Canada de reproduire, prêter, distribuer ou vendre des copies de cette thèse sous la forme de microfiche/film, de reproduction sur papier ou sur format électronique.

The author retains ownership of the copyright in this thesis. Neither the thesis nor substantial extracts from it may be printed or otherwise reproduced without the author's permission.

L'auteur conserve la propriété du droit d'auteur qui protège cette thèse. Ni la thèse ni des extraits substantiels de celle-ci ne doivent être imprimés ou autrement reproduits sans son autorisation.

0-612-37704-0

Canada

Approval

Name: Bahram Ghodsian

Degree: Doctor of Philosophy

Title: Development of Micromachined Field Ionization Tips for Use As An Integrated Gas Detector In a Micromachined Gas Chromatography System

Chairman: Professor Mehrdad Saif

Professor Marek Syrzycki
Senior Supervisor
School of Engineering Science, SFU

Professor M. (Ash) Parameswaran
Senior Supervisor
School of Engineering Science, SFU

Professor Sandy Robinson
Committee Member
Department of Elect. & Comp. Eng.,
University of Alberta

Professor Andrew Rawicz
Internal Examiner
School of Engineering Science, SFU

Professor Andrzej Barwicz
External Examiner
Département de Génie Electrique,
Université du Québec á Trois-Riviéres

December 22nd, 1997

PARTIAL COPYRIGHT LICENSE

I hereby grant to Simon Fraser University the right to lend my thesis, project or extended essay (the title of which is shown below) to users of the Simon Fraser University Library, and to make partial or single copies only for such users or in response to a request from the library of any other university, or other educational institution, on its own behalf or for one of its users. I further agree that permission for multiple copying of this work for scholarly purposes may be granted by me or the Dean of Graduate Studies. It is understood that copying or publication of this work for financial gain shall not be allowed without my written permission.

Title of Thesis/Project/Extended Essay

Development of Micromachined Field Ionization Tips for Use As An Integrated Gas Detector In a Micromachined Gas chromatography System

Author: ______________________
(signature)

Bahram Ghodsian
(name)

31 December 1997
(date)

Abstract

This thesis explores the design, fabrication and testing of miniature gas analysis system using the principles of gas chromatography (GC). Microfabrication techniques and micromachining processes were used to build a prototype gas detector. The work done in this thesis can be classified into two parts: (a) the miniaturization of the gas detectors for use in a miniaturized GC system, and (b) development of a low-cost fabrication method, with the ultimate goal of monolithic integration with a micromachined GC system.

The gas detector proposed in this thesis operates on the principle of field ionization, which has been shown to be applicable for the detection of gases at atmospheric pressure. An electric field is used to ionize the sample gas and generate ionic current. This current is next measured to identify the presence and the concentration of the sample gas. The high electric field necessary for detector operation is achieved by the use of very small distances between field ionization tips and a counter electrode. In this thesis, we have proposed, designed, fabricated and developed a field ionization gas detector: using only standard fabrication processes and a sub-millimeter-resolution mask, we produced self-aligned field ionization tips separated from the counter electrode by a micrometer or sub-micrometer gap.

An experimental study was undertaken to test and characterize the proposed detector. The research results show that: (a) the class of gases that can be detected using the proposed detector encompasses gases with large ionization coefficients (>1.75 x 10^{-5} for acetic acid). Gases with a small ionization coefficient, for example nitrogen dioxide, can be detected in the presence of water vapor. (b) the minimum detectable concentration

level in the case of acetic acid was 14 ppm. (c) the minimum applied voltage required to detect acetic acid at 14 ppm was 5 V.

Acknowledgments

I would like to thank my parents and my two sisters; Maryam and Marjan, for their ultimate patience, support, understanding and encouragement throughout the years, specially during the course of this work. It was their encouragement that helped me to pursue a career in engineering. I would like to express my sincerest gratitude to my two senior supervisors, Professor M. (Ash) Parameswaran and Professor M. Syrzycki for their generous financial support and guidance during the course of this work. Their guidance kept me on the path of micromachining when I was tempted to stray off to VLSI, and their dedication to their profession exemplifies those qualities which I would most like to emulate. A special note of thanks to my co-supervisor Professor Sandy Robinson and members of the micromachining and microfabrication group, Dr. Ewa Czyzewska for her continuous assistance and patience in the cleanroom, Mr. Bill Woods for performing most of the metal deposition steps, Dr. Albert Curzon (from the Department of Physics) for taking the SEM micrographs. There are a number of other people in the School of Engineering Science to whom I am indepted, in particular, Brigitte Rabold, graduate secretary, and Marilyn Prouting for their continuous administration assistance. I would also like to thank my past and present friends at SFU who made the life very enjoyable on campus (in no particular order), Ali Faraz, Sasan Naseh, Vikas Gupta, Jessica Melin, Robert Sobot, Manish Mehta, Taranjit Singh, Benoit Dufort, Dr. Krishna and Janifer Busawon, Kirthi Roberts, Dr. Javad Dargahi, Paris Polydoro, Pirongrang Ramasoota, Jianming Chen, Edward Leung, Madjid and Mahsa Nakhjiri. And, finally, I thank my lovely wife, Mana (aziz-e dellam), for her patience and tolerance during this work.

Dedications

I would like to dedicate this thesis to following people:

- my parents,

- my sisters Maryam and Marjan,

- and last but not least to my lovely wife, Mana.

Table of Contents

Approval ii

Abstract iii

Acknowledgments v

Dedications vi

Table of Contents vii

List of Acronyms xiii

List of Symbols xiv

List of Tables xv

List of Figures xvi

CHAPTER 1

Introduction 1

1•1 Chemical Transducers 4

1•1•1 Electrochemical Detectors 6

1•1•1•1 Amperometric Detector 6

Fuel Cell Sensor 7

1•1•1•2 Conductimetric Detector 8

Metal Oxide Semiconductor Gas Detectors 8

1•1•1•3 Potentiometric Detector 11

ChemFETs 12

1•1•2 Thermal Detectors 13

1•1•3 Sensors Based on Wave Motion 14

1•1•3•1 Optical Detectors 14

1•1•3•2 Surface Acoustic Wave Devices 14

1•2 Problems with Micro-Gas-Detectors 16

1•2•1 Selectivity 16

1•2•2 Stability 17

1•2•3 Reproducibility 17

1•2•4 Cost 17

1•3 Research Motivations 18

1•4 Research Objectives 19

1•4•1 Detector Miniaturization 19

1•4•2 Low-Cost and Reproducible Fabrication Method 21

1•5 Research Methodology 21

1•6 Thesis Overview 22

CHAPTER 2

Gas Chromatography Detectors 23

2•1 Fundamentals of Gas Chromatography 25

2•2 Detectors and their Principles of Operation 26

2•2•1 Flame Ionization Detector 27

2•2•2 Ionization Gauge Detector 29

2•2•3 Thermal Conductivity Detector 31

2•2•4 Electron Capture Detector 33

2•2•5 Atomic Emission Detector (AED) 34

2•2•6 Helium and Argon Ionization Detector 36

2•2•7 Photoionization Detector 36

2•2•8 Flame Photometric GC Detector 38

2•2•9 Hall Electrolytic Conductivity Detector (HECD) 39

2•3 Biological Detectors 40

2•4 Summary 45

CHAPTER 3

Principle of Field Ionization 46

3•1 Theory of Field Ionization 47

3•1•1 Field Emission 47

3•1•2 Field Ionization 48

3•2 Field Ionization Current 51

3•2•1 Diffusion-Limited Electrode Reaction 51

3•2•2 Electron-Transfer-Limited Electrode Reaction 52

3•3 Summary 58

CHAPTER 4

Micromachining Processes 59

4•1 Micromachining 59

4•1•1 Anisotropic Etching 61

4•2 Anisotropic Etching Profile 68

4•2•1 Inverted Pyramid 68

4•2•2 Feedthrough Feature 69

4•2•3 Inverted Truncated Pyramid 70

4•3 Plating 71

4•3•1 Electroplating Versus Electroless Plating Process 72

4•3•2 Electroplating Process 73

4•3•2•1 Photoresist Mold 77

4•3•2•2 Seed Layer 78

4•3•2•3 Electrolyte 78

4•4 Counter Electrode Epoxy Bonding 80

4•5 Summary 81

CHAPTER 5

Design and Fabrication of Micromachined Field Ionization Tips 82

5•1 The Commonly Used Fabrication Processes 82

5•2 Micromachined Tip's Fabrication Process 90

5•2•1 Mask Design and Preparation 90

5•2•2 Design and Fabrication Phase .94

5•2•2•1 An Alternative Fabrication Process 113

5•2•3 Assembly Phase 120

5•2•3•1 Input and Exhaust Manifolds 120

5•2•3•2 Electrical Connection 120

5•2•3•3 Counter Electrode-to-Wafer Bonding 121

5•2•3•4 Packaged Device 122

5•3 Summary 126

CHAPTER 6

Characterization of Micromachined Field Ionization Detector 127

6•1 Experimental Setup 127

6•1•1 Gas Generation and Delivery System 128

6•1•2 Carrier Gas 130

6•1•3 Sample Gases 130

6•1•3•1 Calculation 132

Concentration 132

Temperature Change 132

6•1•3•2 Magnetic Actuated 3-Way Valve 134

6•1•3•3 Semiconductor Parameter Analyzer 134

6•2 Steady-State Response of the Detector 135

6•2•1 Gas Generation/Delivery System Concentration 135

6•2•1•1 Concentration Test Procedure 136

6•2•1•2 Acetic Acid Response 137

6•2•1•3 Nitroge Oxide and Ammonia Response ...138

6•2•2 Applied Voltage Dependence 142

6•2•2•1 Test Procedure 142

6•2•2•2 Acetic Acid Response 143

6•2•2•3 Nitrogen Oxide and Ammonia .. Response 146

6•3 Discussion of the Results 146

6•4 Summary 150

CHAPTER 7

Conclusions and Recommendations for Future Research 151

7•1 Conclusions 151

7•2 Summary of Contributions 153

7•3 Further Research 153

APPENDIX A

Microfabrication Processes 154

A•1 RCA Cleaning 154

A•2 Thermal Oxidation 154

A•3 Boron Diffusion 155

A•4 Oxide Etch 156

A•5 Photolithography Process 156

A•6 Sputtering 157

A•7 EDP Etching 158

A•8 TMAH Etching 158

A•9 Metal Etching 159

APPENDIX B

Non-Linear Least-Square Fit 160

B•1 Fitting Function 160

B•1•1 Response Function 161

B•2 MATLAB Source Code 163

References 165

List of Acronyms

SAW	Surface Acoustic Wave
FET	Field Effect Transistor
GC	Gas Chromatography
FID	Flame Ionization Detector
IGD	Ionization Gauge Detector
TCD	Thermal Conductivity Detector
ECD	Electron Capture Detector
AED	Atomic Emission Detector
CSD	Cross Section Detector
PID	Photoionization Detector
IP	Ionization Potential
FPD	Flame Photometric Detector
PMT	Photomultiplier Tube
IR	Infrared
HECD	Hall Electrolytic Conductivity Detector
MEMS	Microelectromechanical Systems
EAD	Electroantennography Detector
IC	Integrated Circuits
EDP	Ethylenediammine Pyrocatechol
TMAH	Tetramethylammonium Hydroxide
KOH	Potassium Hydroxide
RIE	Reactive Ion Etching
CVD	Chemical Vapor Deposition
LPCVD	Low-Pressure Chemical Vapor Deposition
PECVD	Plasma Enhanced Chemical Vapor Deposition
BOE	Buffered Oxide Etch
SEM	Scanning Electron Microscope

List of Symbols

$q\phi$	Work function of metal
qV_I	Ionization energy
E_F	Fermi level
D_{water}	Water diffusion coefficient
D_{oxygen}	Oxygen diffusion coefficient
E	Energy level
E_{ox}	Oxidation energy level
E_{red}	Reduction energy level
$N(E)$	Density of levels
W	Energy
k	Boltzman constant
T	Absolute Temperature in Kelvin
q	Electron charge in coulomb
λ	Reorganization energy
α	Constant related to tunneling distance
i_a	Anodic current
i_c	Cathodic current
i_{net}	Net current
c	Gas concentration
V_{redox}	Redox potential
V_{app}	Applied Voltage
η	Overvoltage
f_a	Angle between two crystal plane
d_p	Pit depth
W_m	Masking width
W_{bottom}	Width at the bottom of a truncated pyramid
W_{hole}	Width of the hole in a feedthrough feature
T_w	Wafer thickness
R_f	Seed layer resistance
ρ_s	Seed layer resistivity
t_s	Seed layer thickness
C	Sample gas concentration
W_a	Atomic Mass
F_c	Flow rate
R	Permeation Rate

List of Tables

Table 1.1 : Global environmental problems and related gases. 1

Table 1.2 : Comparison between analytical instruments and micromachined detectors. . 2

Table 2.1 : Gases with little or no response to the FID. 29

Table 4.1 : Planer density properties of the major silicon planes 62

Table 4.2 : Etch rate of silicon as a function of the water content of the etch, with the pyrocatechol content held constant 65

Table 4.3 : Approximate silicon (100) etch rates (μm/h) for various boron dopants and temperatures. 66

Table 4.4 : Ratio of the (100) Si/SiO_2 etch rate as a function of temperature 67

Table 4.5 : Comparison of electroplating versus electroless plating. 72

Table 4.6 : Electroplating seed layer material, resistivity and typical thickness. 79

Table 4.7 : : Electroplating bath solution for Ni alloy at 50°C. 79

Table 4.8 : Electroplating bath solution for Ni-Fe alloy at 50°C. 80

Table 6.1 : The specific constants for the permeation tube of sample gases. The number in brackets for temperature specifies the maximum applied temperature recommended by the manufacture. 133

Table 6.2 : Inactive and active atmospheric impurities. 147

Table 6.3 : Selected values of aqueous and their ionization constants at 25°C. 149

List of Figures

Figure 1.1 : Odour recognition in a biological system with typical steps in the signal transduction. . . . 3

Figure 1.2 : Odour recognition in electronic system with typical steps in the signal transduction. . . . 4

Figure 1.3 : Classification of chemical detectors. . . . 5

Figure 1.4 : Schematic diagram of fuel cell detector. . . . 7

Figure 1.5 : Schematic representation of a metal oxide semiconductor gas detector. . . . 9

Figure 1.6 : Typical preparation steps for SnO_2 paste, used as a thick film 9

Figure 1.7 : A micromachined version of metal-oxide-semiconductor gas detector . . . 10

Figure 1.8 : A typical ChemFET. . . . 12

Figure 1.9 : A micromachined thermal conductivity gas detector. . . . 13

Figure 1.10 : Simplified diagram of a SAW 15

Figure 2.1 : Schematic diagram of a gas chromatography system 25

Figure 2.2 : Some of the detectors' sensitivity range 26

Figure 2.3 : Schematic diagram of a flame ionization detector 28

Figure 2.4 : An ionization gauge 30

Figure 2.5 : (a) Standard Thermal Conductivity Detector (TCD) and (b) a Wheatstone Bridge configuration 32

Figure 2.6 : An Electron Capture Detector (ECD) 33

Figure 2.7 : A gas chromatographic atomic emission detector 35

Figure 2.8 : A gas chromatographic photoionization detector. . . . 37

Figure 2.9 : A gas chromatographic flame photometric detector 38

Figure 2.10 : Illustration of the moth with the attached MEMS probe. . . . 40

Figure 2.11 : (a) Schematic representation of the experimental setup, (b) the packaged biological detector with an amplifier 41

Figure 2.12 : Detector response to one female Processionary moth 42

Figure 2.13 : (a) A SEM picture of a MEMS probe's tip, (b) and the actuation system 43

Figure 3.1 : Schematic representation of the field ionization process. 48

Figure 3.2 : The energy diagram of an atom in proximity of metal 50

Figure 3.3 : The band model for the metal/analyte interface with one-electron in equilibrium 52

Figure 3.4 : The band model for the metal/analyte interface with metal electrode and analyte in non-equilibrium 55

Figure 3.5 : The band model for the metal/analyte interface with metal electrode and the analyte in non-equilibrium 56

Figure 4.1 : The etching profile for: (a) (100) oriented silicon anisotropic etch, (b) (110) oriented silicon anisotropic etch and, (c) silicon isotropic etch 61

Figure 4.2 : Miller indices of important silicon crystal planes with lattice constant 'a' 62

Figure 4.3 : The rate of silicon in EDP versus temperature.. 64

Figure 4.4 : Silicon {100} etch rate in EDP versus boron concentration for a few different temperatures.. 66

Figure 4.5 : Cross-section view of a typical inverted pyramidal pit. 69

Figure 4.6 : Cross-section of a typical feedthrough feature etch 70

Figure 4.7 : Cross-section of a typical inverted truncated pyramid feature etch 71

Figure 4.8 : A Simplified plating cell. 74

Figure 4.9 : Non-uniform current densities. 75

Figure 4.10 : Uniform current density 75

Figure 5.1 : The cross-sectional views of the fabrication sequence of the self-aligned tip formation process by Spindt *et al.* 84

Figure 5.2 : The cross-sectional views of a field ionization tip structure fabricated by the photolithographic process 86

Figure 5.3 : The sectional views of a field ionization tip structure fabricated according to an anisotropic process 87

Figure 5.4 : The sectional views of field ionization tip structure fabricated according to an isotropic process 88

Figure 5.5 : The sectional views of a field ionization tip structure fabricated according to a conventional photolithographic process. 89

Figure 5.6 : Photolithographic mask design used for the first EDP etch to create pits on the bottom surface of the silicon wafer. 91

Figure 5.7 : Photolithographic mask design used for the second EDP etch from the top surface of the silicon wafer. 92

Figure 5.8 : Photolithographic mask design used for patterning the metal plate on the top surface of the glass wafer.. 93

Figure 5.9 : The cross-sectional (a) and the top view (b) of an oxidized wafer. 94

Figure 5.10 : The cross-sectional (a) and the top view (b) of a single crystal substrate having the patterned silicon dioxide on one side of the wafer.. 95

Figure 5.11 : The cross-sectional (a) and the top view (b) of the etched pit in the substrate. 96

Figure 5.12 : The optical picture of part of a two anisotropically etched silicon pits with a 100 mm gap between them. 97

Figure 5.13 : The cross-sectional (a) and the top view (b) of the oxidized pit in the substrate. 98

Figure 5.14 : The cross-sectional (a) and the top view (b) of the case after the top part of the silicon substrate etched to release the oxide mold. 100

Figure 5.15 : The cross-sectional view of the electroplated gold into the silicon dioxide mold. 102

Figure 5.16 : The cross-sectional (a) and top (b) view of the released tip.. 103

Figure 5.17 : SEM picture of a tip in micromachined by electroplating gold into a silicon mold as fabricated in Figure 5.11. This is achieved without oxide formation in the fabricated pit [89] 104

Figure 5.18 : Optical picture of an array of pits.. 105

Figure 5.19 : The cross-section of the silicon wafer after it was etched from both sides.. 106

Figure 5.20 : SEM picture of the oxide mold visible from the top of the wafer. 107

Figure 5.21 : Another SEM picture of the oxide mold visible from the top. 108

Figure 5.22 : Optical picture of the cross-section of the oxide mold with respect to counter electrode.. 109

Figure 5.23 : SEM picture of the oxide mold visible from the top of the wafer. 110

Figure 5.24 : The cross-sectional view (a) and the top view (b) of a single-layered substrate having dopant on the top surface for the counter electrode. 111

Figure 5.25 : The cross-sectional (a) and the top view (b) of a single-layered substrate having a metal electroplated into the oxide mold. 112

Figure 5.26 : The cross-sectional (a) and the top view (b) of a single-layered substrate having the highly doped counter electrode. 112

Figure 5.27 : The cross-sectional (a) and the top view (b) of a single-layered substrate having silicon dioxide layer removed from both sides of the wafer. 113

Figure 5.28 : The cross-sectional (a) and the top view (b) of a single-layered substrate having the silicon dioxide grown on both sides of the wafer. 114

Figure 5.29 : Oxide thickness versus oxidation time for silicon oxidation in water vapor (0.87 atm.). 115

Figure 5.30 : Oxide thickness versus oxidation time during initial stages of silicon thermal oxidation 116

Figure 5.31 : The oxide thickness at beginning. 117

Figure 5.32 : The oxide thickness after 1 minute.. 117

Figure 5.33 : The oxide thickness after 1.3 minutes. 118

Figure 5.34 : The oxide thickness after 4.5 minutes. 118

Figure 5.35 : The cross-sectional (a) and the top view (b) of the electroplated metal into the silicon dioxide mold.. 119

Figure 5.36 : The cross-sectional (a) and the top view (b) of the removed oxide from the top part of the wafer.. 119

Figure 5.37 : The cross-sectional view of the final micromachined field ionization detector.. 121

Figure 5.38 : Picture of the input and exhaust manifolds attached to the metallic lid.. 123

Figure 5.39 : Picture of the electrical connector. 124

Figure 5.40 : The view from one side of the aluminum box. 125

Figure 6.1 : The schematic representation of the basic gas generation and delivery system. 129

Figure 6.2 : The picture of the basic gas generation and delivery system. 129

Figure 6.3 : Schematic diagram of a permeation tube. 130

Figure 6.4 : The schematic diagram of the permeation tube in a U-tube holder. 131

Figure 6.6 : Detector performance for acetic acid vapor at a concentration of 41 ppm .139

Figure 6.5 : Detector performance for acetic acid vapor at a concentration of 57 ppm. 139

Figure 6.7 : Detector performance for acetic acid vapor at concentration of 29 ppm. . 140

Figure 6.8 : Detector performance for acetic acid vapor at a concentration of 20 ppm. 140

Figure 6.9 : Detector performance for acetic acid vapor at concentration of 14 ppm. . 141

Figure 6.10 : Dependence of the field ionization detector on acetic acid vapor concentration with 5 volts applied to electrodes. 141

Figure 6.11 : Detector performance for the acetic acid vapor concentration of 57 ppm at 40V. 144

Figure 6.12 : Detector performance for the acetic acid vapor concentration of 57 ppm at 30V. 144

Figure 6.12 : Detector performance for the acetic acid vapor concentration of 57 ppm at 20V. 145

Figure 6.14 : Dependence of the field ionization detector for acetic acid vapor with applied voltage as the variable. 145

Figure B.1 : A gaussian peak. 161

Figure B.2 : Erf function response of the detector. 162

Chapter 1

Introduction

The release of various chemical pollutants from industries, automobiles and homes into the atmosphere has been causing global environmental issues such as acid rain, the greenhouse effect and ozone depletion. They are caused by chemicals (see Table 1.1) that mostly originate from combustion-related processes. Hence, intense efforts are being exerted to research and develop new technologies and/or new chemical processes that eliminate or reduce air pollutants.

Environmental Problem	Related Gases
Acid rain	NO_x, SO_x, HCL
Greenhouse effect	CO_2, CH_4, fluorocarbon, N_2O, O_3
Ozone layer destruction	fluorocarbon, halocarbon

Table 1.1: Global environmental problems and related gases [1].

At the same time, the development of new methods to measure air pollutants is equally important for solving environmental problems [1] especially when it is understood that these pollutants can pose danger to human health as well as our environment. This simple acknowledgment has inspired researchers to develop new sensitive and selective monitoring techniques. So far, the measurements of air pollutants have been primarily carried out by the use of conventional analytical instruments in chemical laboratories. This is simply because they are usually too bulky and fragile to be operated on site. Therefore, in order to be able to carry out the measurements at the site, there is a general need for

miniaturization of the conventional analytical instrument and its supporting instrumentation such as its detector. There have been number of products that demonstrates the feasibility of manufacturing portable analytical tools. On the one hand, they tend to be too costly for small analytical laboratories to purchase and on the other, they are still considered to be heavy in weight (~10 kg). Recognition of the potential importance of miniaturization with specific low-cost approaches has been gradually growing. This fact has been reflected in current research and development efforts to improve different aspects of the fabrication processes, especially for novel detectors. Table 1.2 illustrates the comparisons between the conventional analytical instruments and the miniaturized ones [2].

	Analytical Instrument	Miniaturized Tools
Data accuracy	excellent	fair
Data acquisition	long time	real time
Size	large	compact
Cost	very high	low
Application	stationary site	stationary and mobile site

Table 1.2: Comparison between analytical instruments and micromachined detectors.

In order to be able to design and manufacture a chemical analytical instrument, to perform the detection of a wide range of chemicals, one has to probe nature to obtain ideas. A particularly well-understood biological system which is the basis of detection of chemical substances in the atmosphere for animals, is the odour analyses done by olfactory cells. Their performance characterizes the ultimate limits in the miniaturization of intelligent bimolecular structures. One such example is shown to illustrate the

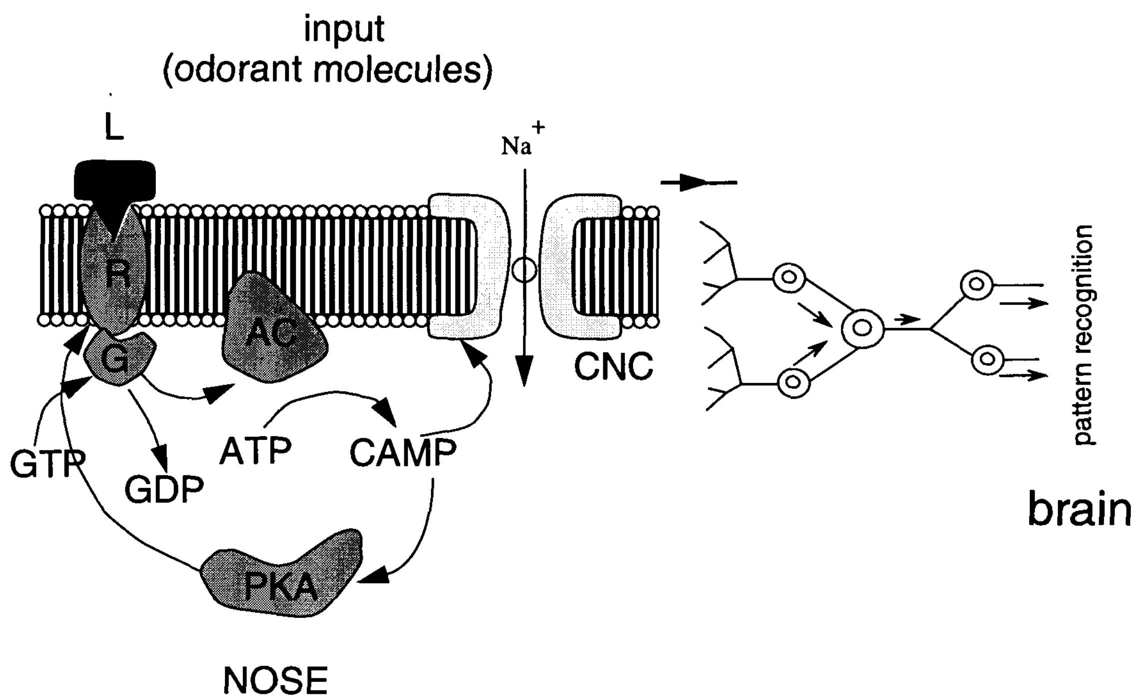

Figure 1.1 Odour recognition in a biological system with typical steps in the signal transduction [3].

functional similarities and technological differences of device components, which may be based upon either artificial (man-made) or natural (biological) structures [3]. Figure 1.1 shows a schematic diagram of an odour analysis system, with the components in an animal's nose. In contrast, Figure 1.2 shows a schematic chemical or odour analysis with the components in an electronic nose. Both 'noses' consist of completely different materials; nevertheless, similar functions formally characterize the components of both systems. Odorant molecules produce ionic or electronic signals through the action of receptors in a membrane (or of the sensor/transducer unit). The signals determine the components of a feature vector and are subsequently evaluated by means of pattern recognition either in the brain or on the computer. Hence, all chemical analytical instruments consist of these components, but different transduction principles may have to

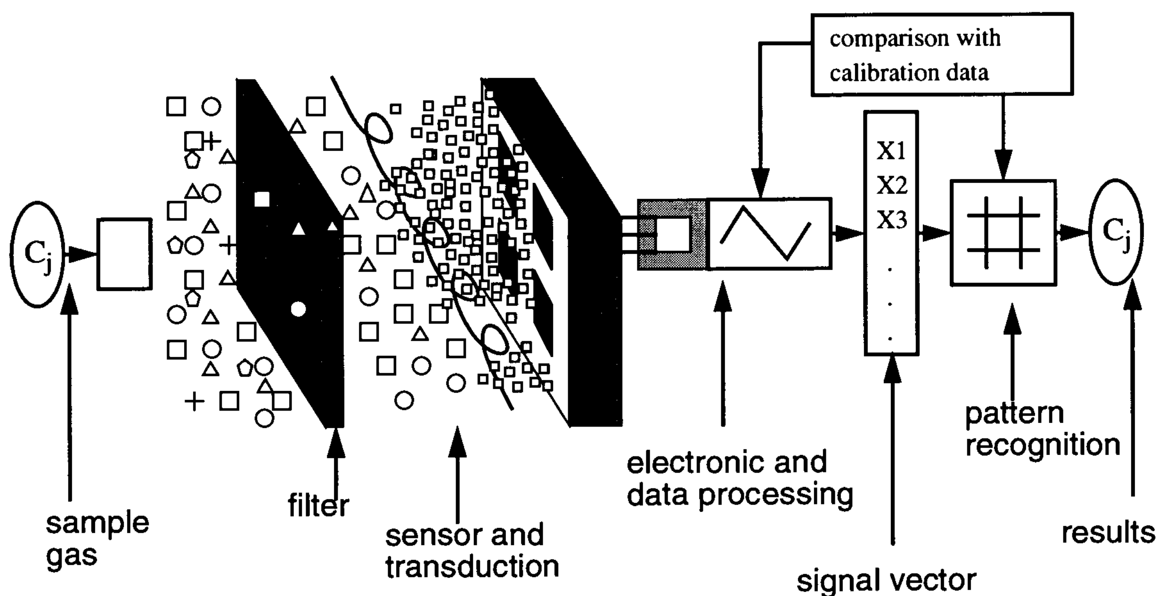

Figure 1.2 Odour recognition in electronic system with typical steps in the signal transduction [3].

be used to detect any chemical components in a given sample.

It can be seen from studying this comparison, that a useful chemical analytical instrument generally requires significant miniaturization of the different components in Figure 1.2. This frequently involves simplification and some degradation of the sensor performance. However, the goal is to allow the response to be in an acceptable error range, in order to be able to rely on the results. Therefore, an overview of some of the popular chemical transducers in current use will be given next.

1•1 Chemical Transducers

Chemical detectors as defined by the *National Research Council Committee on New Sensor Technologies: Materials and Applications* in the US are "devices or instruments that determine the detectable presence, concentration, or quantity of specific chemical substances (analytes)" [4]. However, such detectors have yet to be realized,

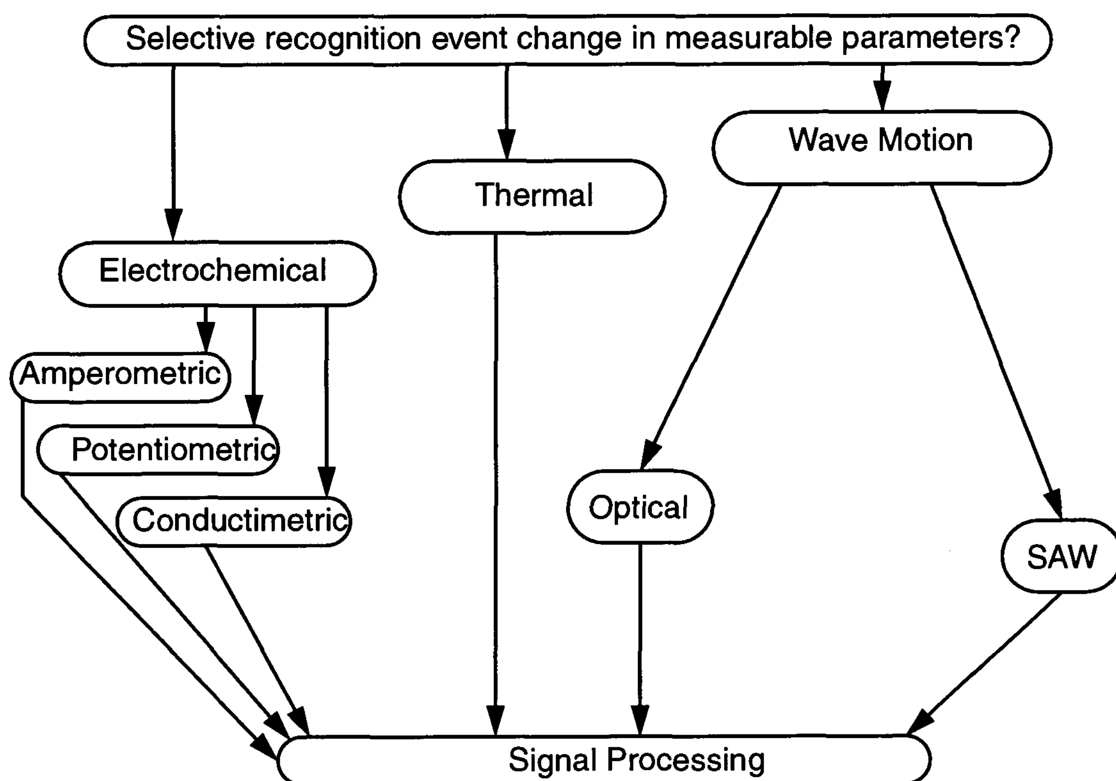

Figure 1.3 Classification of chemical detectors [4].

simply because their most severe technological limitation is the inability to obtain a selective response to a target analyte, given the millions of known molecular species, the variations in environmental conditions (presence of water, temperature, etc.), and the variations in the analyte amount or concentration by factors of 10^{23} or greater. Hence, there has been much research effort to accomplish this deficiency but the progress is slow and without spectacular success. Generally, chemical transducers are divided into two main branches and the research effort is directed along these two:

- direct-reading, selective detectors (e.g., electrochemical detectors, optical fibers);
- detectors that use a preliminary chromatographic sample separation step followed by a sensitive, but not necessarily, selective detector.

A direct-reading detector functions by detecting and rapidly responding to the presence or concentration of an analyte at the interface between the detector material and a sample analyte. This type of detector is made selective toward the desired analyte and unresponsive to others. There is a large investment involved in achieving the high selectivity for a large number of different analytes by direct-reading gas detectors. They achieve molecular selectivity through interaction at the detector-sample interface. Direct-reading gas detectors are generally classified into three groups: electrochemical, thermal and electromagnetic detectors. The classification breakdown is shown in Figure 1.3 [4].

1•1•1 Electrochemical Detectors

Electrochemical detectors work by measuring the electrical signals associated with chemical components in a chemical sample. The detector for this type usually consists of two or more electrodes that function as transducers between the chemical system and the electrical system in which the voltage or current can be measured and/or controlled. For the detector application, one of the electrodes is an indicator electrode designed to interact with species being monitored; the other electrodes' potential should remain constant during measurements. The magnitude of the voltage or current signal from the measurement is related to the activity or concentration of that species in the sample. Electrochemical detectors are generally divided into three main types: amperometric, potentiometric and conductimetric.

1•1•1•1 Amperometric Detector

In this type of electrochemical detector the response is obtained from the current-concentration relationship. The detector, like most electrochemical detectors, consists of two electrodes (cathode and anode). The principle of detection is based on the

measurement of current resulting from the oxidation or reduction of analyte molecules at the surface of an electrode in a flow-through cell. During an oxidation reaction, electrons are transferred from the analyte to the electrode whereas during reduction, the reverse process occurs; electrons leave the electrode and enter the analyte [5]. One example of where these devices is used is the Fuel Cell Sensor.

Fuel Cell Sensor

These sensors are used in breath analyzing by law enforcement officials. In its simplest form, the alcohol fuel cell consists of a porous, chemically inert layer coated on both sides with finely divided platinum (called platinum black) [5]. The manufacturer impregnates the porous layer with an acidic electrolyte solution, and applies platinum wire electrical connections to the platinum black surfaces. The entire assembly is mounted in a plastic case, which also includes a gas inlet that allows a breath sample to be introduced. Various manufacturers employ numerous proprietary distinctions in their construction. The basic configuration, however, follows the description above and is illustrated in Figure 1.4.

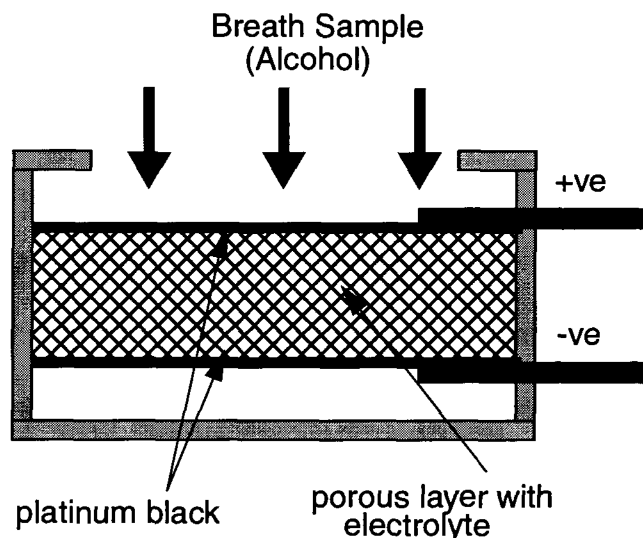

Figure 1.4 Schematic diagram of fuel cell detector [5].

The exact chemistry of the reaction that takes place in an alcohol fuel cell is open to some conjecture. Researchers assume that in the presence of often platinum catalyst, the reaction converts alcohol to acetic acid. The conversion produces two free electrons per molecule of alcohol. The reaction takes place on the upper surface of the fuel cell. H^+ ions are freed in the process, and migrate to the lower surface of the cell, where they combine with atmospheric oxygen to form water, consuming one electron per H^+ ion in the process. Therefore, the upper surface has an excess of electrons and the lower surface has a corresponding deficiency of electrons. If you connect the two surfaces electrically, a current flows through this external circuit to neutralize the charge. This current is a direct indication of the amount of alcohol consumed by the fuel cell. Using the appropriate signal processing, you can directly display breath alcohol concentrations.

1•1•1•2 Conductimetric Detector

Conductimetric detection is based on the measurement of the electrical conductivity analytes, as they move in the electric field between electrodes in a flow-through cell. No oxidation or reduction reactions take place, since there are no electron transfer reactions [5]. The measurement is based on the change in conductivity of the sensing material.

Metal Oxide Semiconductor Gas Detectors

The discovery of change in the conductance of semiconductor material when it is subjected to gases goes back to the early days of the invention of transistors in 1953 by Brattain and Bardeen [6]. Nowadays, most semiconductor gas sensors are based on metal oxide (usually Tin oxide). When tin oxide is heated to 300°-400°C by a heating coil, under certain conditions, such as in an environment containing oxygen, it behaves like an n-type

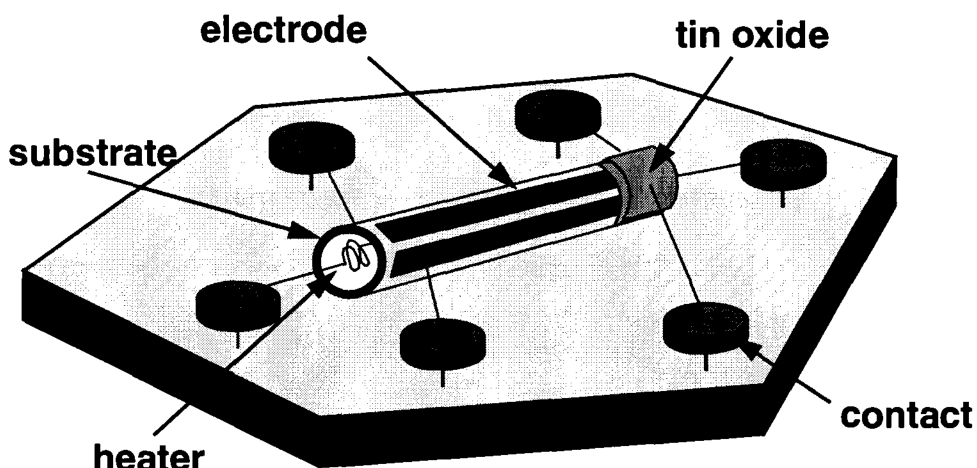

Figure 1.5 Schematic representation of a metal oxide semiconductor gas detector [7].

semiconductor. Metal-oxide semiconductor materials are extremely sensitive to trace concentrations of reactive gases in air [7]. Once in air, oxygen is absorbed onto the surface of semiconductor material. In the presence of other gases, the oxygen molecules are replaced with other gas molecules on the surface and the semiconductivity of the metal oxide changes. This effect has been observed with a number of binary metal oxides such as SnO_2, In_2O_3, ZnO, MoO_3, Ga_2O_3, Nb_2O_5 (a more complete list of all oxides can be

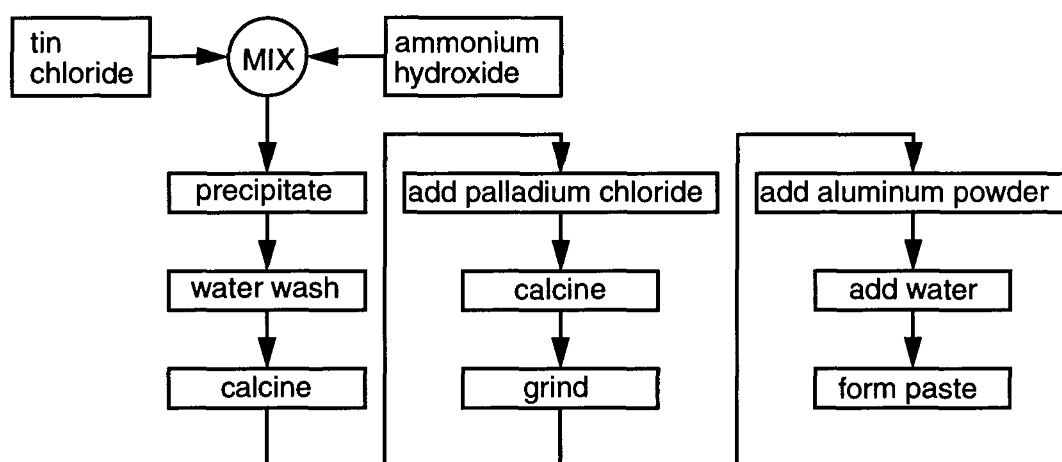

Figure 1.6 Typical preparation steps for SnO_2 paste, used as a thick film [7].

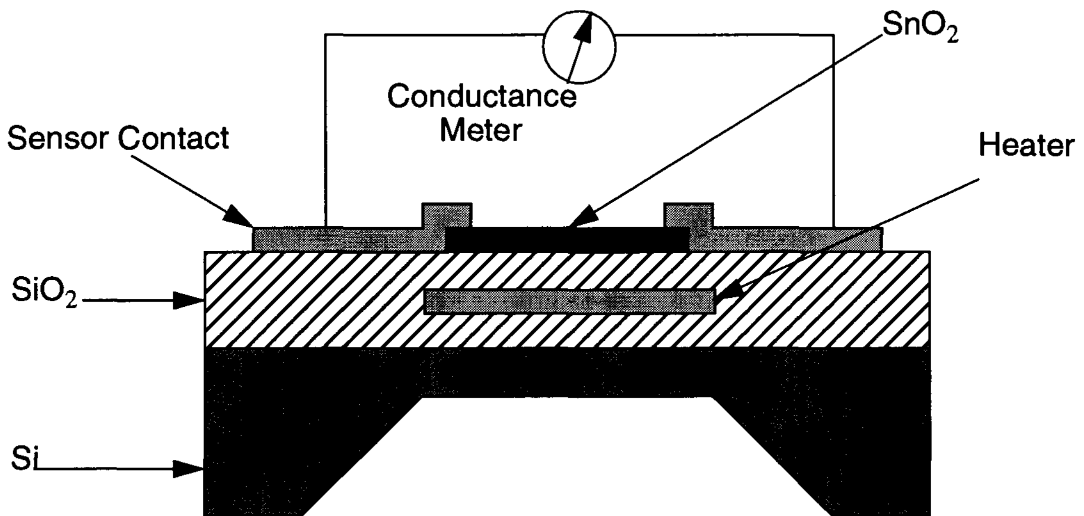

Figure 1.7 A micromachined version of metal-oxide-semiconductor gas detector [9].

found in reference [8]. The output signal is normally a logarithmic function of the gas concentration. The present sensors are not very specific and detectors using them are only really suitable for leak detector. One form of these sensors is manufactured and sold by Figaro Engineering Inc. (in Japan), shown in Figure 1.5. The function of the heater element in the centre of the tube is to bring the metal-oxide coating to a desired operating temperature. The paste of semiconductor powder is applied onto the outside of the tube. The paste is often prepared in a series of steps as illustrated in Figure 1.6 [7]. This illustrates the complexity in preparing this type of sensor. With such a series of preparation steps, the exact reproducibility of sensors' characteristics cannot be expected [7]. Nevertheless, these are some advantages of these sensors: they can work for many years and don't wear out; in stable conditions, they can pick up extremely low levels (possibly sub-ppm) of gases which can't normally be detected without sophisticated equipment; they also tend to react to anything. This is sometimes a benefit, such as when they are used as leak detectors. These are some disadvantages in addition to their

reproducibility problem: they take a few hours to settle to within 10% of their long-term zero resistance after switch-on; and they take a few days to really stabilize. This makes accurate low-level measurements essentially impossible except with fixed systems, which can be calibrated after being left on for a few days. What is more, after being exposed to high levels of gas, they can take up to 15 minutes to resettle to zero.

The possibility of measuring the change in conductivity a of metal-oxide, induced by absorbed gases with a micromachined version of these detectors is attractive and was investigated by Bott *el at.* [10]. Figure 1.7 shows the schematic cross section of one possible arrangement of this type of detector. The sensor contact is designed in an interdigited manner to make it more sensitive to change in conductance of the sensor material, SnO_2, and, at the same time, decreasing the size of the device. The use of micromachined techniques also allows easier preparation, more customized for detection of specific gases than the conventional approach. However, reproducibility still remains a big issue and depends on how good the sensor contact is sintered to the sensor material together and how uniform the resistivity of the sensor material is.

1•1•1•3 Potentiometric Detector

Potentiometric detection is based on the measurement of the potential that develops at an electrode or across a membrane, such as in an ion-specific or a pH electrode (e.g., Ion Selective FET). Amperometric and conductimetric detectors are more commonly used than potentiometric ones. In fact, all commercially available electrochemical detectors are of these first two types partly due to their higher sensitivity and speed [5]. ChemFETs are examples of the potentiometric detector group which is used for detection of gases.

ChemFETs

Generally, a FET consists of a thin-conductance channel on the surface of the silicon, which is controlled by the applied voltage on the gate metal. The gate is separated from the channel by a thin layer of silicon dioxide (see Figure 1.8) [11]-[16]. When a FET with a palladium gate is exposed to gases, the gate metal absorbs gas molecules from the ambient. This has the effect of changing the work function of the palladium which in turn appears as a shift in the threshold voltage of the FET. The selectivity can be induced in these sensors by the choice of an appropriate metal for the gate electrode [8].

The development of FET-based chemical detectors which, at one point, seemed very promising, is now plagued by a tremendous number of technological and fundamental problems. These problems are reflected in their rather poor reproducibility of performance and more importantly drift and degradation they tend to exhibit with time, which frequently even precludes the use of disposable devices. In general, FET-based chemical detectors are not presently well suited for long-term, in-line chemical analyses, and their development is mainly geared towards single-use biomedical-type applications [11]-[16].

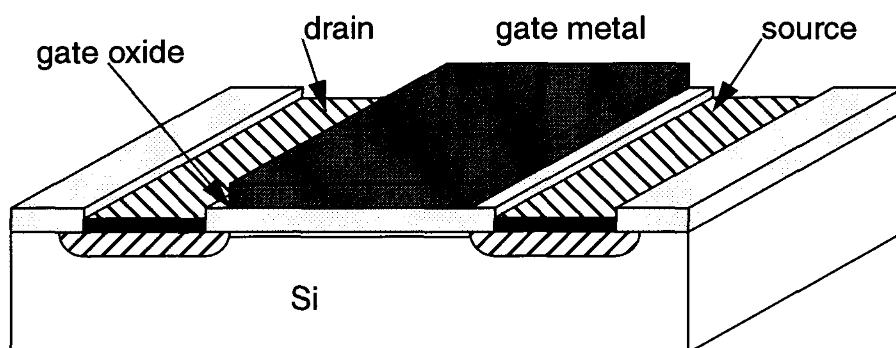

Figure 1.8 A typical ChemFET [11]-[16].

1•1•2 Thermal Detectors

The actual structure of the detector used is shown in cross-section in Figure 1.9. A {100} silicon wafer is used as the starting material. About 1000Å of silicon dioxide is thermally grown on the wafer followed by the sputter deposition of 1.5 μm of Pyrex glass on the top surface. A large hole is etched from the backside of the wafer to remove the thermally conductive silicon from beneath the detector sensing region. Finally, 1000Å of nickel is evaporated on the surface, defined photolithographically, and etched to produce the thin film nickel sensor. The thermal detector functions by being heated from an external constant current source. The temperature reached by the detector is a function of the thermal conductivity of the gas stream. This temperature is monitored by measuring the voltage across the detector, since the nickel has fairly high positive thermal coefficient of resistance (TCR). The high thermally conductive helium carrier gas causes the overall electrical resistance of the nickel resistor to drop, thus lowering the potential across the nickel resistor [2]. Any other gas that has a smaller thermal conductivity than helium results in an increase in the measured potential difference.

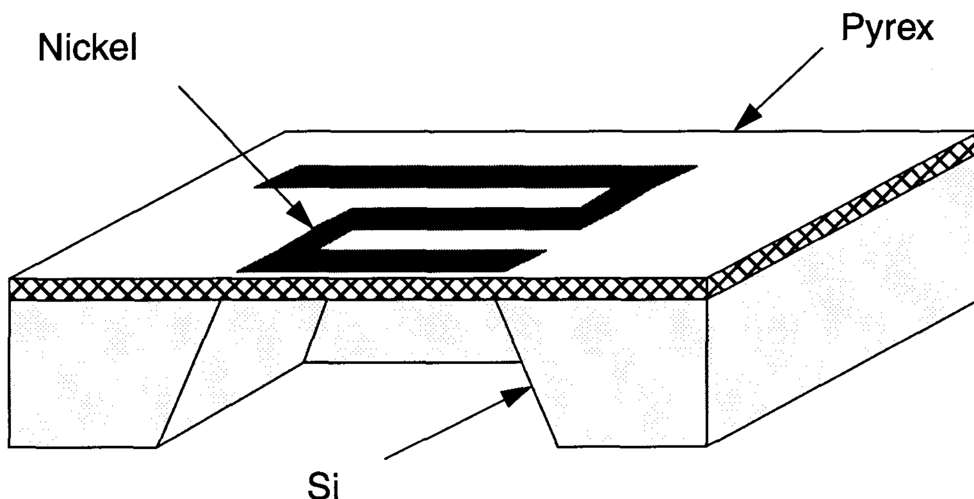

Figure 1.9 A micromachined thermal conductivity gas detector [18].

These detectors suffer from a major problem. The power consumption of a standard device is rather high for portable instruments (~1W). The micromachined version has reduced this high-power consumption to the milliwatt range; however, this is still considered to be high for a portable system [18].

1•1•3 Sensors Based on Wave Motion

1•1•3•1 Optical Detectors

There are also a wide variety of sensitive, optical detectors based upon the absorption or transmission of light (e.g., [19]). However, due to the scope of this investigation, these detectors were not considered because of their requirements for specialized instrumentation.

1•1•3•2 Surface Acoustic Wave Devices

The principle of operation of a surface acoustic wave (SAW) device for gases is conceptually quite simple. A surface acoustic wave (normal to surface) is transmitted across the surface of a solid which is exposed to the atmosphere for analysis. If the solid is a piezoelectric crystal (PZT), then the transmitted wave can be induced electrically. The transmission of the SAW is sensitive to the mass of material absorbed on the surface and may be dampened by the environment. The gaseous analyte can also interact with the surface, of which the change in frequency, amplitude and phase of the transmitted wave can be measured. The standard design for a quartz SAW is shown in Figure 1.10 [18]. For gas sensing, the is often coated in a polymer, or some such material, showing selectivity towards the analyte under investigation. When a mass is created as a result of gas being absorbed on the surface, there is a shift in the SAW device resonant frequency. The phenomenon allows the SAW to be used as a gas monitor, as the frequency shift is

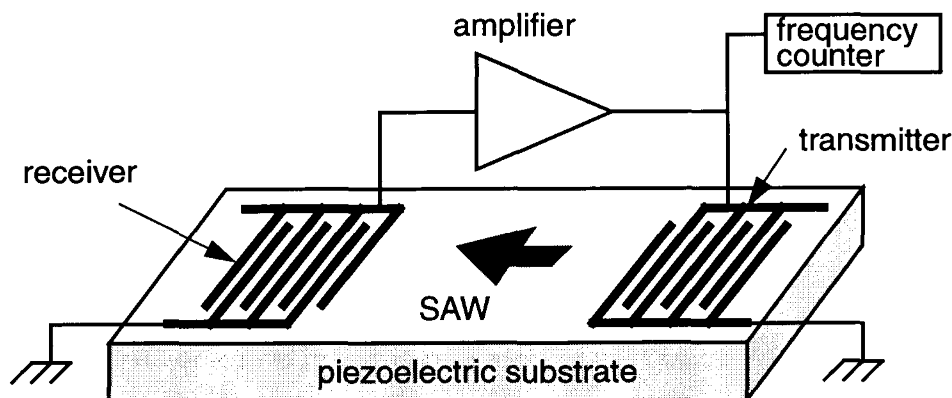

Figure 1.10 Simplified diagram of a SAW [18].

proportional to the amount of mass added. Considerable work has been done on the application of these devices to measurements of inorganic gases (e.g., NO_2, H_2, H_2S, SO_2), organic gases and vapor (e.g., CH_4, C_6H_6, C_2H_5OH) [18]. The main problems with SAW devices are their poor long-term stability, high dependence on temperature and high sensitivity to humidity.

Piezoelectric-based sensors (e.g., quartz microbalances) have a high sensitivity when compared to other types of chemical detectors and so they are quite attractive in that respect. This is because the change in mass is generally recorded by a very accurate measurement of the shift in the resonance frequency of the resonating device.

However, the drawbacks of piezoelectric devices are that the sensing material only functions at relatively low temperatures (<50°C); they also tend to be unstable for use with high-temperature oxide materials such as SnO_2. In addition, there is a limit to the use of a chemical-sensitive coating. Therefore, the careful chemical design of the coatings ultimately determines the quality of performance of these types of chemical detectors [18], [20].

1•2 Problems with Micro-Gas-Detectors

After having given a brief overview of the currently used micro-gas-detectors and their principles of operation, we can categorize their corresponding problems in four major groups: (a) selectivity issues, (b) stability, (c) reproducibility and (d) cost.

1•2•1 Selectivity

The ultimate objective in the development of gas detectors is a series of detectors, each of which responds to only one gas [7]. Unfortunately, as the preceding discussion has made clear, the nature of some of these gas detectors leads to a sensitivity to all gases, and others to only a few of them. Therefore, this objective is difficult to accomplish with current material technology simply due to the huge number of gases involved.

The alternative approach to accomplish the needed selectivity in a gas detector, as discussed in Section 1•1, is to incorporate a preliminary sample separation step, such as a chromatography column [2], [21]. Separation by the modern technique of chromatography is an extremely powerful and enabling technology for the analysis of a complex chemical mixture. When combined with a suitable detector, and an electronic data processing unit, separation-based detectors can, nonetheless potentially provide an analysis system with response times approaching those of many direct-reading detectors but with greatly enhanced effective selectivity. In this technique, a large number of different analytes in the sample are separated into pure components. A detector (which may not be necessarily selective) can then be used to detect the pure components. The time taken for pure components to come out of the separation column is used to identify the substance. The magnitude of the detector's response gives an indication of the concentration of the pure components. Miniaturized total analytical systems represent a relatively new area of

research in analytical chemistry [2], [21], [23], [24], and their development could significantly supplement the capabilities of the existing direct-reading detectors.

1•2•2 Stability

The stability of the detector is another factor which has to be taken into account in the design of gas detectors. This is the factor which indicates how resilient the detector is to certain environmental effects, such as temperature and humidity. Ideally, the detector should be completely immune to these effects, but in reality, it is difficult to achieve these goals.

1•2•3 Reproducibility

Another factor which is important from a manufacturing point of view is the reproducibility of the detectors. This factor is dependant on the sensing material and so the preparation of the sensing material plays an important role in how reproducible the gas sensor will be. Sometimes the reasons for non-reproducibility is difficult to understand and difficult to overcome for some detectors. This limitation forces the sensor to be calibrated for the gas to be detected. The use of micromachining and microfabrication techniques is preferred because they tend to improve this factor most effectively for this type of detector.

1•2•4 Cost

One of the most decisive factors which ultimately determines the success of any gas detector for commercialization is the reduced manufacturing cost. The use of micromachining and microfabrication has brought down the cost, but for certain technologies the cost still remains high. The most cost-effective gas detector used on the market is the metal-oxide-semiconductor detector. Although it has major problems with

reproducibility, it has a relatively low manufacturing cost. Nevertheless, the cost is still considered to be high for implementation in some applications in the automobile industry, such as for a better emission control of the toxic gases generated by cars. It is recommended that the cost of a gas detector should be less than one US dollar for it to be worthwhile [22]. Due to the high cost of present detectors, catalytic converters are being used a device containing a catalyst for converting the automobile exhaust gases into mostly harmless products. This is not a control device, and so in order to control the emission of exhaust gases, a cost-effective gas detector has yet to be manufactured.

1•3 Research Motivations

The scope of the problem mentioned in the previous section provides motivation for research in the gas detectors. In addition, the research motivation is also on integrating the potential gas detector with the proposed micromachined gas chromatography [2] on silicon wafer. Although, there has been a few attempts in integrating these two devices together, the research approach has been focused on using hybrid assembly. Nevertheless, there has not been any commercial product resulted from these research. This is partly due to fact that there are some issues which has not been addressed effectively, these are the integration of detector and GC system on silicon wafer and perhaps the more importantly what would be the optimum detector that is going to be used for detection of gases. Therefore, a new detector that is going to improve the manufactuability must be investigated.

In order to advance the research on micromachined gas chromatography system further, we need to target two directions. These two directions are:

• development a new gas chromatography detector for battery-powered of the micromachined gas chromatography system on Si

• the other aspect which is important, is the fabrication should rely on the use of a technology which is compatible with integrated circuits standard processes

1•4 Research Objectives

The primary objectives of the work are in two major categories:

a) Investigation the miniaturization of the gas detector;

• for operation at atmospheric pressure

• featuring standard microfabrication techniques

• featuring detection characteristics sufficient for application as an end detector in miniaturized gas chromatography

b) Research on low-cost fabrication methods;

• developing process allowing future monolithic integration of gas detector and a micromachined gas chromatography system

These categories are described in the following sections.

1•4•1 Detector Miniaturization

Among the detectors which have been literature reviewed in Section 1•1, the micromachined metal-oxide semiconductor detectors have been the most popular, due to features such as moderate cost[1], good sensitivity and simple technology. These features have made, and undoubtedly will continue to make, sensors popular for safety applications. However, these detectors' biggest drawbacks are their unselectivity,

1. Matheson Gas Products Canada manufactures this type of gas detector for a price of $400-$600 per unit detector.

unstability and irreproducibility, which has limited their successful application in the automotive industries and environmental monitoring. One approach to increase the selectivity of micro gas detectors such as these, is the idea of using a chromatography column for separating the different species before detection. For this reason, the use of a preliminary separation column is attracting more popularity [2]. The challenging part of this miniaturize system is an integrated gas detector. The *NRC Committee for New Sensor Technologies: Materials and Applications* on future sensor materials R&D opportunities has advised that ". . . one strategy to address this is the development of miniaturized high-speed separations-based sensors. These have the potential for avoiding difficulties in molecular selectivity but present major challenges in improving detector sensitivity." [4].

The operating principles of the majority of micro-gas detectors reviewed in this chapter are based on a broad range of measurement techniques and chemical reactivity, developed through research in different branches of chemistry and engineering. However, the conventional detectors used by chemists for analyzing samples do not necessarily use the same operating principle. In this respect, they are very sensitive, selective, stable and reproducible. On the other hand, their fabrication is very complex, relatively over-sized, requiring large power and sample volume. Therefore, the future detectors have to be based on one of the operating principles used by the conventional detector, but at a miniaturized level. The limit of miniaturization depends on how small the device can be shrunk, while still being able to maintain the same laws of physics applicable on the macro size. Miniaturization seems to be the new trend in industries as opposed to shrinking devices to micro-scale.

1•4•2 Low-Cost and Reproducible Fabrication Method

The technique which we selected to accomplish these objectives employs the *field ionization process*. This is one of the first, soft (non-fragmenting) ionization methods for mass spectrometry [25] and has been used for this purpose since 1954. A non-fragmenting ionizer is essential to analyze long-chain multicomponent hydrocarbon samples, as it would be impossible to select and sort out the molecular and atomic fragments resulting from the breakup of many large molecules in a mixture of several different compounds.

1•5 Research Methodology

The research methodology in this thesis is firstly to look at the state-of-the art gas chromatography detectors to see which has the potential for an integrated gas chromatography system on silicon. Two class of detector was focused on for integration on silicon wafer with the gas chromatography system was:

- biological sensors
- ionization detectors

They are two class of sensors and require two different approach. In biological sensors the major trust would be on constructing microscopic probes and equipping them with high sensitive electronic to detect biological sensors. However, in ionization detector the focus would be on developing structure with submicrometer gap between the electrodes for field ionization and develop appropriate fabrication techniques.

The gas detector discussed in this thesis works on the principle of field ionization. This is one of the principles which was applied for the detection of gases at atmospheric pressure by Madou *et al.* [26]. The electric current generated from the field ionization process is used to identify the presence and the concentration of the sample gas. However,

it never received much consideration as a gas detector due to its high manufacturing cost of sharp tips, according to Spindt *et al.* [27]. The major problem with the fabrication of a field ionization detector has been the alignment of the tip to a counter electrode [28]. One obvious way of simplifying the fabrication problem of the micromachined field ionization detector is to use only a single tip. However, the efficiency of the multipoint ionizer is better than that of the traditional activated wire field ionization system. The current produced by a single tip is insufficient to be measured accurately. Therefore, a design change that reduces manufacturing difficulties, increases the sensitivity with much reduced cost and improves efficiency of detection, is the objective of this research. There is feeling that ionization detector will cover a wider spectrum as chromatography gases and therefore I think they are more promising for research.

1•6 Thesis Overview

Chapter 1 gives the thesis introduction which includes an overview of the chemical transducers, the problem definition and objectives. Chapter 2 presents a literature review and discussion of the basic operating principles of conventional gas chromatography detectors. The complexity of some of them is examined. Chapter 3 presents the fundamental theoretical background of the field ionization process. Once this framework is established, the micromachined tool used to microfabricate a field ionization detector is discussed in Chapter 4. The design and fabrication process of the field ionization detector is addressed in Chapter 5. Chapter 6 presents the experimental setup used and its results in the testing of the field ionization detector's functionality. Chapter 7 provides conclusions and suggestions for further research.

Chapter 2

Gas Chromatography Detectors

In the previous chapter, the four major problems with micro-gas-detectors, as far as their use in chemical analysis instruments are concerned, were identified. In this chapter, the conventional detectors currently used in gas chromatography are reviewed, from the prospective of miniaturization and their integration in a micromachined gas chromatography column. The ability of the gas chromatography system to separate the various components of an unknown sample, and then quantify the characteristics of these components (such as their concentration), makes it a powerful instrument for the analytical chemist.

Gas chromatography is a particularly valuable instrument in a variety of disciplines, such as medical analysis, toxic and combustible gas monitoring, automobile combustion control, environmental pollution monitoring, the classification of fuels and solvents in the air, and the detection of pesticides. Unfortunately, the size of modern gas chromatographs are much too large to be operated in on-site analysis. Consequently, this situation, along with the fragility of the instrument itself, has motivated researchers to look for an alternative and more portable gas chromatography design [2]. One of the long-term objectives (and the thrust of this research) is to manufacture a gas chromatograph which can totally integrate a separation column with a miniaturized detector on a common substrate. Two stumbling blocks associated with the development of the micromachined gas chromatography system have been firstly, to develop a miniaturized detector which

has the qualities mentioned in Section 1•2 and, secondly to achieve a high fabrication yield for the micromachined gas chromatography column on a silicon wafer. The integration of these two components on a common substrate, with one single continuous fabrication sequence, allows the manufacturing cost to be reduced considerably by eliminating the manual assembly. To date, there have been two attempts in making a micromachined gas chromatography system. The first attempt was done by Terry *et al.* [2] who fabricated the various gas chromatography systems' with a hybrid-assembled gas detector. Their detector worked on the principle of thermal conductivity, which is not ideal for portable instruments, as it consumes a large amount of power. Reston *et al.* [24] on other hand, made a great deal of improvement on the original design and homogeneity of the stationary phase in the column. They also replaced the thermal conductivity detector with a conductimetrics. He demonstrated the functionality of his detector to two sample gases (NO_2 and NH_4), although, he didn't get very conclusive results with NH_4.

As detectors are the most important part of the gas chromatography system and there are a number of different detectors available for a particular application, this chapter is going to discuss briefly the operating principles of the most common type. This discussion is meant to emphasize the motivation behind and the justification for choosing the micromachined field ionization detector as our preferred choice for the micromachined gas chromatography system's detector. Although it is believed that other detectors can also be miniaturized, the complexity in their design, high-manufacturing cost and requirement for specialized material proved to be the decisive factors in rejecting them as the potential detector in our research efforts. A detailed review of the general field ionization detector's operating principle, its structural design, and its microfabrication process follows in the

next few chapters.

2•1 Fundamentals of Gas Chromatography

An excellent general discussion of a gas chromatography system can be found in many references; for example, [29] through [31]. Here we are only presenting the basics necessary for understanding the fundamentals of the gas chromatography system's operation.

The five major components of a conventional gas chromatography system are the following: a carrier gas, an injection port, a separation column with the stationary phase, a detector and a data processing unit to record the data (see Figure 2.1). The carrier gas, also known as the mobile phase, is a high-purity gas (e.g., hydrogen or helium) that transports the sample gas of interest through the column. It is usually selected so as to maximize its chemical inertness with respect to the sample gas and the stationary-phase column coating. The sample injector is an electromechanical device that introduces a precise and finite gas sample volume into the carrier gas stream that continuously flows through the column. The column itself is a long spiral glass tube, coated with a stationary phase material that chemically interacts with the injected gas sample to produce a propagation

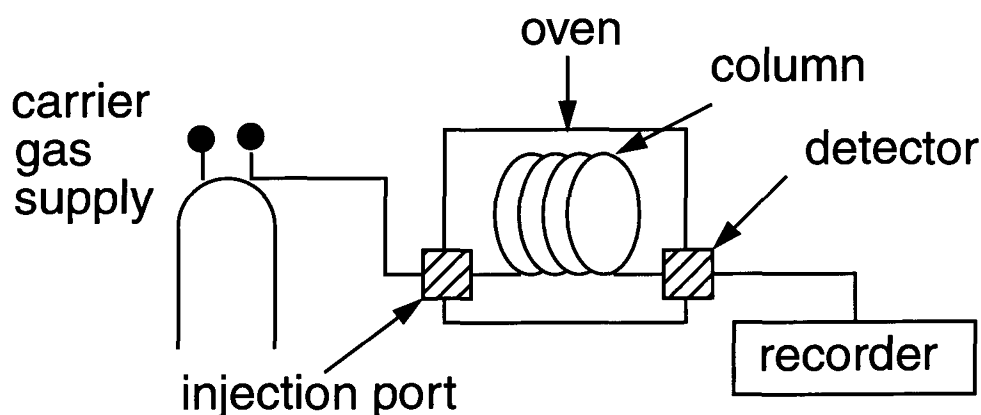

Figure 2.1 Schematic diagram of a gas chromatography system [32].

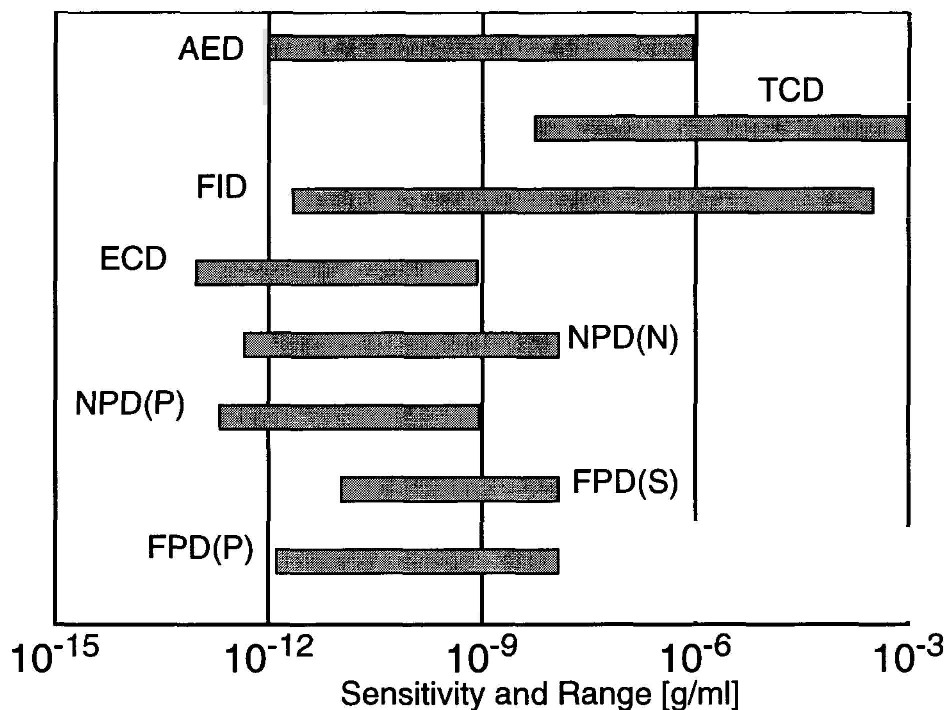

Figure 2.2 Some of the detectors' sensitivity range [32].

delay for each of its components in the sample gas. The process is based upon heat absorption and vapor pressure. This phenomenon results in the physical separation of the sample's individual constituents and the column's stationary-phase coating and causes the sample components to emerge from the column at different times. The detector which is chosen from a wide range is located at the column's output and is used with the data processing system to identify and quantify the concentration of each species.

2•2 Detectors and their Principles of Operation

Gas chromatography detectors differ from other detectors (e.g., selective detectors) in that the input to the detector is in the form of the *flow* of separated chemical components. Therefore, they must complete analysis in a few seconds or less. For this reason, most gas chromatography detectors must have good sensitivity and dynamic range. Figure 2.2 presents the sensitivity of some of the most popular detectors in gas

chromatography systems. The principles of operation of these detectors are discussed briefly in this chapter. In addition to this, the detectors are most often required to quantify known compounds. The detector provides the actual results for our interpretation of the process. A wide variety of physical and chemical properties are used for measuring purposes in gas chromatography. Choosing the right detector for miniaturization purposes requires an understanding of the transduction mechanism of each type of detector.

2•2•1 Flame Ionization Detector

One of the most common detectors used in the conventional gas chromatography system is the Flame Ionization Detector (FID). The FID consists of two electrodes with fixed but different potentials, placed over a small burning hydrogen-air diffusion flame (see Figure 2.3). A hydrogen-air diffusion flame provides the high temperature needed to strip and crack organic molecules. The organic compounds are introduced into the flame through the capillary column effluent. The electrically charged species are formed and collected with the electrodes. This results in an increase of the time-varying current between the electrodes which is usually proportional to the carbon content in the flames' organic compounds. The resulting current can be amplified if its magnitude is small.

Although the FID primarily detects compounds with hydrocarbon molecules, it can still be used as a form of a reliable detector in gas chromatography for several reasons [29]:

- Modest changes in flow, pressure, or temperature have a minimal effect on its response characteristics;
- In the normal operating mode it does not respond to common carrier gas impurities such as water or carbon dioxide;
- When properly installed, it has a stable baseline;
- It has a wide linear range, about 10^8.

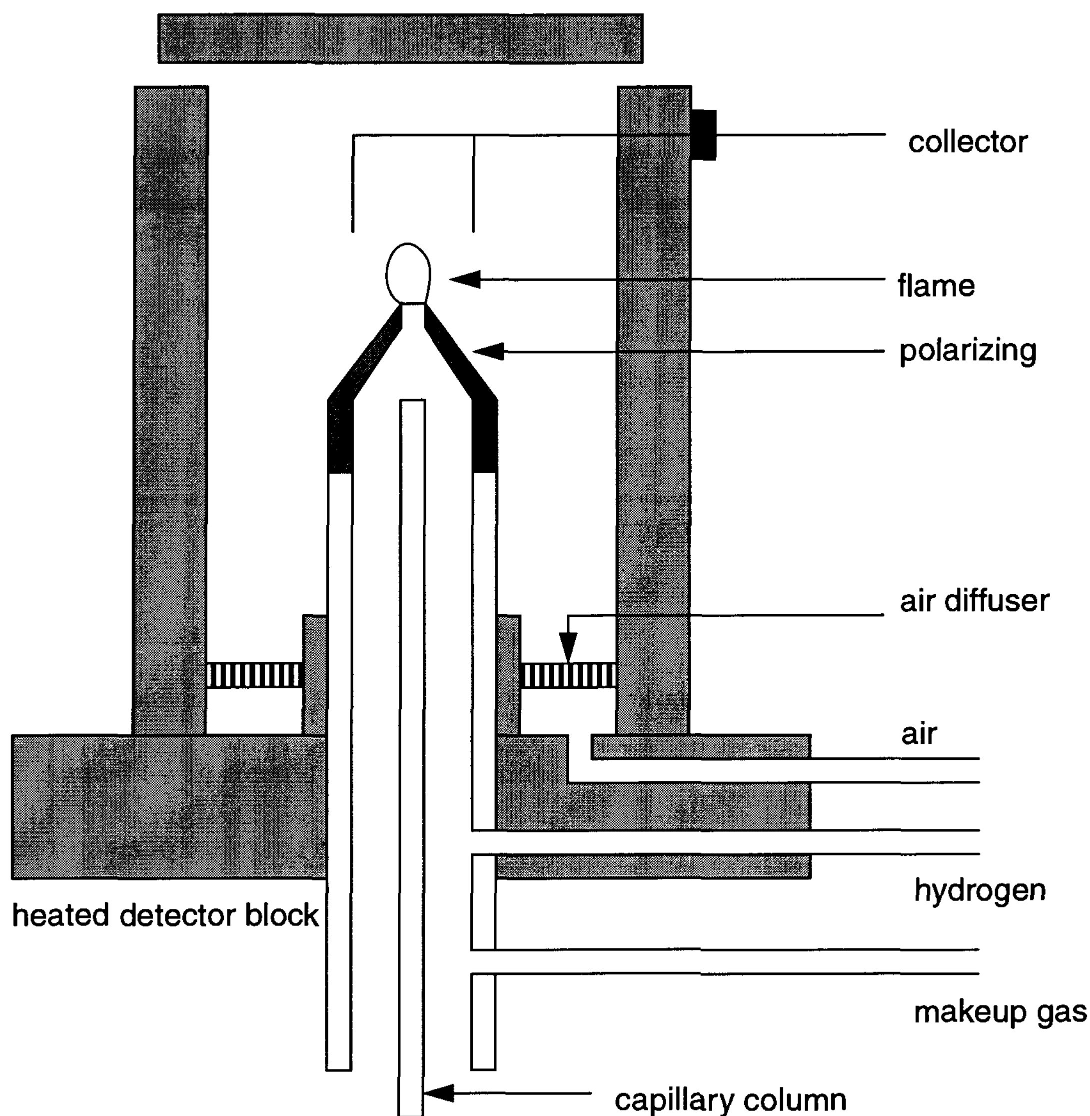

Figure 2.3 Schematic diagram of a flame ionization detector [29].

These attributes make FID a useful detector in making quantitative analyses with a gas chromatography system. Unfortunately, the FID is not highly selective to other gases. Table 2.1 lists gases that have little or no response to the FID [29]. The lack of response to these gases, coupled with the difficulty of miniaturization of the complex FID structure with micromachining techniques, implies that the FID should not be considered as the preferred candidate for the micromachined gas chromatography system. Since one of the

main objectives of micromachined gas chromatography is its use as a means of monitoring the pollution level in our atmosphere, it must be able to detect the pollutant gases such as those mentioned in Table 1.1.

He	N_2	H_2S	NO	CCl_1
Ar	O_2	CS_2	N_2O	$SiCl_4$
Kr	CO	COS	NO_2	CH_3SiCl_3
Ne	CO_2	SO_2	N_2O_3	SiF_4
Xe	H_2O	HCN	NH_3	$SiHCL_3$

Table 2.1 Gases with little or no response to the FID [29].

2•2•2 Ionization Gauge Detector

In ionization gauge detector, electrons are produced from a heated filament and are accelerated by an electric field. This is done to allow them to acquire sufficient energy to ionize gases in their path by collision. Its principle is very similar to the vacuum ionization gauge, which uses the current produced to measure small gas pressures. Littlewood [31] has modified a standard vacuum ionization gauge to act as a detector in gas chromatography. His modified design is shown in Figure 2.4 [31]. A small fraction of the effluent is passed into the ionization gauge. The gas in the ionization gauge is continuously pumped out thoroughly so that the pressure in the gauge is kept at a steady value. Helium is used as the carrier gas because of the required high-ionization energy. The ionization potential of helium is 24.5 eV so that when no vapor is passing through, the electrons do not have sufficient energy to ionize the helium and there is no current at the plate. As soon as an organic vapor enters, however, its molecules can be ionized by 18 eV on the grid electrode [31]. The detector's sensitivity can be increased by increasing the

grid potential. This potential can be increased so long as this potential is smaller than the potential required to ionize the helium.

The advantages of this type of detector are that it is not affected by variation in temperature, flow rate through the column, or external pressure [31]. Thus, it can be effectively used with the temperature operation of the column without danger of drift. The other advantage of this type of detector is its instantaneous response to a change in composition. As the size of this type of detector becomes smaller, the volume required to

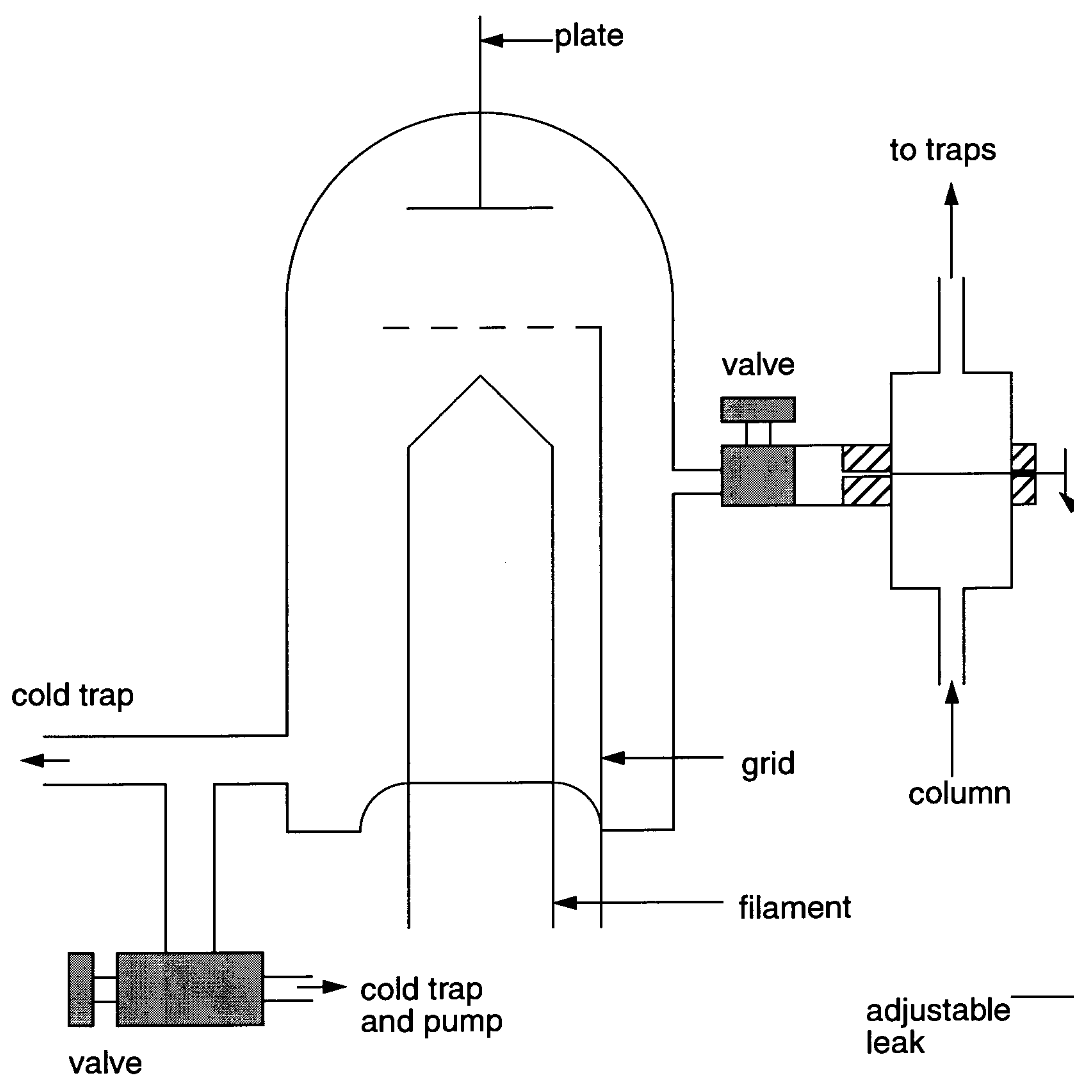

Figure 2.4 An ionization gauge [31].

fill it also becomes smaller. Thus, in spite of its large actual volume, the detector is rapid, and will work on small gas flow rates [31]. For this reason it is suitable for use with capillary columns.

These detectors will respond to all substances whose ionization potential is less than that of carrier gas; e.g., with a helium carrier gas, this includes everything [31]. Thus its use is universal. However, its biggest drawback as far as microfabrication is concerned, is its requirement to operate at a low pressure, which requires a vacuum pump [31].

The complexity behind the fabrication of a hot filament for this type of detector using micromachining techniques argues against its use in the micromachined gas chromatography system, where simplicity in fabrication is the key.

2•2•3 Thermal Conductivity Detector

The thermal conductivity detector (TCD) is one of the most commonly used detectors in gas chromatography. It operates by sensing a difference in thermal conductivity between its heated filaments. The thermal conductivity cell is extremely sensitive to the fluctuation of physical variables. Some of these can be cancelled out if two cells are used [24]. Figure 2.5(a) shows the schematic diagram of a typical TCD cell [29]. Typically, one is used to detect samples and the other to serve as a reference. A Wheatstone Bridge circuit is used to balance the resistance of the sample cell against the resistance of the reference cell (Figure 2.5(b)). Two resistors, R_1 and R_2, comprise the remainder of the bridge. When no substance is being extracted, all the resistors have the same value and there is no voltage difference to be measured. However, when a sample extracts from the column, its resistance increases and a voltage difference is measured. If a change in room temperature affects the resistance of the analytical cell, it will also affect

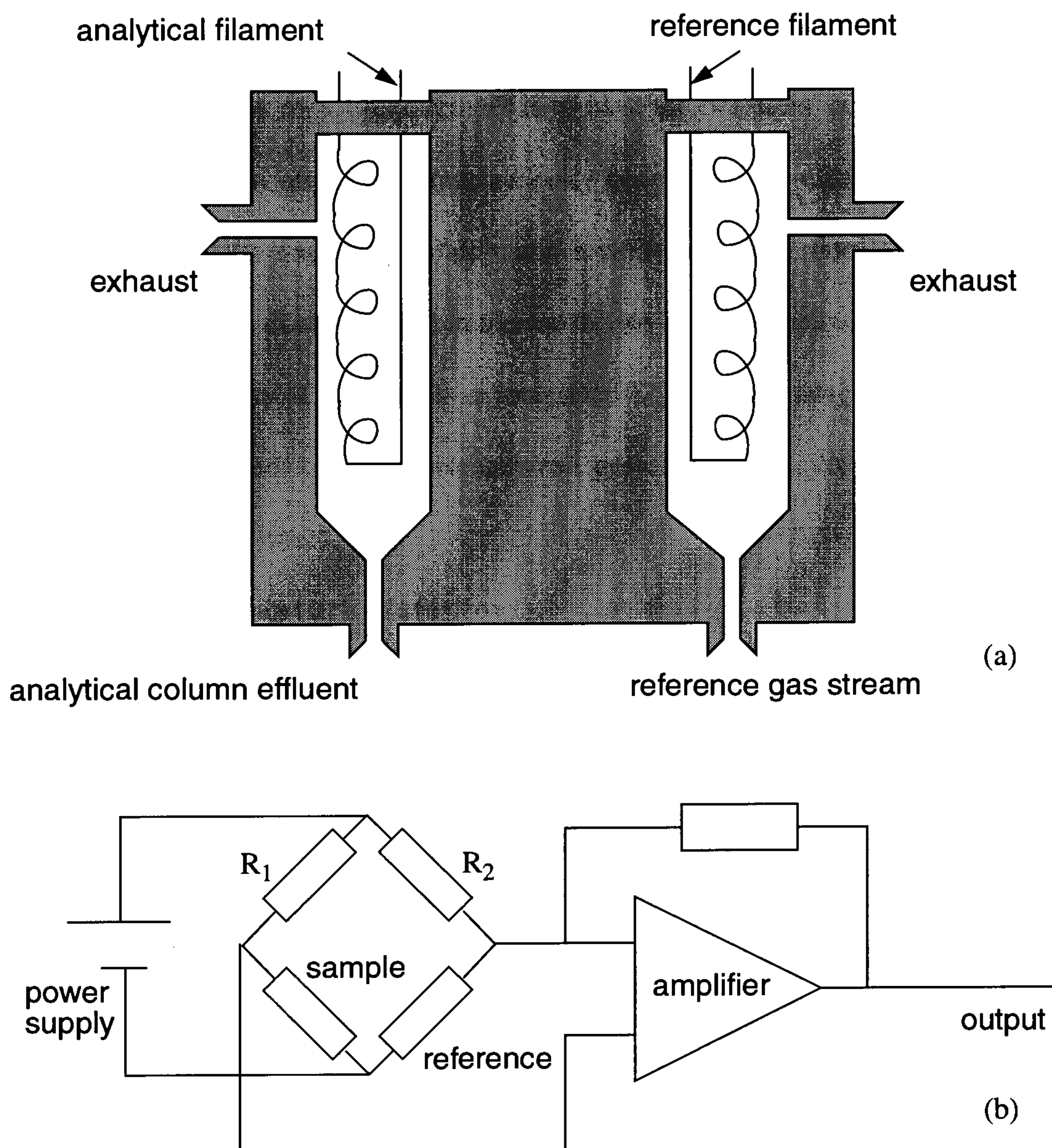

Figure 2.5 (a) Standard Thermal Conductivity Detector (TCD) and (b) a Wheatstone Bridge configuration [29].

the resistance of the reference cell by nearly the same amount. Hence, no significant change in voltage would be measured. Generally, the conventional TCD is considered a general detector since it is capable of detecting most gases [29].

The electrical requirements for a micromachined version of the TCD is slightly

more demanding to meet than for a conventional TCD used in gas chromatography, even though there have been a number of attempts regarding the fabrication of these devices on silicon wafers [2]. The major requirement is to have the detectors' filaments all matched electrically; they must also match mechanically because of the effect on the geometric factor. This is usually easy to regulate using a well-controlled process such as CMOS technology. However, this will result in the use of two different technologies which we try to avoid. This difficulty of fabricating an integrated TCD device using the CMOS foundry and the technique used for the micromachined gas chromatography column makes this device not a desirable one.

2•2•4 Electron Capture Detector

One of the most popular and powerful gas chromatography detectors in use today is the electron capture detector (ECD). It is based on gas-phase electron capture reactions

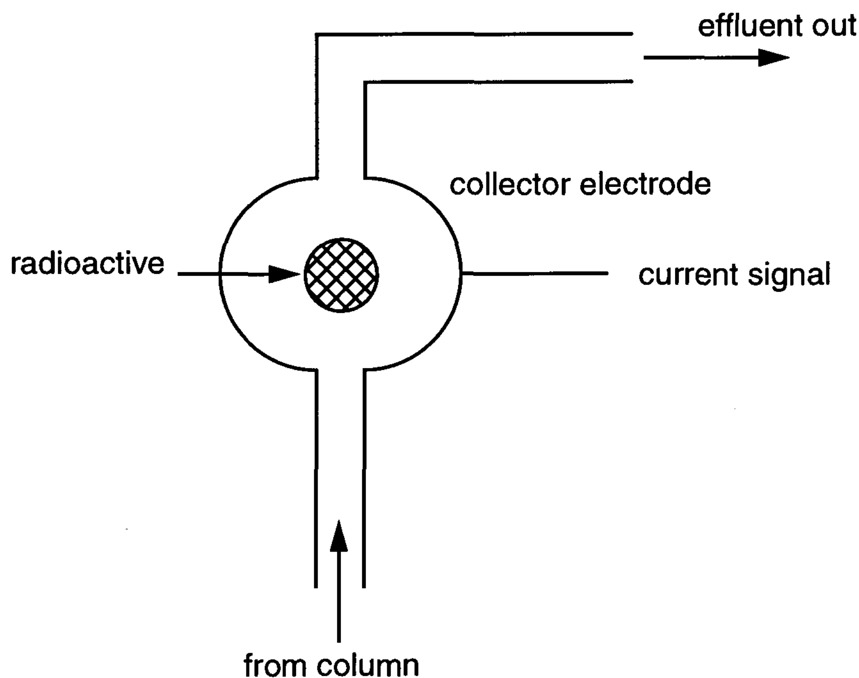

Figure 2.6 An Electron Capture Detector (ECD) [32].

and their approach to detection can provide a response to a picoliter or even femtoliter levels of specific substances (see Figure 2.6). This makes it an ideal detector for environmental and biomedical studies.

However, the ECD (see Figure 2.6) is selective towards halogenated compounds. In this type of detector, nitrogen or argon is usually used as the carrier gas. A β-radioactive source is used to ionize the effluent in the column and record the current flowing between two electrodes held at a fixed potential (say 1000V) [29]. Since the carrier gas is easily ionized by the β-radiation from the radioactive source, a steady-state current response can be obtained [29]:

$$N_2 \overset{\beta}{\Leftrightarrow} N_2^+ + e^- \qquad (2.1)$$

However, it has been theoretically proposed that electronegative species, functionally present in an organic molecule, can capture an electron to form a negatively charged species. This results in a sharp drop of current [29]:

$$EC + e^- \Rightarrow EC^- + energy \qquad (2.2)$$

where *EC* is the electronegative species. Therefore, the decrease in the current represents the quantity of halogenated compound in the chamber, and this change can be readily measured. Since ECD is mainly designed for halogen gases and requires a radioactive source, it would not be a suitable detector for this research.

2•2•5 Atomic Emission Detector (AED)

One of the newest additions to the gas chromatographer's arsenal is the atomic emission detector (AED). This detector, while quite expensive compared to other commercially available gas chromatography detectors, is an extremely powerful

alternative. For instance, instead of measuring simple gas phase (carbon-containing) ions created in a flame as with the flame ionization detector, or the change in background current because of the electronegative element capture of thermal electrons as with the electron capture detector, the AED has a much wider applicability, being based on the detection of atomic emissions [29].

The AED's strength lies in the detector's ability to simultaneously determine the atomic emissions of many of the elements in the analyte that elute from a gas chromatography capillary column. As extracts come off the capillary column, they are fed into a microwave powered plasma (or discharge) cavity, where the compounds are destroyed and their atoms are excited by the energy of the plasma. The light emitted by the excited particles is separated into individual lines via diffraction grating, and by a photodiode array. The associated computer then sorts out the individual emission lines and

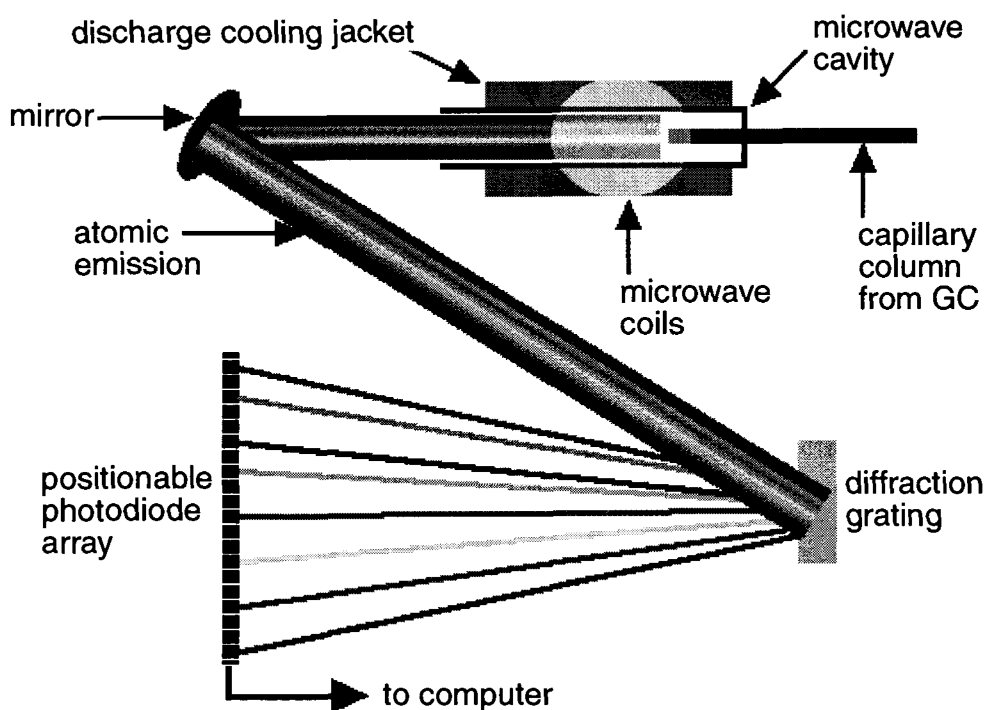

Figure 2.7 A gas chromatographic atomic emission detector [32].

can produce chromatograms made up of peaks from the sample containing only one specific element (see Figure 2.7). It is a very delicate approach, but the downside of this detector from the miniaturization point of view is the complexity of manufacturing it all on a silicon wafer [29].

2•2•6 Helium and Argon Ionization Detector

Two other detectors developed for the CSD are the Helium and Argon Detectors. The argon detector differs from the CSD one in that the carrier gas must be argon which is excited (but not ionized) to a metastable state. Since the metastable state is not ionized, the carrier gas does not contribute to the conductivity within the ionizing chamber (see Figure 2.8). The species formed is then capable of ionizing all compounds with a lower ionization potential. The products formed are then subject to an electric field and the change in current is measured. Since the ionization potential of helium (19.8 eV) is significantly higher than that of argon (11.8 eV), helium has the capacity to ionize some species that argon cannot. Additionally, the excited argon atoms increase the probability of ionization for the other gas species. This feature improves the detector's sensitivity. Both helium and argon detectors share the same disadvantage as the ECD and the CSD, the requirements of the radiation source [29].

2•2•7 Photoionization Detector

The reason to use more than one kind of detector for gas chromatography is to achieve a selective and/or highly sensitive detection of specific compounds encountered in particular chromatographic analyses. The selective determination of aromatic hydrocarbons or the organo-heteroatom species is the job of the photoionization detector (PID) (see Figure 2.8). This device uses ultraviolet light as a means of ionizing an analyte

exiting from a GC column. The ions produced in this process are collected by electrodes. The current generated is, therefore, a measure of the analyte concentration. If the energy of an incoming photon is high enough (and the molecule is quantum mechanically *encouraged* to absorb the photon), photo-excitation can occur to such an extent that an electron is completely removed from its molecular orbital, i.e., ionization [32].

$$R + h\nu \Rightarrow R^{+} + e^{-} \qquad (2.3)$$

If the amount of ionization is reproducible for a given compound, pressure, and light source, then the current collected at the PID's reaction cell electrodes is reproducibly proportional to the amount of that compound entering the cell. The reason why the compounds routinely analyzed are either aromatic hydrocarbons (contains at least one benzene ring) or heteroatom containing compounds (like organosulfur or organophosphorus species), is because these species have ionization potentials (IP) that

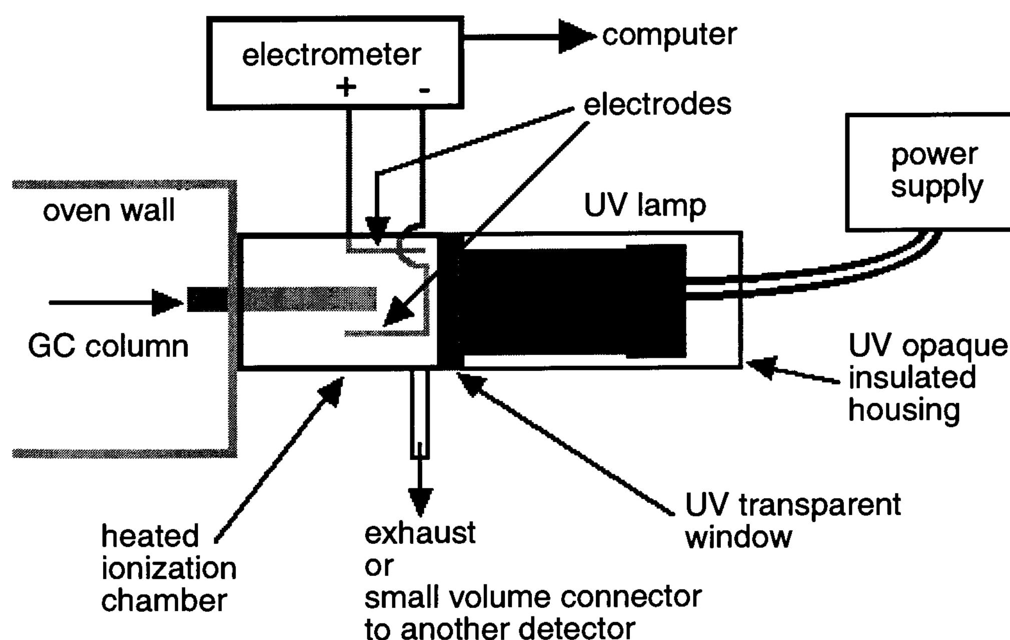

Figure 2.8 A gas chromatographic photoionization detector [32].

are within reach of commercially available UV lamps. The available lamp energies range from 8.3 to 11.7eV, i.e. λ_{max} ranging from 150nm to 106nm. Although most PIDs have a single lamp, lamps in the PID are exchanged depending on the compound selectivity required in the analysis [32].

However, the significant disadvantages of PID are the complex difficulties encountered with fabricating a transparent window for photons which can pass through it on a scale compatible with a micromachined gas chromatography system. Thus, the PID is not considered as a suitable detector for this research.

2•2•8 Flame Photometric GC Detector

The determination of sulfur- or phosphorus-containing compounds is the job of the flame photometric detector (FPD) (see Figure 2.9). This device uses the chemiluminescent reactions of these compounds in a hydrogen/air flame as a source of analytical information

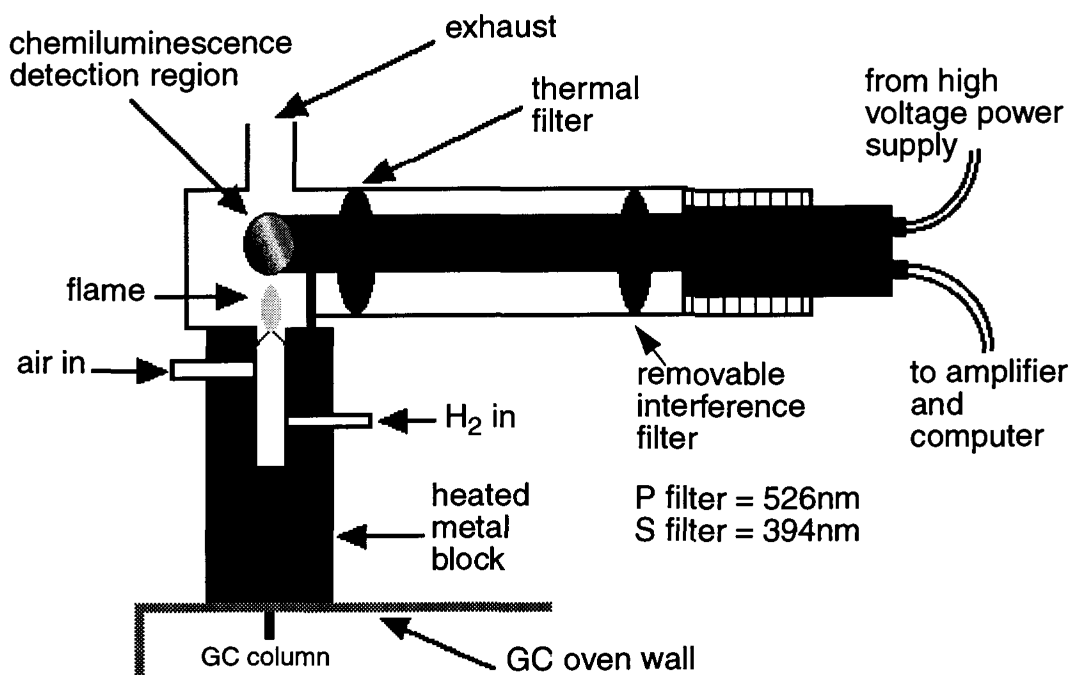

Figure 2.9 A gas chromatographic flame photometric detector [32]

that is relatively specific for substances containing these two kinds of atoms. The emitting species for sulfur compounds is excited S_2. The λ_{max} for the emission of excited S_2 is approximately 394nm. The emitter for phosphorus compounds in the flame is excited (λ_{max} = doublet 510-526nm). In order to selectively detect one or the other family of compounds as it elutes from the gas chromatography column, an interference filter is used between the flame and the photomultiplier tube (PMT) to isolate the appropriate emission band. The drawback here is that the filter must be exchanged between chromatographic runs if the other family of compounds is to be detected [32].

In addition to the instrumental requirements for 1) a combustion chamber to house the flame, 2) gas lines for hydrogen (fuel) and air (oxidant), and 3) an exhaust chimney to remove combustion products, the final component necessary for this instrument is a thermal (bandpass) filter to isolate only the visible and UV radiations emitted by the flame. Without this, the large amounts of infrared radiation emitted by the flame's combustion reaction would heat up the PMT and increase its background signal. The PMT is also physically insulated from the combustion chamber by using poorly (thermally) conducting metals to attach the PMT housing, filters, etc. [32].

The physical arrangement of these components is as follows: flame (combustion) chamber with exhaust, permanent thermal filter (two IR filters in some commercial designs), a removable phosphorus or sulfur selective filter, and finally the PMT. The manufacturing of this detector on a Si wafer is quite a complex project.

2•2•9 Hall Electrolytic Conductivity Detector (HECD)

Like the electron capture detector, the HECD is selective towards detecting halogenated compounds. Halogens in the column effluent are catalytically converted to

acids and mixed with solvent to form a heterogeneous mixture in liquid and gas phases. The liquid phase extracted from this mixture passes through a bridge-type differential conductivity detector.

The complexity of this detector argues against its potential use in the micromachined devices environment where simplicity is the key to process development. Additionally, since the HECD is selective towards only halogen atoms, this would not make a good choice for the micromachined gas chromatography detector.

In summary, among detectors described here, probably the ionization gauge is the most suitable one for micromachining technology. However, it requires vacuum to function.

2•3 Biological Detectors

This category of detectors has been investigated in recent years [35] and [36]. These detectors incorporate live biological organs for various applications. Research on chemical analysis systems based on biological detectors has been significantly advanced

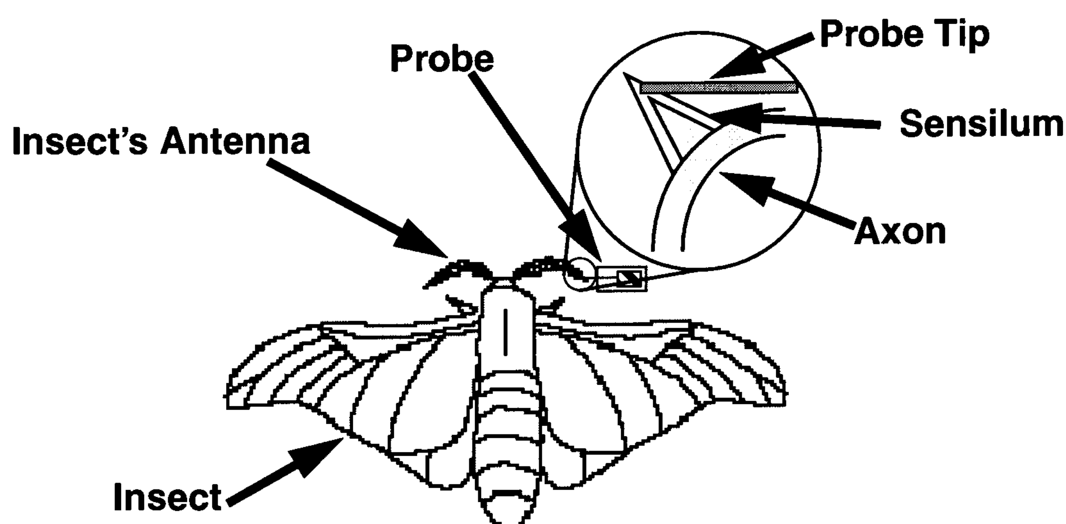

Figure 2.10 Illustration of the moth with the attached MEMS probe.

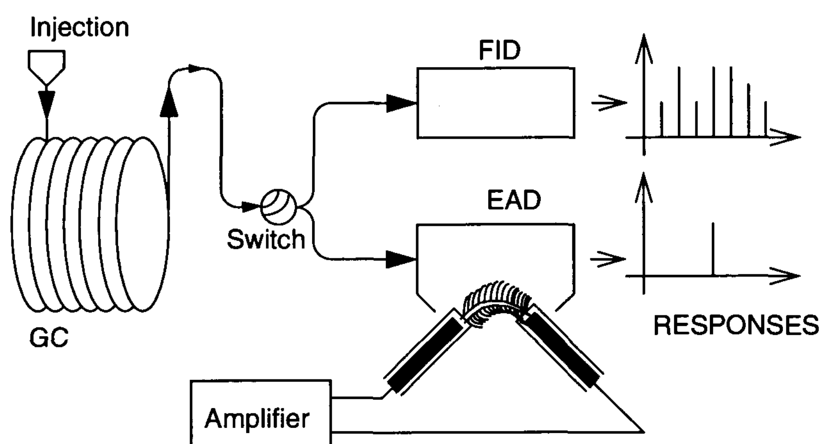

(a)

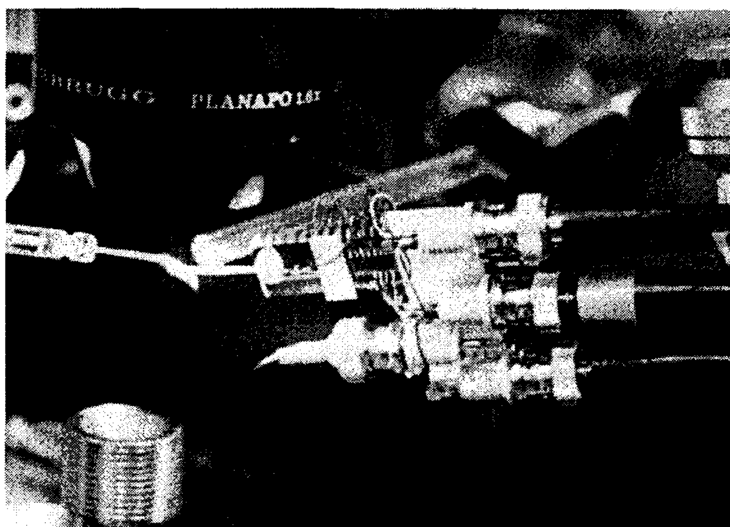

(b)

Figure 2.11 (a) Schematic representation of the experimental setup, (b) the packaged biological detector with an amplifier [37].

by new developments in microelectromechanical systems (MEMS) technology. The micromachining techniques allow significant miniaturization and integration of the entire biological system on the silicon substrate with other signal processing circuits for much improved accuracy and reliability. For instance, these detectors have opened new capabilities for conventional chemical analysis systems such as the gas chromatography system. A gas chromatography analysis may be further advanced with much improved selectivity and sensitivity by coupling them to, for instance, an insect's antenna. This

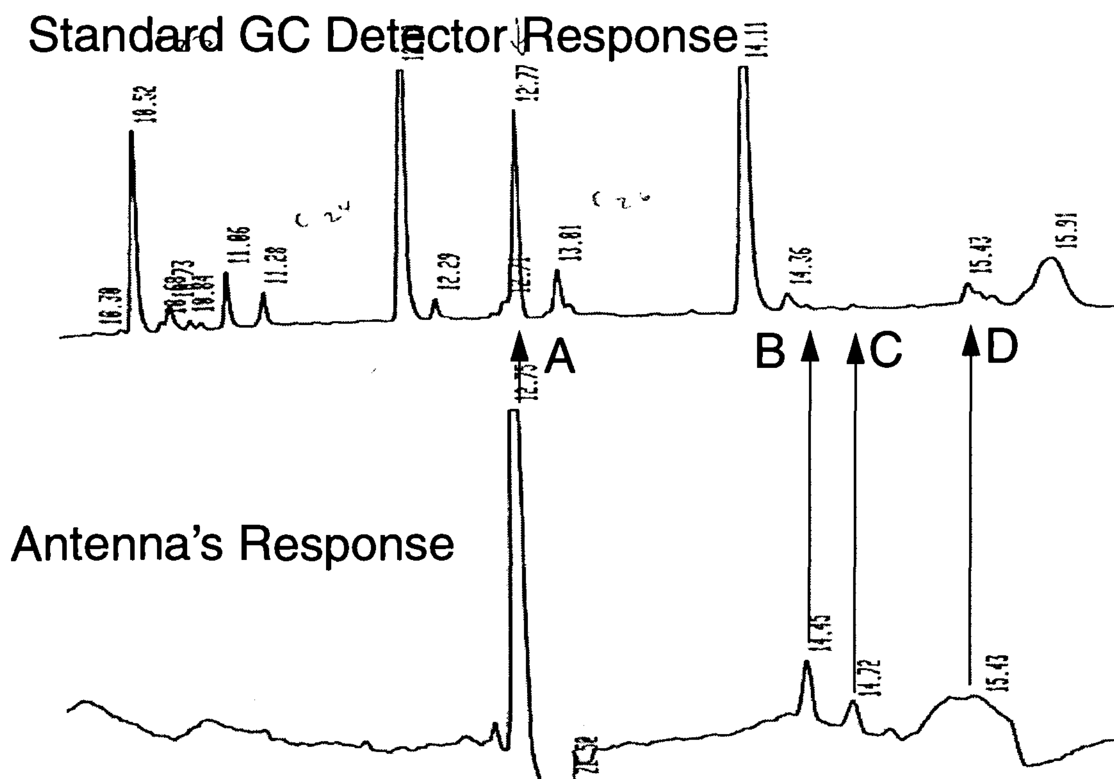

Figure 2.12 Detector response to one female Processionary moth [37].

technique is called an electroantennagraphic detector (EAD) and it usually uses a wide variety of an insect's antennae [35], [36] (see Figure 2.10). It has been proven that insects use their antenna mainly as their olfactory system.

One of the possible applications for biological sensors using the electroantennography technique is in the area of forest pest management. A variety of insects are considered pests in the forest, and are responsible for damage of many trees in North America each year. Traps are commonly used to capture and destroy these pests, with the opposite sex pheromone substance as the bait. Hence, synthesizing the insect's pheromone remains one of the challenges that must be solved to achieve better pest control in forests. A standard GC technique with an FID detector is only capable of

detecting the major components of the pheromone and the minor components will go undetected, mostly due to relatively low its sensitivity. On the other hand, the insect's olfactory system is a very sensitive and selective detector, able to detect a situation when all the major and minor components of a pheromone exist in the right proportion. For this reason biological detectors that integrate gas chromatography with selective electroantennagraphic detectors become the best candidate for miniaturization and mass-fabrication using technologies normally reserved for integrated circuits (ICs).

The sensitivity and selectivity of the insects' antennae as a biological detector has been demonstrated, and compared with an FID's response [37]. The schematic representation of the experiment setup is shown in Figure 2.11(a) and picture of the experimental setup in Figure 2.11(b). The results of one such biological sensor are shown in Figure 2.12 and can be used to discuss the sensitivity and selectivity of the insect's

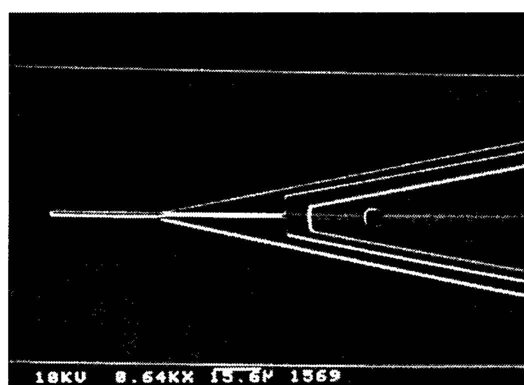

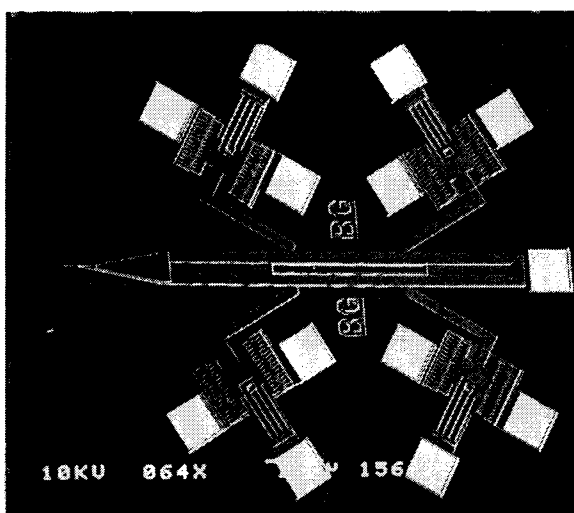

(a) (b)

Figure 2.13 (a) A SEM picture of a MEMS probe's tip, (b) and the actuation system[37].

antenna as compared to the response from an FID detector. As can be seen from the recorder plot, there are major and minor chemical components in the pheromone sample. In addition, the known impurities in the sample have been also detected. However, the response from the EAD shows that there is one major and three minor components. The major component is the one whose concentration in the pheromone sample is the largest, and the minor components are the ones with the lowest concentration. One thing which seems to be very remarkable in the EAD response is the fact that all impurities which were insignificant to insects were not detected by the EAD, and were totally ignored, whereas the four main chemical components in the pheromone (represented by A, B, C and D arrows in Figure 2.12) were detected. This is in contrast to the FID response where two components out of the four (one major and one minor) were detected, and with much smaller sensitivity. The above result shows that biological detectors using insect antenna are very selective and sensitive. Since the FID detector is unable to detect all the necessary components to synthesize a given pheromone, then the use of insects as detectors is beneficial. There is an ongoing research to find the most effective method to obtain the signal generated by the neural cell in the insects' antennae. One such example is to use microprobes fabricated by surface micromachining techniques. This probe is shown in Figure 2.13. As can be seen from the SEM picture (Figure 2.13(b)), the design consists of two parts: a microprobe which is attached to a slider and a set of four electrostatic comb resonators (which are referred to as impact actuators). These impact actuators have an impact arm attached onto their movable parts and use them to drive the probe on the slider through inclined impacts [38]. The principle of operation of the impact actuators is described in [39].

2•4 Summary

In summary, a literature review of current conventional detectors used in gas chromatography system has been presented. The choice of the detector is based on the required fabrication simplicity and the type of gases to be detected (by the conventional way). One of the main objectives is to be able to perform the miniaturization task by micromachining techniques mainly to lower the cost of manufacturing and improve the reproducibility of the devices. However, there exist major technological problems with miniaturization for each of these detectors. Some of them require radioactive materials for ionization of the sample gas, whereas the others are selective to one or two particular gases. And finally, biological sensors are effective mainly for detecting the insect's pheromone.

Chapter 3

Principle of Field Ionization

From the previous chapter's discussion, it is clear that most conventional detectors suffer from complex manufacturing technology and miniaturization by micromachining techniques is hardly possible. For this reason, they are not going to be considered as possible candidate detectors for the micromachined gas chromatography column. On other hand, a detector based on field ionization is by far the most suitable choice among the detectors. One of the reasons which makes the field ionization detector a more attractive choice for this research is its simplicity of being microfabricated in a series of simple sequences. The microfabrication techniques described in this thesis can be performed with standard micromachining processes which are widely available at most microfabrication laboratories.

In the simplest example of field ionization, two conductive materials (anode and cathode) are separated from each other by a certain gap holding the sample gas. The essence of the design is to make the anode electrode sufficiently sharp to be able to ionize the sample gas molecules on contact at a relatively small applied voltage. In this chapter we proceed with development of the fundamental principle of field ionization for detection of sample gases and establishment of electric conduction through gases ionized by these devices.

3•1 Theory of Field Ionization

Before the principle of field ionization can be explained, it is necessary to describe briefly the field emission process. This is because field emission structures are more established devices in microelectronic industries. These structures have been used for a number of years as sources for various applications, such as scanning electron microscopes and atomic force microscopes. They are now being investigated for a wider field of application, such as flat panel displays, vacuum microelectronic devices, and chemical detectors by field ionization.

3•1•1 Field Emission

Field emission structures consist of very sharp points (typically less than 100 nm radius) made out of field emission materials. These sharp points, when biased at a negative potential, and concentrate the electric field at their sharpest point. This high electric field allows the electrons to *tunnel* through the tip material into surrounding space, normally maintained under high vacuum conditions. The magnitude of the potential required to produce sufficiently strong electric fields is proportional to the distance between the tip and the principal counter electrode as well as the sharpness of the tip. While this counter electrode can be a separate structure, a minimum potential can most conveniently be obtained by physically integrating the counter electrode directly with the field emission cathode tips. This produces very small counter electrode-tip distances which are physically locked in proper alignment. Field emission cathode structures both with and without integrated counter electrodes are useful electron sources in a variety of present and future potential applications such as flat panel display, vacuum microelectronic devices and various electron microscopes. The field emission display elements that utilize

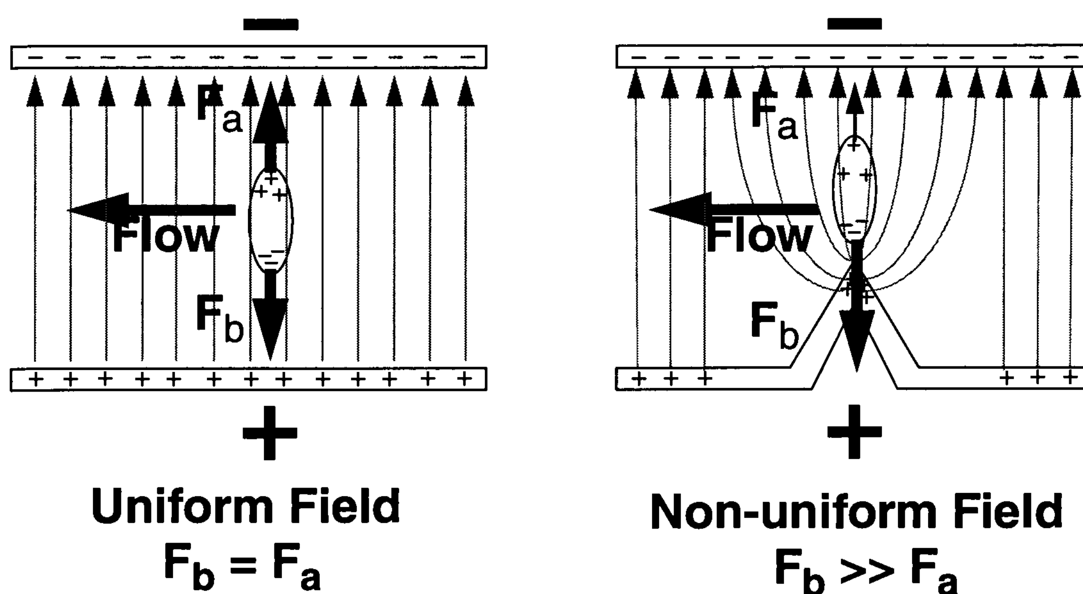

Figure 3.1 Schematic representation of the field ionization process.

these cathodes use the basic field emission structure and add additional structures, such as an extension of the vacuum space, a phosphor surface opposite the cathode tip, and additional electrodes to collect and/or control the electron current.

3•1•2 Field Ionization

In the case of the field ionization, the mechanism is basically the reverse process of field emission in the sense that the process involves the tunneling of an electron from the outer orbit of the molecule in proximity to the sharp tip into the metal.

This can be explained by examining Figure 3.1(a)-(b) and Figure 3.2(a)-(c). When an uncharged molecule enters into a region between two parallel electrodes where there is uniform electric field, as shown in Figure 3.1(a), the uncharged molecule experiences polarization. This means there will be a transfer of charge within the particle so that one end of the particle becomes negative and the other positive. The particle in the electric field thus becomes a dipole. As a result there will be a force acting on each end of the

dipole. Because the field is uniform, the two forces (F_a and F_b) will be the same in magnitude but in opposite directions. The resultant force is zero and so the polarized molecule passes through the region between the two electrodes unaffected.

In situations where the electric field distribution in the region between the two electrodes is non-uniform, as shown in Figure 3.1(b), the entire dipole will experience a net force toward the stronger region of the field. The dipole will then move in the direction of the field gradient, and almost along the field lines. Under such conditions, the dipole will attach itself to the tip. When the field intensity is high enough, electrons can be extracted from the negative end. In cases where an electron is emitted from the dipole, the rest of the molecule becomes positively charged and experiences a force in the direction of the electric field to the opposite electrode.

The principle of field ionization developed by Müller *et al.* [40] may be discussed with the aid of a potential energy diagram. When this atom is brought in close proximity to an unbiased, ideally smooth metal surface (as shown in Figure 3.2(a)), the vacuum level of the atom and the metal electrode are aligned. The conduction band of the metal is filled with electrons up to the Fermi level E_F. An amount of energy equal to the work function $q\phi$ must be transferred to an electron at the Fermi level to be removed from the metal into the vacuum level. An ionization energy of qV_I must be supplied to an electron to move it to a vacuum. Now, when an external field is applied to the system, as shown in Figure 3.2(b), the energy level of the valence electron in the gas molecule is raised to the metal Fermi level. At this point, the atom will be at its minimum distance from the metal surface, due to attraction force. Under these circumstances, the potential energy barrier between the molecule and the metal has a width of only a few angstroms and a height of only a few

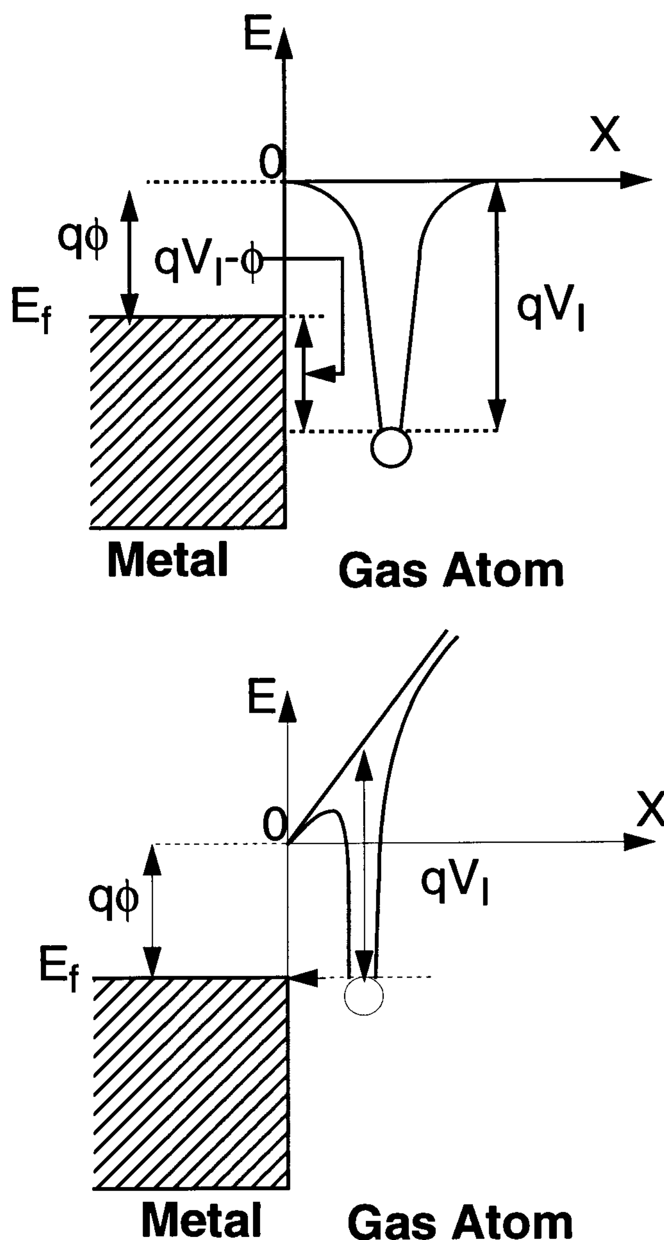

Figure 3.2 The energy diagram of an atom in proximity of metal [41].

electron volts. Therefore, there exists a finite probability for the electron to penetrate through this barrier via quantum mechanical tunnelling with which the electron strikes the barrier, in a direction normal to it, from inside the atom. This probability is a function of the metal material and the type of gas which is being analyzed.

3•2 Field Ionization Current

Having explained the principle of the field ionization detector, it is straightforward to classify it as an electrochemical gas detector. And, like most electrochemical detectors its current-voltage characteristics are based on the similar principle. In most electrochemical detectors, a chemical reaction has to occur at the interface in order for electric current to pass between the electrodes. This current is referred to as the faradaic current [47]. Generally, the faradaic current is controlled by two important mechanisms which comprise the total generated current, depending on the type of the detector, and one of the mechanisms is the dominating one. The two mechanisms are as follows [47]:

1. Diffusion-limited electrode reaction
2. Electron-transfer-limited electrode reaction

3•2•1 Diffusion-Limited Electrode Reaction

The mechanism which controls the current in most chemical detectors, is the diffusion-limited electrode reaction. Under this mechanism, current can flow only as fast as the gas/liquid molecules can reach the surface. Under this diffusion mechanism, the molecules move from a region of high molecular concentration to a region of low concentration. This is the preferred situation for analytical measurements. This mechanism of current flow can only be measured when an important condition is fulfilled; namely, that the rate of reaction at the electrode, and hence the current flowing, is exclusively determined by diffusion [47]. This condition is usually fulfilled when the detector is dealing with a liquid analyte. This is because the diffusion constant of liquid analyte is normally around $D_{water} \approx 2.5\times10^{-5}$ cm^2s^{-1}. This small value means that the rate of diffusion in a static medium is rather slow, and makes this mechanism to dominant

in current flow. However, for gas molecules the diffusion constant is higher and so they move much faster than in a liquid; for example, the O_2 diffusion constant at room temperature in N_2 gas is $D_{oxygen} \approx 0.16\ \text{cm}^2\text{s}^{-1}$. As a consequence, this mechanism is not a dominant are in a gas analyte. Otherwise, no simple analytical relation between analyte concentration and current through the gas sample exist [47].

3•2•2 Electron-Transfer-Limited Electrode Reaction

In this type of reaction the rate-limiting step is not the diffusion of species to the electrode but the rate of electron transfer between the electrode and analyte in the chemical sample (in this case, gas). In order to derive the current-voltage characteristic of this reaction there are two assumptions that have to be taken. Firstly, it is assumed a first-order reaction so that the probability of electron transfer in or out of the electrode is proportional to the concentration of the available species (e.g., gas sample) at the

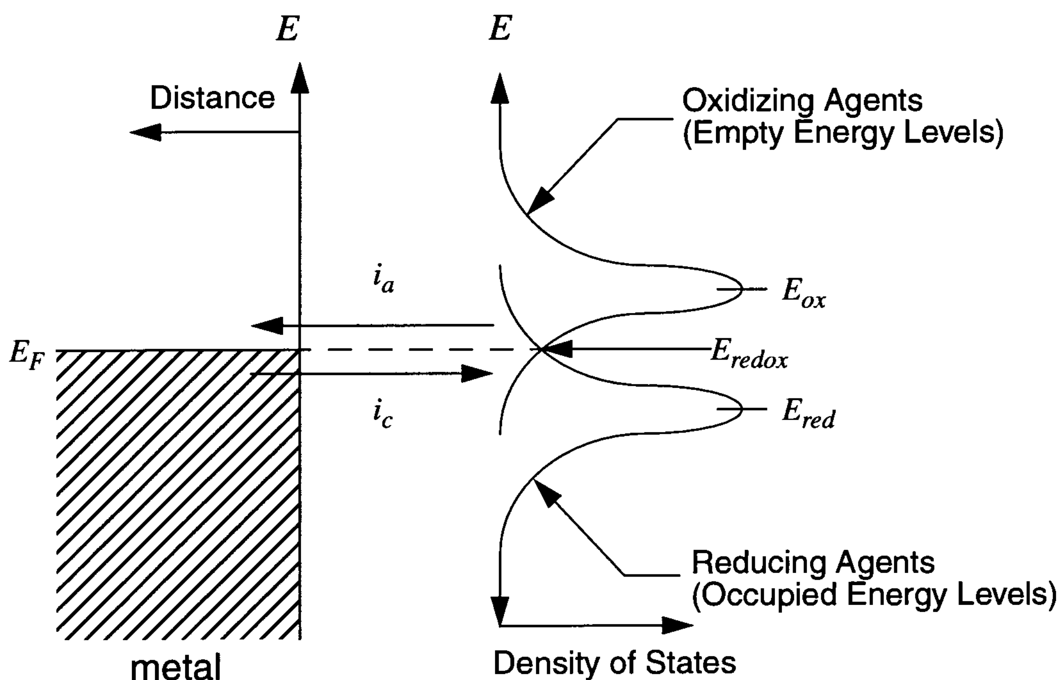

Figure 3.3 The band model for the metal/analyte interface with one-electron in equilibrium [47].

proximity of the sharp tip [47]. Secondly, it is assumed an isoenergetic electron transfer, meaning that the electron must tunnel between the electrode and the gas molecule potential barrier without a change in its initial energy value (radiationless electronic transfer) [47]. Thus, *available molecules* are then oxidizing agents whose energy levels are isoenergetic to the levels in a filled band (in case of the metal any energy levels below Fermi level). In this case, the process is referred to as Oxidation (O). Or, the molecules are reducing agents, and then their occupied energy levels are isoenergetic to the unoccupied levels in the electrode (in case of the metal, any energy level above the Fermi level). This process is referred to as Reduction (R). The first step is to calculate the density of the energy levels.

For this purpose, the Marcus-Gerischer model of energy levels in analytes is used [47] and is shown in Figure 3.3. In the right-hand side of the figure, the density of energy levels $N(E)$ in the analyte for a one-electron reactant is plotted versus energy E of the levels.

As can be seen from the Figure 3.3, there are the energy values of E_{ox} and E_{red} where the density at these levels are at their maximum. Hence, the electrons in these energy levels have the most probable chance to make the transition to/from the metal electrode. The left-hand side of the Figure 3.3 represents the band diagram for the metal. Having a prior knowledge of the most probable energy values E_{ox} and E_{red}, one can calculate the probability distribution of the energy levels. According to the Marcus-Gerischer model, this is given by [47]:

$$W(E, E_t) = \frac{1}{\sqrt{(4\pi kT)}}\exp\left[-\frac{(E_t - E)^2}{4\lambda kT}\right] \tag{3.1}$$

where E_t is the most probable energy value, in this case E_{ox} and E_{red}, and λ is the *reorganization* energy, a parameter that normally has a value between about 0.4 and 3eV. The relation between $W(E, E_t)$ and $N(E)$ in Figure 3.3 is given by:

$$N(E) = \alpha c W(E) \tag{3.2}$$

where α is a constant related to the quantum mechanical tunneling of an electron through the potential barrier due to a high electric field between the metal tip and analyte, and αc is the total density (per unit area) of molecules in close proximity to the field ionization tip for participation in electron exchange. The anodic current i_a will be given by an expression of the form:

$$i_a = Ac_a \int_{E_F}^{\infty} W(E, E_a) dE \tag{3.3}$$

and the cathodic current is given by an expression of the form:

$$i_c = Bc_c \int_{0}^{E_F} W(E, E_c) dE \tag{3.4}$$

where the c 's represent concentration and A and B are constants. The integration is over energy levels in the analyte that are isoenergetic with unoccupied (anodic) or occupied (cathode) energy levels in the metal. It is clear by inspection that the net current:

$$i_{net} = i_a - i_c \tag{3.5}$$

will be zero when E_F is somewhere near the energy E_{redox} at which

$W(E_F, E_{ox}) = W(E_F, E_{red})$. Since E_F is related to the work function of the metal and E_{redox} is loosely related to the energy required to remove an electron from the analyte to infinitely; normally, the two levels cannot be expected to line up as in Figure 3.3 without a charge exchange.

When the energy levels do not line up, once the electrode is first immersed in the analyte with no voltage applied, but misaligned as shown in Figure 3.4, then there will be an isoenergetic transition of electrons to empty levels in the metal. A Helmholtz double-layer voltage will develop in such a way as to raise the Fermi level in the metal relative to an E_{redox} level in the analyte. The isoenergetic transition will continue until the Figure 3.4 is changed to Figure 3.3. The exact value of Helmholtz double-layer voltage is not measurable because of the lack of any information in determining the potential in the

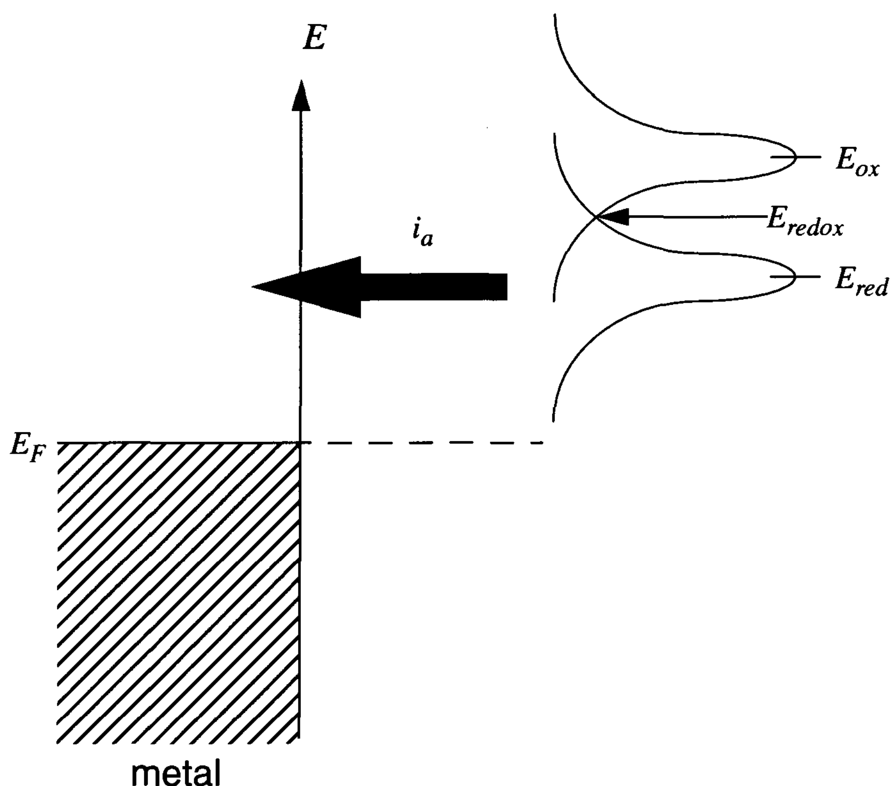

Figure 3.4 The band model for the metal/analyte interface with metal electrode and analyte in non-equilibrium [47].

analyte. A similar argument is applicable when the analyte and metal have the band diagram shown in Figure 3.5. In this case, the Fermi level has to be lowered with respect to the analyte E_{redox} level.

Therefore, when there are no net current flows, the difference between the double-layer voltage between the two electrodes is the redox potential V_{redox}, which can be measured and is usually nonzero. At a different applied voltage, V_{app}, relative to a counter electrode, the voltage across the two electrodes is η. This is defined as an *overvoltage* η [47]:

$$\eta = V_{app} - V_{redox} \tag{3.6}$$

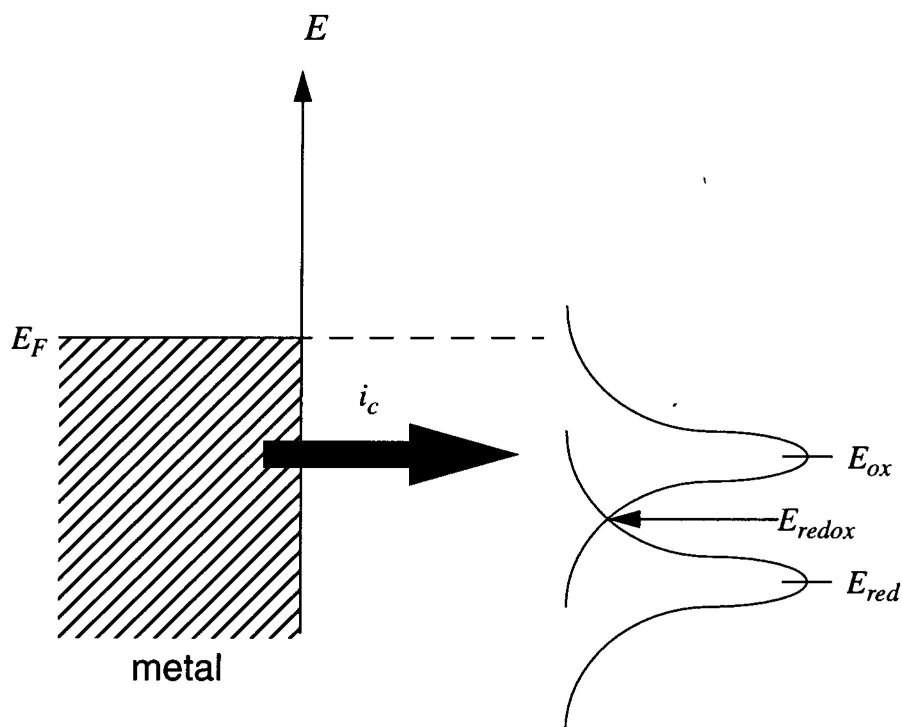

Figure 3.5 The band model for the metal/analyte interface with metal electrode and the analyte in non-equilibrium [47].

As η changes from zero, there is a shift in potential in the metal and, hence, in the Fermi energy in the metal relative to the energy levels in the analyte. This shifts the overlap integrals and, through (3.3), (3.4) and (3.5), the net current i_{net}.

Because in metal electrodes, the overlap of filled and empty states is dominantly near E_F (see Figure 3.3), the integrals in (3.3) and (3.4) can be expressed as:

$$i_a = Ec_{red}\exp\left[-\frac{(E_{red}-E_F)^2}{4\lambda kT}\right] \tag{3.7}$$

$$i_c = Fc_{ox}\exp\left[-\frac{(E_{ox}-E_F)^2}{4\lambda kT}\right] \tag{3.8}$$

Now, when $c_{red} = c_{ox}$ we have by symmetry $i_{net} = 0$, assuming $E \approx F$. It can be shown that by a first-order approximation ($E \approx F$ and $E_F = E_{redox}$), E_{redox} is given by [48]:

$$E_{redox} = E_{red} + \lambda + kT\ln\left(\frac{c_{red}}{c_{ox}}\right) = E_{ox} - \lambda + kT\ln\left(\frac{c_{red}}{c_{ox}}\right) \tag{3.9}$$

Since E_F changes linearly with the voltage, relative to E_{redox}, we can write:

$$E_F = E_{redox} - \eta q \tag{3.10}$$

where q is the electronic charge (inserted to represent η in terms of energy in eV). The η will modulate the field in the Helmholtz double layer and change the net rates and directions of electrode reactions. Consider Figure 3.4, for a positive voltage value of η, by equation (3.10), it will appear between E_F, metal and E_{redox} and will cause a high anodic current as indicated in the figure.

With all these equations inserted into (3.7) and (3.8), we can show [48]:

$$i_{net} = E\left\{c_{red}\exp\left(\left[-\frac{\left(\lambda + kT\ln\left(\frac{c_{red}}{c_{ox}}\right) - \eta q\right)^2}{4\lambda kT}\right] - c_{ox}\exp\left[-\frac{\left(\lambda - kT\ln\left(\frac{c_{red}}{c_{ox}}\right) + \eta q\right)^2}{4\lambda kT}\right]\right)\right\} \quad (3.11)$$

where $\lambda \gg \eta q$ and $\lambda \gg kT\ln(c_{red}/c_{ox})$, as is normally the case for one-electron reactions; this equation simplifies to the Butler-Volmer equation [47]:

$$i = i_0\left[\exp\left(\frac{\alpha\eta q}{kT}\right) - \exp\left(-\frac{\alpha\eta q}{kT}\right)\right] \quad (3.12)$$

which is the complete current-potential characteristic. Here i_0 represents a collection of constants and is the value of i_c and i_a at $\eta = 0$. The factor α in the exponent is called transfer coefficient and can range in principle from 0 to 1, although for metals, it is normally near $\frac{1}{2}$ and is the number of electrons involved in the electrochemical reaction. A plot of $\log i$ versus η, known as a Tafel plot, is a useful device for evaluating the above kinetic parameters [49].

3•3 Summary

In this chapter, the principle of field ionization was established. With the discussion of the field ionization principle, it is apparent that a gas detector based on the field ionization process requires a sharp metallic tip and the gap between this tip and a preferable counter electrode has to be small to reduce the applied potential. The current-voltage characteristic of this type of detector is established to be exponential. The next chapter deals with the micromachining tools we have to fabricate sharp tips to build a field ionization gas detector.

Chapter 4

Micromachining Processes

For the microfabrication of a miniaturized field ionization detector, the primary microfabrication tools used in its manufacturing are wet chemical etching (both isotropic and anisotropic), a generic electroplating process with or without a photoresist mold (for thick film deposition) and counter electrode epoxy bonding (as a means for sealing the top lid). In the following sections, each of these processes is discussed in relation to its ultimate goal, which is to facilitate the fabrication of the miniaturized field ionization detector. In addition, there is thermal oxidation of silicon wafers (by wet oxidation) to grow insulation, and thin film deposition of metal layers (as a means to uniformly coat surfaces) both of which are a part of fabrication processes and will not be discussed here. The recipe for these standard processes appears in Appendix A.

4•1 Micromachining

Silicon micromachining is, as its name implies, the fabrication of very small three-dimensional mechanical structures on a silicon substrate. However, micromachining, in the broadest sense, is the production of artifacts in which at least one dimension is controlled to a scale of a few micrometers or better. In practice, much micromachining derives from the use of photolithographic techniques used in the semiconductor industry.

Nevertheless, recently there has been a huge increase in micromachining applications. As a result, technologies are being developed and adapted specifically to micromachining. In addition, advances in integrating microelectronic circuits with

micromachining devices allow manufacturing innovative micromachining systems able to perform complex tasks in scientific laboratories that were previously impossible to do due to lack of miniaturized tools. Investigating certain properties for analytical chemistry requires development of novel microtools that can function and perform well within the constrained size. Some of the innovative micromachining systems being developed include: pumps [51], valves [52], accelerometers [53], fluid density sensors [54], pressure sensors [55], radiation sensors [56], biological detectors [37], electrostatic motors [57], gyroscopes [58] and sub-nanogram mass measurement systems [59].

Although the micromachining technique consists of a variety of methods, for the purpose of the present research, micromachining refers exclusively to the modifications performed on a substrate's surface by etching. There are two major families of etching processes used to accomplish micromachining. These include: wet chemical etching and dry etching. Of these two techniques, the simplest to implement is wet chemical etching. Thus, in the interest of developing a straightforward low-cost fabrication, the simplest technique that could accomplish the objective was selected. As will be demonstrated, wet chemical etching was the fundamental tool used to fabricate the micromachining devices in this thesis.

Since the wet chemical etching of silicon is well characterized, and it has had a demonstrated reproducibility in SFU laboratories, it was chosen as the etching technique for this research. In general, wet chemical etching involves three major steps, and is summarized by Williams [60]: (1) the etchant species reach the surface, (2) the appropriate reaction occurs and (3) the resulting product is removed from the surface.

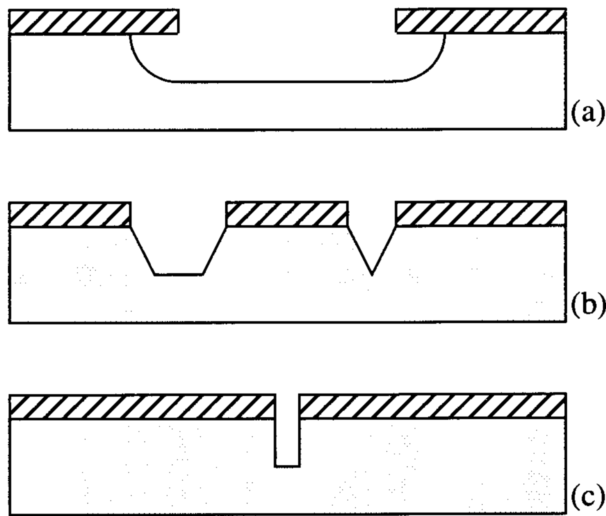

Figure 4.1 The etching profile for: (a) (100) oriented silicon anisotropic etch, (b) (110) oriented silicon anisotropic etch and, (c) silicon isotropic etch [61].

Wet chemical etching as a process can be divided further into two sub-groups: isotropic and anisotropic. In an *isotropic* etch, the etch rate is limited by diffusion which is the rate at which reactant species can reach the surface and there are no significant differences between the etched crystal orientation. In other words, an isotropic etch proceeds at the same rate through the material, yielding the profile shown in Figure 4.1(a). On the other hand, an anisotropic etch possesses an etch rate that is reaction-rate-limited meaning how fast the chemical can react with the crystal plane. It tends to etch the surface at different etch rates relative to the crystallographic orientation of the material, yielding a profile which is significantly different, as shown in Figure 4.1(b and c). As the anisotropic etching is the process which is used to process the devices in this thesis, it is described further in detail.

4•1•1 Anisotropic Etching

As the wet chemical anisotropic etching mechanism is based upon a differential

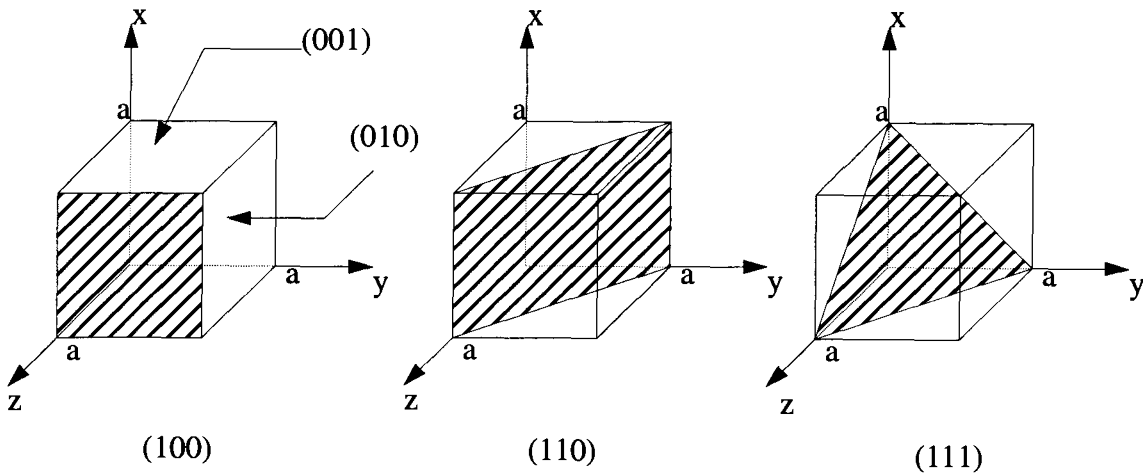

Figure 4.2 Miller indices of important silicon crystal planes with lattice constant 'a' [24].

etch rate between crystallography planes within a single crystal silicon wafer and being one of the vital steps in the microfabrication process of field ionization tip, it is important to review the silicon crystal structure. There are a number of different planes in the silicon crystal structure. However, in micromachining there are three planes which are critical to wet chemical etching. These planes are shown in Figure 4.2, together with their Miller indices.

Property	Crystal Orientation		
	(100)	(110)	(111)
Atomic Density [x10^{14}/cm^2]	6.78	9.59	15.56
Available Bond Density [x10^{14}/cm^2]	6.78	9.59	11.76

Table 4.1 Planer density properties of the major silicon planes [63].

It has been discovered that there are two primary mechanisms which are responsible for differential etching by the wet chemical anisotropic etchant. The first responsible mechanism is related to atomic density along the etch plane [50] and the

second mechanism likely involves the number of available surface bonds [63]. These results indicate that those planes which have a higher surface bond density or atomic density would etch less quickly. Table 4.1 lists the atomic and chemical bond densities for three important silicon crystal planes. These densities support the arguments that the different etch rates for common anisotropic silicon etching are a strong function of the magnitudes of the atomic and chemical bond densities. There are five wet chemical anisotropic etchants: ethylenediamine-pyrocatechol-water (EDP) [65], [67], [68], [69], [70], [71], tetramethylammonium hydroxide (TMAH) [72], [73], hydrazine-water solution [74], potassium hydroxide-water (KOH) [69], [75], [76] and cesium hydroxide-water (CsOH) [78]. Of these etching systems, EDP was selected for several reasons. Firstly, it has been successfully used in the School of Engineering's microfabrication laboratory[1] for several years. Secondly, the EDP system has a superior differential etch rate compared to the TMAH and KOH. Compared with KOH, EDP has minimum contamination with sodium or potassium. What is even more important, the etch attacks the silicon dioxide mask very slowly. The etch rates ratio of silicon and silicon dioxide using KOH can be as large as 400:1 [71] (1μm/min of silicon) which is much smaller than the EDP solution or even TMAH. Finally, its performance is well characterized for various temperatures and concentrations [79]. On the bad side, EDP is a highly toxic and corrosive solution.

EDP was introduced in 1967 [65]. The chemical mechanism for the anisotropic etching of silicon by EDP which was proposed by Finne *et al.* [65], is still used today to describe the chemical reaction that takes place. According to this theory, ethylenediamine with molecular formula $NH_2 - CH_2 - CH_2 - NH_2$ and water, oxidize the silicon surface

1. School of Engineering Science, Simon Fraser University, Burnaby, BC, V5A 1S6, CANADA.

to hydrated silica, and pyrocatechol with molecular formula $C_6H_4(OH)_2$ plays the role of a complexing agent, which makes the hydrated silica soluble in water. The overall reaction was represented as

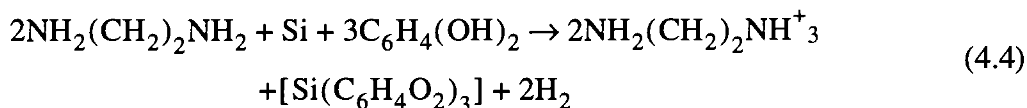

$$2NH_2(CH_2)_2NH_2 + Si + 3C_6H_4(OH)_2 \rightarrow 2NH_2(CH_2)_2NH^+{}_3 + [Si(C_6H_4O_2)_3] + 2H_2 \quad (4.4)$$

The optimum composition suggested in [66] is of the following proportion: (ethylenediamine (liquid): water (liquid): pyrocatechol (solid), 17ml: 8ml: 3g). which gives an etch rate close to the maximum etch rate. This composition of etch is called EDP type T [66]. The exact chemical and its ratio is unknown for the commercial solution used at SFU's laboratory due to the manufacturers' proprietary information. However, it is believed, due to many years of silicon etching, that it closely resembles EDP type T. The

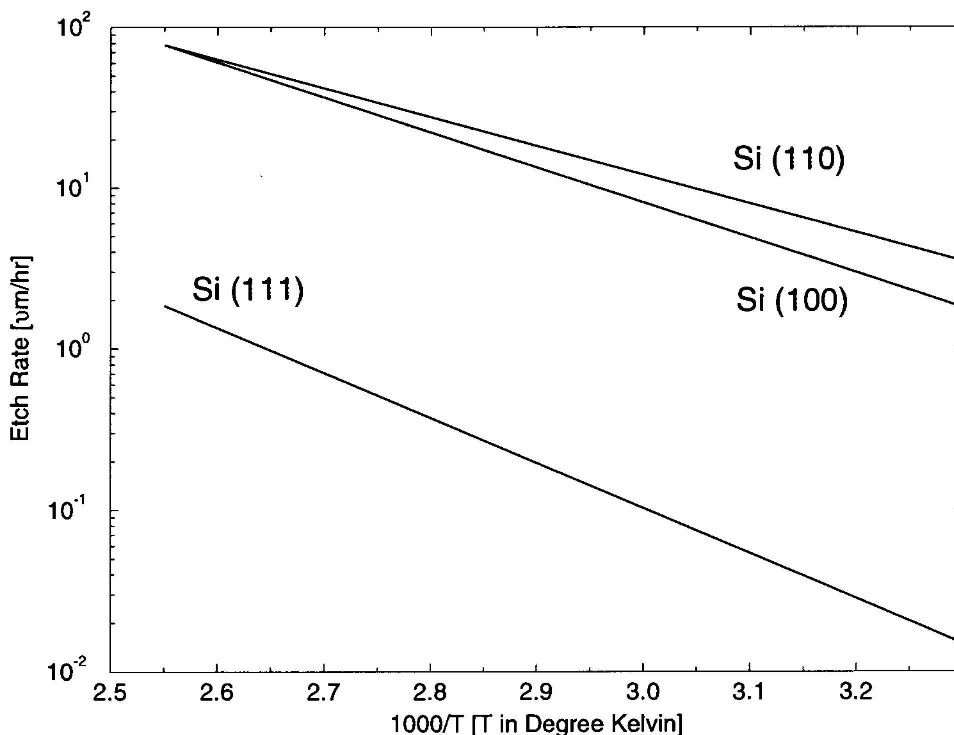

Figure 4.3 The rate of silicon in EDP versus temperature [79].

graph shown in Figure 4.3 represents the etch rate of various silicon planes at different temperatures.

Mole Fraction H_2O	Etch Rate [μm/h]
0.0	0.0
0.2	7.5
0.4	16.0
0.6	22.5
0.8	15.0
1.0	0.0

Table 4.2 Etch rate of silicon as a function of the water content of the etch, with the pyrocatechol content held constant [65].

Table 4.2 shows the etch rate of silicon as a function of the water content of the etch. A maximum limit can be observed for the etch composition, corresponding to a mole fraction of 0.6 water. The silicon etch rates fall to zero for solutions with mole fractions of water equal to one and zero [65]. The approximate etch rates EDP for a variety of boron concentrations and temperatures are shown in Table 4.3. From this table, it becomes apparent that if the boron concentration in Si is below $1\times10^{16}cm^{-3}$, then EDP is going to have a high etch rate for the temperatures evaluated [79] (see Figure 4.4). However, before an operating point is identified, a careful examination of the silicon dioxide etch rate must be accomplished. The reason the silicon dioxide etch rate is very important in this research work is because the silicon etch process will be in the order of several hundreds of micrometers deep. Therefore, it is absolutely necessary to know the amount of silicon dioxide etched by EDP.

B [dopant/cm^3]	70°C	80°C	90°C	100°C
1.0×10^{16}	0.0	15	25	28
3.3×10^{16}	4.1	6.4	10	15
4.4×10^{16}	1.8	2.4	4.0	4.8
7.0×10^{16}	0.24	0.40	0.60	1.0
9.0×10^{16}	0.08	0.14	0.21	0.27

Table 4.3 Approximate silicon (100) etch rates (μm/h) for various boron dopants and temperatures [79].

Table 4.4 summarizes the silicon dioxide etch rates for the same condition reported in Table 4.3 [79]. For all anisotropic etchants, (111) crystal planes expose the slowest etch rates, being approximately two orders of magnitude smaller than other principal crystal

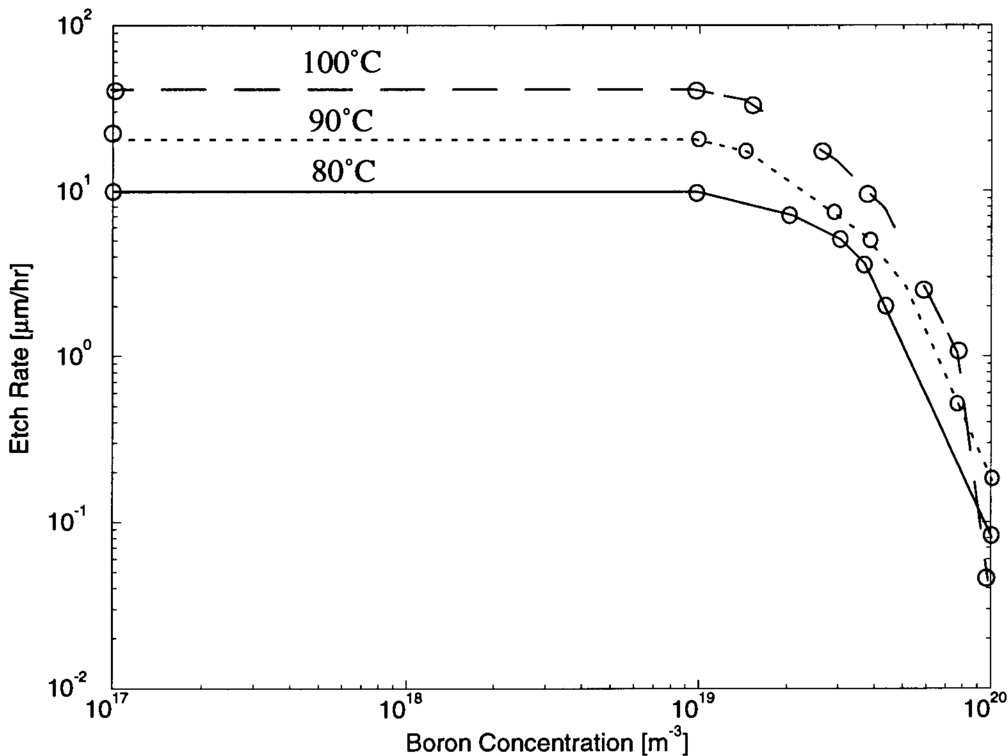

Figure 4.4 Silicon {100} etch rate in EDP versus boron concentration for a few different temperatures [79].

directions. For EDP solutions the temperature dependence of vertical (100) and (110) etch rates, as well as the lateral (111) etch rate, as determined on (100) wafers, is shown in Figure 4.3 [79]. Although all etch ratios in Table 4.4 are greater than the $2x10^4$ ratio associated with the anisotropic etch process, the total silicon dioxide thickness required to accomplish a deep silicon etch could then exceed any reasonable thickness of thermally grown silicon dioxide. Since the silicon wafers used in this research were in the order of 550μm thick, the worst case of oxide thickness would still be sufficient to allow etching through the wafer. Knowing the length of time that silicon dioxide must survive is a

Etch Ratio (Si/SiO_2)	Temperature [°C]
$7.0x10^4$	60
$5.0x10^4$	70
$3.5x10^4$	80
$2.0x10^4$	90
$1.8x10^4$	100

Table 4.4 Ratio of the (100) Si/SiO2 etch rate as a function of temperature [79].

straightforward calculation (using the values in Table 4.4) to determine the silicon dioxide's required thickness.

4•2 Anisotropic Etching Profile

All anisotropic etching systems share a common feature, since they result in the intersection of the (100) surface by (111) plane. For silicon, the angle ϕ_α between two planes $(h_1k_1l_1)$ and $(h_2k_2l_2)$ is given by the following equation [62]:

$$\phi_a = \arctan\left(\frac{h_1h_2 + k_1k_2 + l_1l_2}{(\sqrt{h_1^2 + k_1^2 + l_1^2})(\sqrt{h_2^2 + k_2^2 + l_2^2})}\right) \tag{4.5}$$

From equation (4.5), the angle ϕ_α, which is between the (100) and (111) plane, can be calculated to be approximately 54.74°. There are three basic etch profiles which are important in the design of a micromachined field ionization tip: the inverted pyramid, the feedthrough features and the inverted truncated pyramid. These have been discussed by Reston [24].

4•2•1 Inverted Pyramid

The inverted pyramid shown in Figure 4.5 is typical of an inverted anisotropic etch on (100)-oriented silicon. This structure occurs because at the point where (111) planes intersect (100), the etch rate decreases to approximately 5% of the values associated with the (100) plane [24]. The depth of the pit, d_p, can be calculated from the width of the silicon dioxide mask W_m, (or conversely, the silicon dioxide mask's width can be calculated from a specific etch depth), using the following relationship [24]:

$$d_p = \left(\frac{W_m}{2}\right)\tan 54.74° \tag{4.6}$$

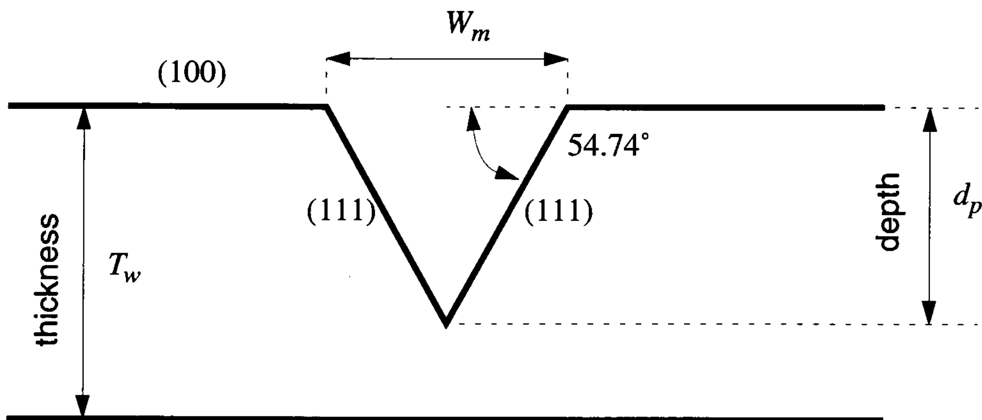

Figure 4.5 Cross-section view of a typical inverted pyramidal pit [24].

As an example, a pit 500 μm deep requires a silicon dioxide mask that is approximately 700 μm wide.

4•2•2 Feedthrough Feature

The feedthrough feature is similar to a very deep inverted pyramid, as can be seen from Figure 4.6. However, the most important difference is that the feedthrough extrapolated etch depth is actually greater than the wafer thickness. This feature is the essential part of the micromachined tip to be discussed in the fabrication chapter (Chapter 5). Therefore, in order to determine the width of the hole that will appear at the bottom of the wafer, it is necessary to examine the geometry involved. Figure 4.6 illustrates the geometry of a typical feedthrough feature's etch.

The single triangle 123 in Figure 4.6 is a right-angle triangle with $\angle 312 = 54.74°$; the following relationship thus holds:

$$\tan 54.74° = \frac{d_p - T_w}{W_{hole}/2} \qquad (4.7)$$

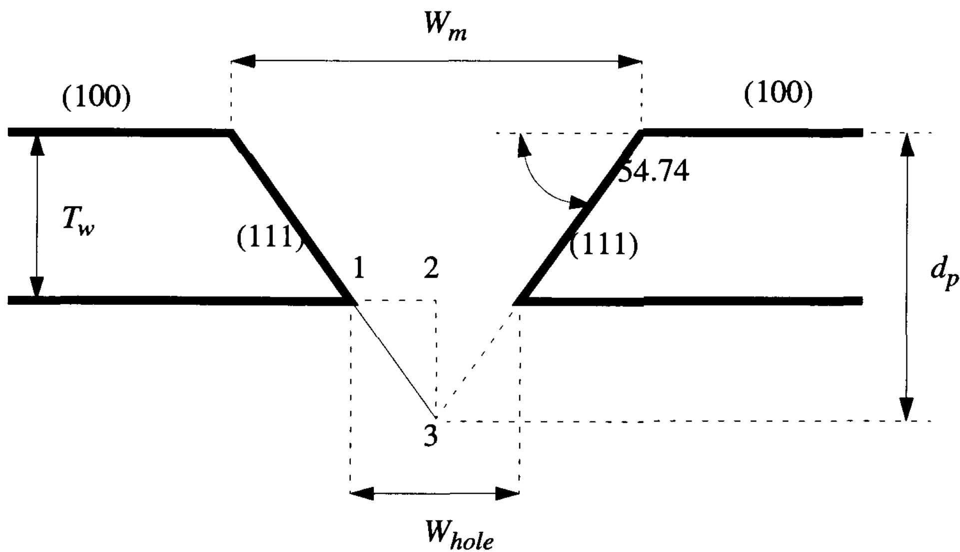

Figure 4.6 Cross-section of a typical feedthrough feature etch [24].

Since d_p is defined by (4.6), then by substituting and solving W_m, we get [24]:

$$W_m = W_{hole} + \frac{2T_w}{\tan 54.74°} \quad (4.8)$$

As an example, if a 100 μm wide hole was required in a 550 μm thick wafer, the silicon dioxide mask aperture (W_m) would need to be approximately 878 μm wide.

4•2•3 Inverted Truncated Pyramid

The third anisotropically etched structure required for the micromachined tip design is the inverted pyramid which is terminated before the (111) planes intersect, leaving a flat bottom. This situation is depicted in Figure 4.7. Since the depth of this isothermal etch is controlled by etching time, the self-stopping properties of the (111) plane intersection cannot be used. It is important to monitor the etch time as reported in Table 4.3.

Given a desired etch depth, d_p, it is possible to calculate the required mask width,

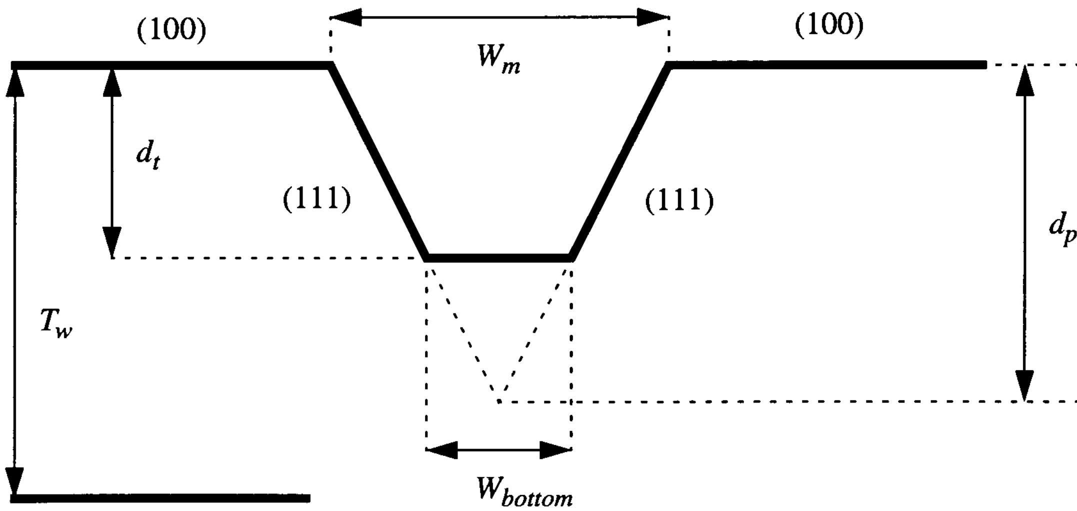

Figure 4.7 Cross-section of a typical inverted truncated pyramid feature etch [24].

W_m, for a certain bottom width, W_{bottom}, using (4.8) and substituting d_t for T_w. As an example, a 200 μm deep etch (d_t) with a bottom width of 300 μm (W_{bottom}) requires a mask width (W_m) of approximately 583 μm.

These three anisotropic etch structures, in conjunction with the isotropic oxide etch process, form the basis of the micromachining aspect of the field ionization detector fabrication. However, in order to construct a functional detector, it is necessary to deposit a thick metallic layer which can be used as an electrode. This process is accomplished by an electroplating deposition technique.

4•3 Plating

Plating is well suited as a means for depositing thick films for the purpose of making the tips, as this method of deposition is fast and allows the deposition of a wide range of metals. Alternative processes are the chemical vapor deposition (CVD) processes. These methods are limited to polysilicon with 1-3 μm thickness. There are two

methods to plate metal on the substrate: electroplating and electroless process.

The generic technique to microfabricate structures on the substrate is by means of making a mold out of photoresist material. The technique consists of four steps: (a) sputter a conductive material, known as the seed layer on the substrate; (b) microfabricate photoresist molds on the seed layer, using photolithography; (c) plating metals to fill the molds; and finally (d) removing the photoresist mold. We have selected electroplating as the method of thick film deposition to make the tip structures and Section 4•3•1 discusses the advantages and the disadvantages of the two techniques. Section 4•3•2 presents the electroplating technique in more detail.

4•3•1 Electroplating Versus Electroless Plating Process

Table 4.5 presents a comparison of electroplating and the electroless plating process. The electrical potential is the driving force for electroplating and so a conductive seed layer is needed to connect to the external power supply,to establish the appropriate substrate potential. This contact is called the *seed layer* and must be deposited in advance;

	Electroplating	Electroless
Driving force	electrical	chemical
	needs external power	no external power
	needs anode	no anode
Substrate	metal	metal, non-metal
Step coverage	conformal	conformal
Adhesion	good	poor on non-metal
Control rate	current density	not simple

Table 4.5 Comparison of electroplating versus electroless plating.

it may then be removed subsequent to plating. Providing an electrical contact to the substrate, as required in electroplating, is often seen as the disadvantage of electroplating in comparison to the electroless plating process. Secondly, although electroless plating can be performed on non-conductive substrate materials, it results in a poor adhesion which, for certain applications, such as surface micromachining, is a drawback.

Thirdly, both processes can provide a conformal coverage of the substrate topography when all parts of the surface have been catalytically activated and wetted by the solution. However, in electroplating, the step coverage is not uniform, due to the non-uniform distribution of electric potential, which is a function of geometry.

Finally, in electroplating, the rate of plating and grain size are controlled by the current density. In electroless plating, which is a fully chemical process, there are more parameters that affect the plating rate and deposition characteristics. Parameters such as pH, temperature, and concentration are very difficult to control for the best results.

4•3•2 Electroplating Process

Although the electroplating process predates most semiconductor fabrication technologies, it has not yet been characterized for micromachining application as widely as expected. It has been admitted that a particular plating cell may become well controlled by experience rather than exact science. Despite the disadvantages mentioned above, electroplating has become a very powerful deposition tool for MEMS researchers in recent years.

A simple technique such as the electroplating process provides a tremendous deposition capability which no other technique can provide. For instance, it has the capability of depositing over half of the elements in the periodic table [85]. A typical

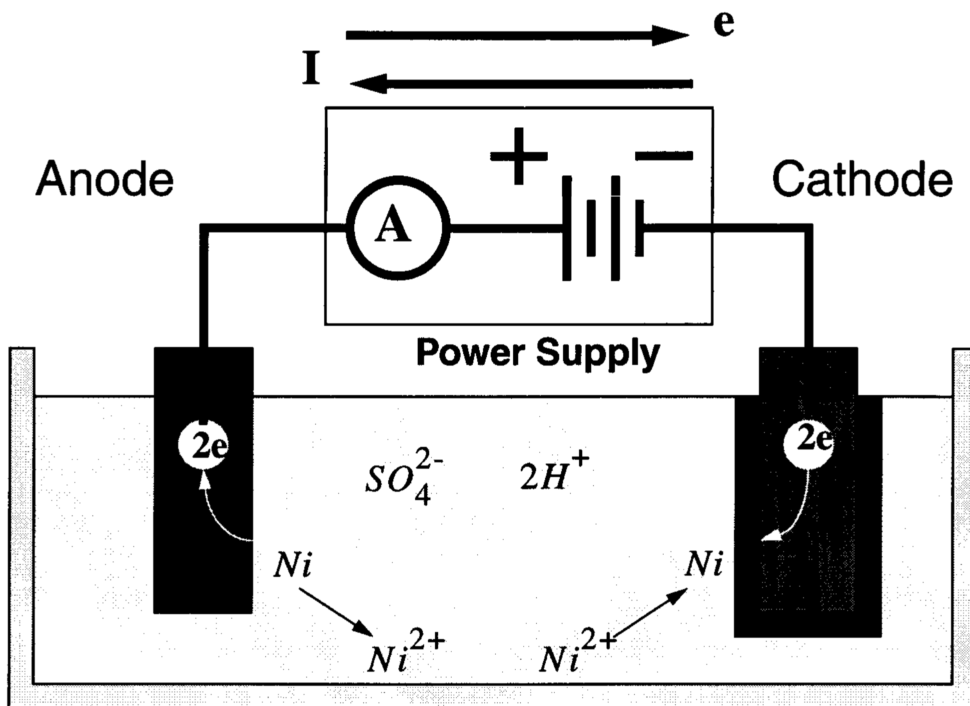

Figure 4.8 A Simplified plating cell [86].

electroplating cell consists of an anode, a cathode, an aqueous metal solution and a power supply. In the simplified example shown in Figure 4.8, the cathode is made of nickel, the anode is made of another conductive material, and the aqueous metal solution consists of nickel ions (Ni^{2+}), hydrogen ions (H^+) and sulfate ions ($SO_4{}^{2-}$). When the supply is turned on, the positive ions in the solution are attracted to the negatively biased cathode. The nickel ions that reach the cathode gain electrons, and deposit or plate themselves on the surface of the cathode, and thereby form the electrodeposit. Simultaneously, nickel is electrochemically etched from the nickel anode to produce nickel ions for the aqueous solution and electrons for the power supply.

Hydrogen ions also gain electrons from the cathode to form bubbles of hydrogen gas. These hydrogen bubbles are undesirable since they lower the plating efficiency (i.e.,

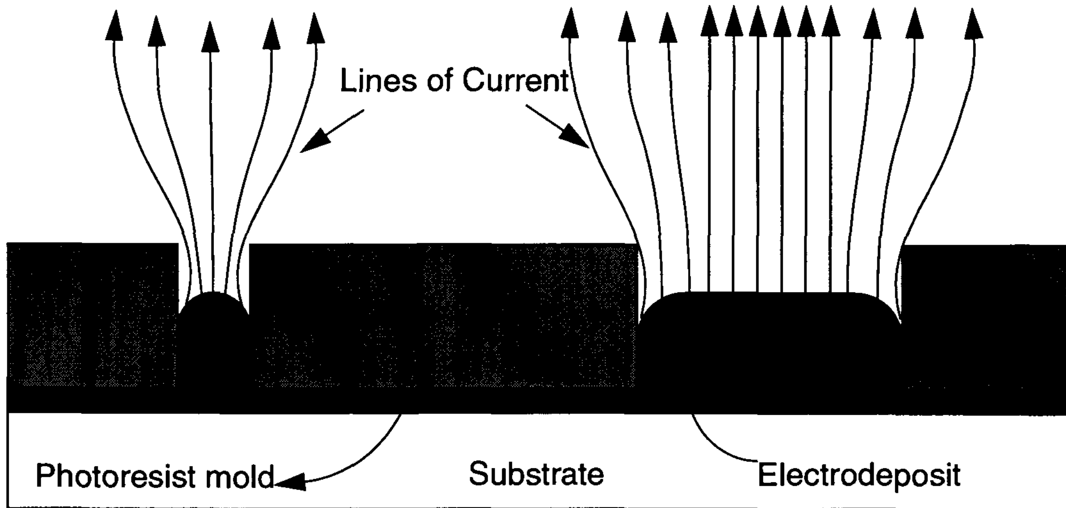

Figure 4.9 Non-uniform current densities [86].

only a fraction of the total current is used to form the electrodeposit); these bubbles can also obstruct the deposition of the intended electrodeposit.

To electroplate microfabricated structures, a conductive material is needed, which will form the cathode (i.e., the seed layer) and is a means to pattern the electrodeposit.

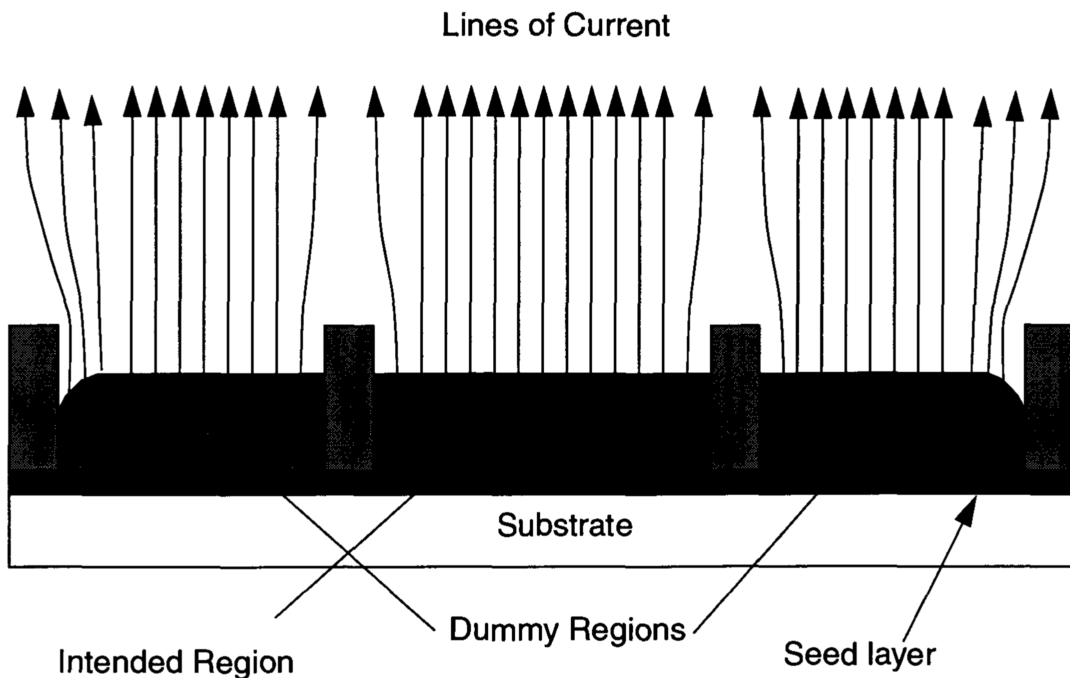

Figure 4.10 Uniform current density[86].

Typically, the electrodeposit is patterned by a selective process as opposed to a subtractive process (masking and etching). Since the localized deposition rate is proportional to the localized current density, a current density that is uniform over the entire seed layer is needed to obtain an electrodeposit with a uniform thickness. However, to achieve selective deposition, portions of the seed layer are covered with an insulating masking material which will make the current density non-uniform at its proximity. An example of the effect the plating mask has on the uniformity of the current density, and hence on the deposition rate, is illustrated in Figure 4.9. This effect becomes more noticeable the smaller the dimension of the structure. Thus, to obtain a particular deposition rate, the current, the effective total plating area (i.e., the regions not masked by the insulating material), and the geometry of the plating mask need to be known.

This problem with non-uniformity can be solved by a technique called frame plating. This technique is used by the thin-film magnetic-recording head industry to obtain a uniform and well-defined deposition rate [86]. In frame plating, the electroplating mask only forms an outline around the desired shape of the magnetic material (see Figure 4.10). Since the molding covers a small portion of the entire plating surface (typically less than 1%), the current density is very uniform over the entire plating surface and is easier to calculate. A uniform current density leads to a uniform deposition.

Often the micro-structures of the molding layers are reasonably thick, so that electrodeposited structures of substantial thickness can be formed. The molding material typically used is photoresist[80]-[82], [87] since the thickness can be defined with a precision of up to 200 μm using UV lithography process. In fact, extremely thick photoresist-electroplating molds (>500 μm), with nearly vertical sidewalls, have been

formed using X-ray lithography. The high energy X-rays are typically generated by a synchrotron source; they thus tend to be much more expensive than the optical photolithography process. In the following section, the description of the conventional photolithography with the photoresist molding process that has been developed at Simon Fraser University is given. In Chapter 5, a new technique which uses single crystal molding will be described. This new technique is more suitable for this research.

4•3•2•1 Photoresist Mold

The procedure to prepare the photoresist mold will first be described. For this process, a positive photoresist with high viscosity (Hoechst, AZ4562) has been used. The first step is to subject the wafer to dehydration baking and vapor priming. The dehydration baking is done at 120°C for 15 minutes. Next, the primer is spun onto the wafer at 4000 rpm for 30 seconds. The wafer is then left to vaporize at room temperature for 15 minutes. These two steps are necessary to improve the photoresist adhesion to the seed layer on the wafer. Having done these two steps, a photoresist mold is made from AZ4562, with 3-4 mL of AZ4562 photoresist being poured into the centre of the wafer. The photoresist is then spread to cover a uniform circular region of roughly three inches in diameter, at the centre of the wafer. This step is important to prevent the formation of *fish eyes* in the photoresist. The wafer is then spun at 1750 rpm for 10 seconds. This is a vital step to obtain a uniform thickness of the photoresist. After that, the spin speed is increased to 2500rpm for 60 seconds. During this step, most of the solvent is evaporated and a relatively solid film is formed. Finally, the spin speed is increased to 5000 rpm for 60 seconds. This step is to accelerate the solvent evaporation and does not affect the film thickness; it is also more effective than a hard bake step, because the very thick photoresist

obtained will easily crack when subjected to a hard bake temperature. What is more, a thick photoresist results in a significant edge bead which has to be removed to allow for an intimate contact between the mask and the photoresist. This can be removed by using acetone. Next, the photoresist is patterned using a standard mask aligner and developed using developer solution (Hoeschst, AZ715MIF). After that, the wafer is subjected to soft bake at 100°C for 25 minutes.

4•3•2•2 Seed Layer

In order to electroplate, the electrodeposited material requires a seed layer. This layer acts both as the conductive path from the power supply to the ionic solution and as a nucleation surface for film growth. To avoid significant resistance to the current, there is a minimum film thickness that will depend on the seed-layer conductivity. The resistance of the seed-layer R_s is proportional to its resistance ρ_s, and inversely proportional to its thickness t_s

$$R_f \propto \frac{\rho_s}{t_s} \tag{4.9}$$

Although a common seed layer used for NiFe plating is ~100 nm of sputtered NiFe, the seed-layer material does not have to be the same as the electrodeposited material. If a NiFe seed-layer thickness of 100 nm is desirable then, for the same resistance, a 22nm-thick seed layer of Cu can be used instead (see Table 4.6).

4•3•2•3 Electrolyte

The compositions of the plating baths of NiFe, Ni and Au are given in Tables 4.6-4.8. In the case of NiFe, the recipe was taken from reference [90], whereas in the case of the Ni plating, the recipe was received from our collaborator the Mechanical Engineering

Laboratory in Japan [95].

For Au plating, a commercial plating bath was purchased. In the first Ni or NiFe plating baths, saccharin was omitted because of its unclear nature. After several attempts that resulted in highly stressed films which peeled away from the substrate, saccharin was used to lower the stress of the electrodeposited Ni or NiFe [96].

Material	Resistivity [Ω-m]	Seed layer Thickness [nm]
Ni	6.84×10^{-8}	~85
Fe	9.71×10^{-8}	~120
NiFe	7.41×10^{-8}	~100
Cu	1.67×10^{-8}	~20

Table 4.6 Electroplating seed layer material, resistivity and typical thickness [86].

Material	Chemical Formula	Quantity [g/L]
Nickel Sulfate	$NiSO_4$	330
Nickel Chloride	$NiCl_2$	30
Boric Acid	H_3BO_3	30
Sodium Sulfate	Ne_2SO_4	0.5
Saccharin	$C_7H_4NO_3C_2$	1.0

Table 4.7 : Electroplating bath solution for Ni alloy at 50°C [95].

Material	Chemical Formula	Quantity [g/L]
Nickel Sulfate	$NiSO_4$	212
Nickel Chloride	$NiCl_2$	18
Ferrous Sulfate	$FeSO_4$	22
Ferrous Chloride	$FeCl_3$	2.5
Boric Acid	H_3BO_3	25
Sodium Sulfate	Na_2SO_4	180
Saccharin	$C_7H_4NO_3C_2$	1.0

Table 4.8 : Electroplating bath solution for Ni-Fe alloy at 50°C [90].

4•4 Counter Electrode Epoxy Bonding

This is an optional step and serves two purposes. Firstly, it is used to seal the cavity that contains the micromachined tips to the top plate. And secondly, it provides the mechanical support for the second or the third electrode to be positioned above the tips. There are two methods to accomplish this. The first method of fabricating an electrode, at a precise distance from the tip, is to pattern metal onto a glass substrate and anodically bond the substrate on the cavity where the tips will be [24], [84]. In this case the glass is usually made out of a borosilicate glass and will have two holes to provide the input and the exhaust manifolds. Since the electrodes can be positioned very close to the tips, it is imperative that this seal be accomplished without introducing any foreign materials into the cavity (i.e., an epoxy or other adhesives). However, the main disadvantage of this technique is due to the thermal constraints imposed by certain conductive material of the tip. Therefore, it is necessary to perform the operation at a lower temperature; i.e., 150°C using a borosilicate glass substrate. Reston [24] has reported that it is possible to perform a similar operation at a lower temperature but the operation time is long (20 hours) at

1800V (as opposed to 15 minutes at 1000 V at 450°C). This temperature can be even high enough to deform tips made out of gold.

The alternative approach to the glass anodic bonding process is to use a thick electroplated gold plate to provide the counter electrode and the input and the exhaust manifold. The electroplated gold plate can be simply connected to the chip with epoxy to seal the cavity. This method has the risk of contaminating the cavity with epoxy and therefore has to be done with a high viscous epoxy to reduce this risk.

4•5 Summary

This chapter discussed the theory concerning the basic and important tools and techniques used or necessary to manufacture the micromachined field ionization tips in the same sequence as it was actually fabricated. Anisotropic wet chemical etching is firstly used to micromachine the silicon surface creating the pits for the detector structure. Thick film deposition by electroplating is then employed to realize the cathode structure. Finally, an anode electrode was patterned on a glass substrate and can be anodically bonded to the micromachined tip to assemble the micromachined field ionization detector. The next chapter will discuss in greater detail the microfabrication steps and design.

Chapter 5

Design and Fabrication of Micromachined Field Ionization Tips

In this chapter, the low-cost techniques used to micromachine the field ionization tip is described in detail. The primary microfabrication tools used for fabricating the field ionization tip are those described in Chapter 4 namely, the standard oxidation process, a standard wet anisotropic chemical etching, a generic electroplating process without photoresist mold (for thick film deposition), a standard sputtering process and finally counter electrode bonding for sealing a top lid with input and exhaust manifolds. It is also the intention of this research to demonstrate that a mask with a millimeter resolution can be used to achieve a sub-micrometer gap between the tip and the counter electrode. In the following sections, these processes are discussed relative to their ultimate goal, which is to micromachine a field ionization gas detector.

5•1 The Commonly Used Fabrication Processes

As discussed in Chapter 3, the significance of having a high electric field is to initiate the field ionization process in a sample gas. At the same time, it is pointed out that a simple parallel electrode structure, is simply not a practical approach to accomplish the field ionization process. Thus, it is argued that the essential arrangement is to have an electrode with sharp tips opposite a flat counter electrode. In this respect, the fabrication processes that are most commonly used to microfabricate a sharp tip are reevaluated with

respect to their cost effectiveness. Most of the fabrication processes evaluated here are those used to manufacture sharp tips in field emission devices. Since the field emission is the reverse process of the field ionization, these tips can also be used for the field ionization process.

Inherently, the field ionization tip has to be very sharp (typically in the range of 100nm in radius) to be able to generate a high electric field at a strength of 10^7-10^8 V/cm, preferably with a small applied voltage for hand-held applications. The sharp tips, when biased to a positive potential with respect to a counter electrode, create a large electric field at the structures' apex. Two of the governing parameters which are generally used to produce the high electric field are: (a) the sharpness of the tip; and (b) the gap between the tip and the counter electrode. The latter one is equally important. Since this particular gap is restricted by the limit of the lithography process used, then a very high resolution process has to be essentially utilized to achieve the needed sub-micrometer gap. Some of the processes that can be used to achieve this small gap include the use of masks with sub-micrometer resolution, the electron beam lithography process or even X-ray lithography. All these processes result in a considerable increase in the manufacturing costs which opposes one of our main objectives. While this counter electrode can be a physically separate structure, the minimum gap can most conveniently be obtained by physically positioning the counter electrode with respect to the tips in a self-aligned process for much improved fabrication yield and cost.

The fabrication of the sharp tips which are applicable to field emission devices can broadly be classified into five major groups, which are described here. The first category is

one of the earliest inventions in which the tip structure is formed by a direct deposition of the metal material. The conventional fabrication method for this type of self-aligned tip has been described by Spindt *et al.* [98] and is shown in Figure 5.1(a)-(d) [98], [99].

The process begins with the deposition of insulation and a metallic layer utilized for the counter electrode on a conductive substrate respectively. Most often this conductive substrate is silicon, but glass or other isulative substrate with a conductive layer on the top have also been tried [100]. A small round hole is then formed in the metallic layer and the insulation layer underneath, by using the conventional photolithographic process (see Figure 5.1(a)). Next, a sacrificial layer made out of a material such as alumina, is vacuum deposited on the substrate at a shallow angle to the counter electrode (see Figure 5.1(b)). Also this results in a reduction of the diameter of gate aperture substantially. The metal layer made out of a material such as molybdenum, is then deposited perpendicularly to the substrate (see Figure 5.1(c)). The gate-aperture diameter is gradually reduced as the metal

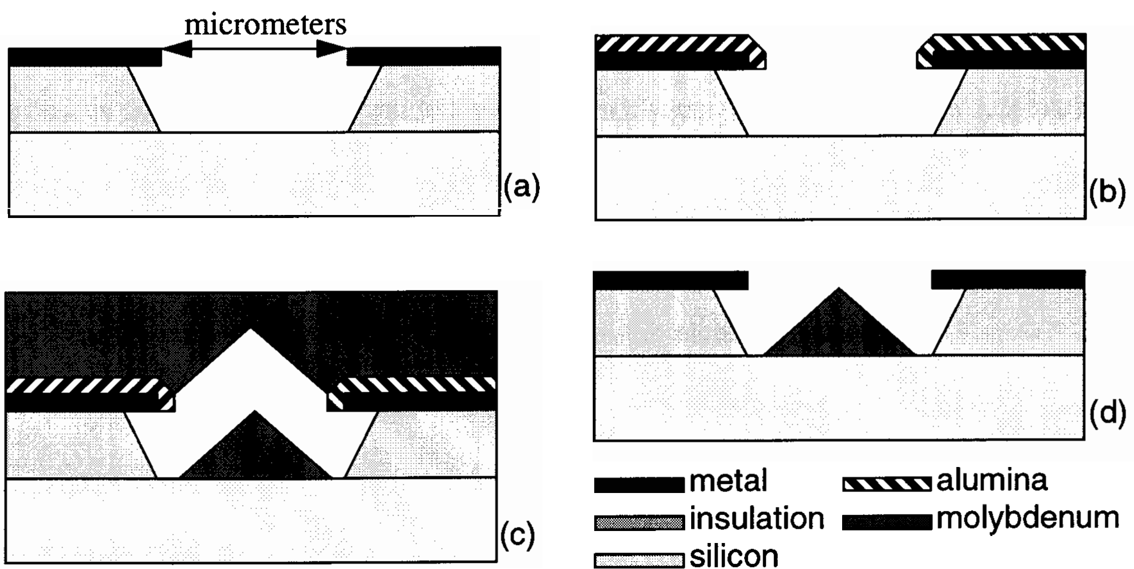

Figure 5.1 The cross-sectional views of the fabrication sequence of the self-aligned tip formation process by Spindt *et al.* [98].

layer is vacuum deposited, and a cone-shaped tip is formed within the aperture since the counter electrode's aperture becomes smaller as the deposition proceeds. Lastly, the fabrication process is completed by removing the sacrificial layer and the unnecessary metal layer using an etching or lift-off method (see Figure 5.1(d)).

The required tools for fabricating this category of tips are a low-pressure chemical vapor deposition system (LPCVD) or plasma enhanced chemical vapor deposition system (PECVD) for deposition of insulation, an electron beam evaporator with a rotating source and substrate, with a steep angle deposition process. Since the tips are formed by metal deposition, through micrometer or sub-micrometers-sized apertures that are defined lithographically, precise control of the tip radii and height of the tips are hard to achieve.

The second category of the tip's formation uses an anisotropic etching of a single crystal material such as silicon (see, for example [101]). The fabrication process sequence is shown in Figure 5.2(a)-(e). The fabrication process begins with the deposition of a silicon oxide film on a silicon substrate (see Figure 5.2(a)). Then, the photolithographic process is used to pattern the oxide layer to form a square mask (see Figure 5.2(b)). Next, the silicon substrate is subjected to an anisotropic etching process to form a pyramid with a sharp tip under the oxide mask (see Figure 5.2(c)). Next, an insulating layer and a metal layer, for the counter electrode, are deposited on the etched substrate (see Figure 5.2(d)). The patterned masking layer prevents the deposited layers going underneath the masking material. Lastly, the mask and the insulating and metal layers thereon, are removed, resulting in a tip self-aligned to the counter electrode (see Figure 5.2(e)).

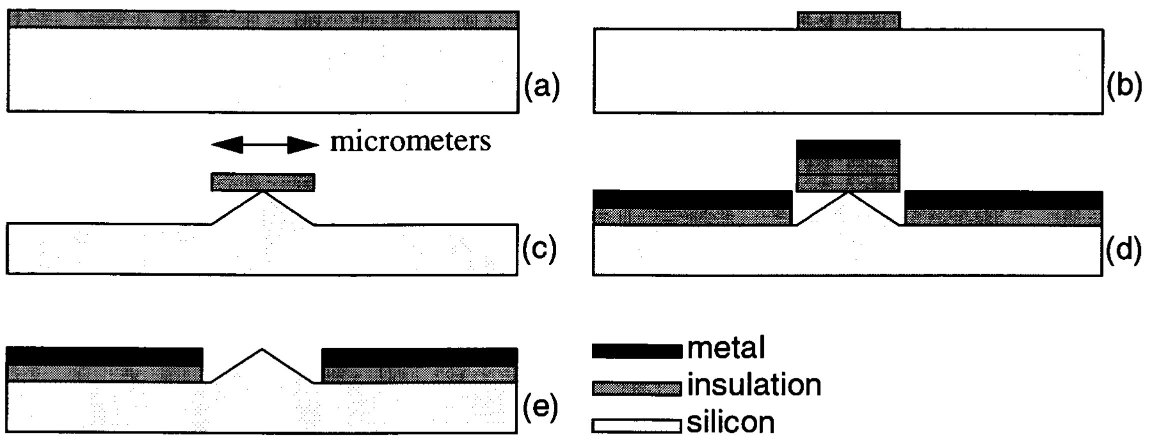

Figure 5.2 The cross-sectional views of a field ionization tip structure fabricated by the photolithographic process described in [101].

In addition to fabrication tools such an electron beam evaporator, a CVD for the deposition of insulation, and a RIE for etching or stripping silicon nitride, there is a need to have lithography masks with a micrometer or sub-micrometers resolution to create a square island. However, this method has the disadvantage that the tips are not very sharp. This is usually due to fact that the etch process is stopped right before the {111} planes meet under the square mask to avoid the collapse of mask over the tip.

The third category of tip formation process uses an isotropic etching method to form the sharp structures (see, for example, [102]). Its fabrication sequence is shown in Figure 5.3(a)-(e). The process starts by forming a silicon oxide film on a silicon substrate (see Figure 5.3(a)). Next, the photolithographic process is applied to the silicon oxide to form a square mask (see Figure 5.3(b)). Next, the patterned substrate is subjected to wet isotropic etching to form a protrusion of a tip under the mask (see Figure 5.3(c)). Next, an insulating film and a metal film, to be used as the counter, are deposited (see Figure

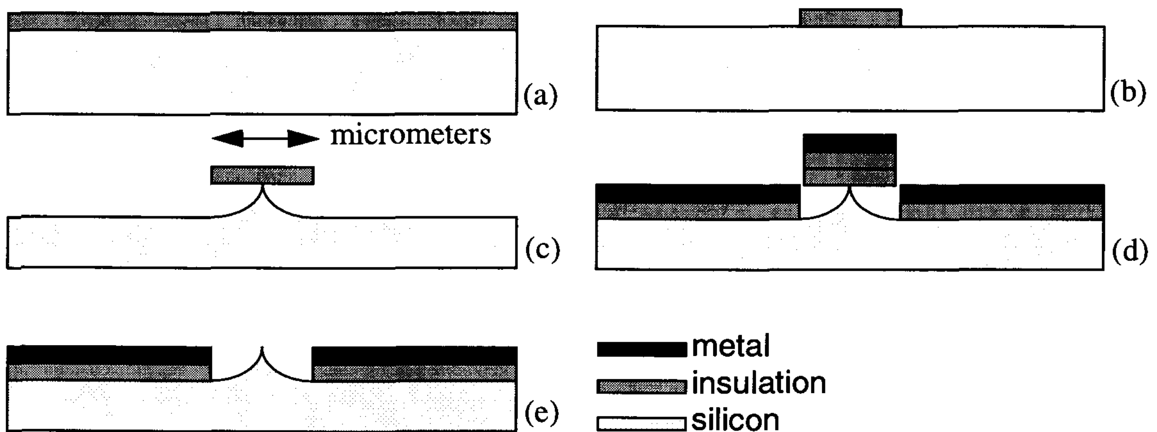

Figure 5.3 The sectional views of a field ionization tip structure fabricated according to an anisotropic process [102].

5.3(d)). Lastly, the mask and the insulating and metal films thereon are removed, resulting in a tip with a sharp apex (see Figure 5.3(e)).

Again, like the second category of tips, this process also requires similar non-standard tools to fabricate tips as well as a high resolution mask to create the circular pattern on the oxide layer of the silicon substrate. Tips fabricated in this way also lack sharpness.

The fourth category uses oxidation processes, which sharpen a tip by oxidizing the isotropically etched tip [103]. Oxidation profiles under oxide masks are virtually identical to isotropic etch profiles in isotropic tip formation; they sharpen the tip structure when the profiles converge under a circular mask (see Figure 5.4(a)-(e)). When the oxidized material is removed, the unoxidized tip can function as a field ionization electrode. The process in this category is very similar to that of the isotropic etch category but with much improvement in the sharpness. And, in the same way, the counter electrode is self-aligned

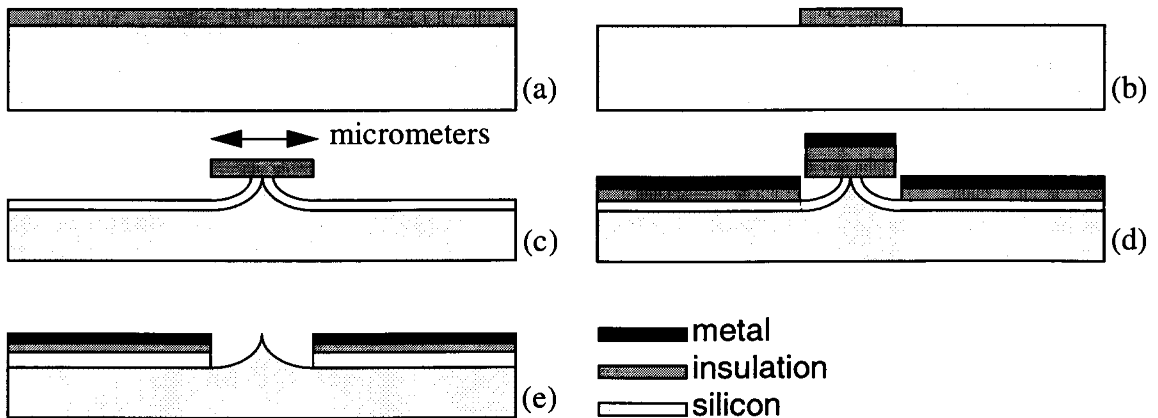

Figure 5.4 The sectional views of field ionization tip structure fabricated according to an isotropic process [103].

to the tip. Other masking materials such as silicon nitride can also be used similarly to retard the oxidation and produce the desired sharp tip profile.

The disadvantage with this process is also the use of non-standard tools for manufacturing tips and the use of the high resolution masks to pattern the oxide layer on the silicon substrate.

The fifth category in its simplest form, starts with a deposition of a metal layer on silicon substrate (see Figure 5.5(a)) [104] and [105]. Then, a hole is formed by the RIE process to form vertical walls in the hole as shown in Figure 5.5(b). Next, a layer of a second material, usually oxide, is conformally deposited on the surface of the etched substrate, until the growing thickness on the sidewalls of the hole converges in the centre of the hole to form the cusp (Figure 5.5(b)). A conductive layer is then deposited to fill the cusp (see Figure 5.5(c)). The substrate is then selectively etched away from the tip (see Figure 5.5(d)). Finally, etching away the oxide cusp completes the process (see Figure 5.5(e)).

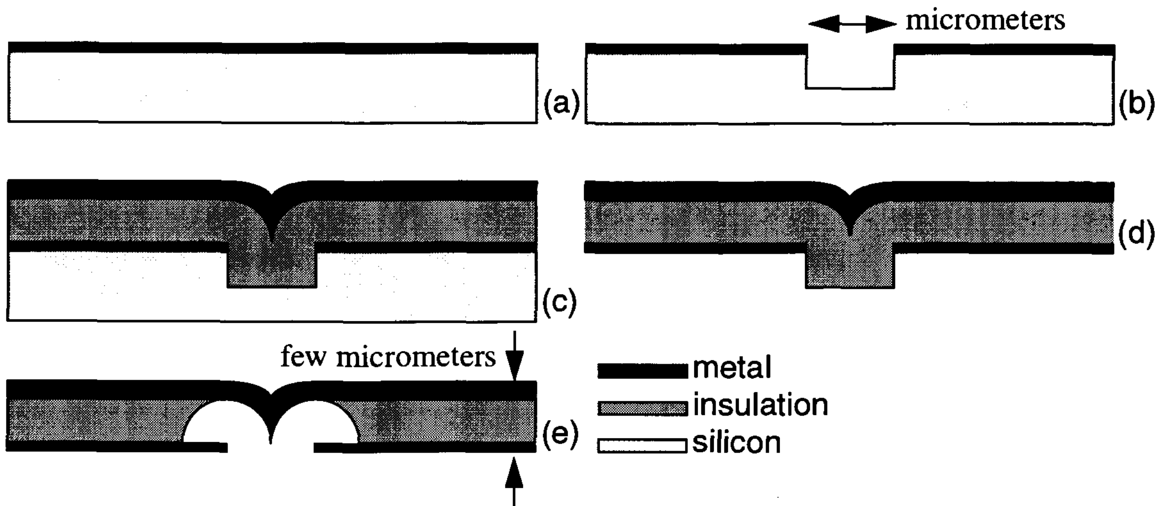

Figure 5.5 The sectional views of a field ionization tip structure fabricated according to a conventional photolithographic process described in [104].

This process is done with the use of non-standard tools and a high resolution mask to pattern the oxide layer on the silicon substrate. Although this process results in sharp tips with a self-aligned counter electrode, it lacks practicality as far as a gas detector is concerned. This is because the insulation layer shown in the Figure 5.5 is quit thin (not more than 1-2μm in thickness) which causes problems with handling.

All of the tip formation techniques reviewed in this section have several limitations. Firstly, they all require equipment which are not accessible to small laboratories due to their high cost and size. Secondly, to pattern the masking layer, they need to have masks with a micrometer or sub-micrometer resolution to position the tip as close to a counter electrode as possible.

In addition, it is important for the fabrication method to be flexible, in order to position the tip at a precise position with respect to the counter electrode as discussed in [106]. And it must allow the tip to be very sharp which is one of the requirements for field ionization [107].

5•2 Micromachined Tip's Fabrication Process

In this section, the fabrication process for an micromachined tip is going to be described in more detail. The fabrication of a micromachined tip was accomplished through several phases. In the first phase, a photolithography mask set was designed and manufactured in our laboratory. In the second phase, the microfabrication and micromachining steps were applied to physically create the required features in the silicon wafer. It also consisted of microfabrication steps to deposit metallic layers (by electrodeposition or sputtering) for the anode electrode. The last phase involved attaching the interconnecting tubing and the counter electrode by glue bonding. These phases will be expanded upon in the following sections in the order in which they were applied.

5•2•1 Mask Design and Preparation

All of the masks used in the photolithography process steps were made using in-house facilities in the School of Engineering Science[1] using the Cadence[2] software package and photographic glass plate with emulsion on one side. The total number of photolithography masks needed for manufacturing of micromachined field ionization detector are three plates, each corresponding to a specific fabrication process step. All three photolithographic masks were realized by implementing similar techniques for their layout and preparation. In order to generate the photolithographic mask layouts, a layout-generating program such as Cadence was used to place the required photolithographic mask features (i.e., squares and rectangles) in precise relative locations, ensuring that

---

1. School of Engineering Science, Simon Fraser University, Burnaby, BC, V5A 1S6, Canada.
2. Cadence Design Systems, Inc., 555 River Oaks Parkway, San Jose, CA 95134, USA.

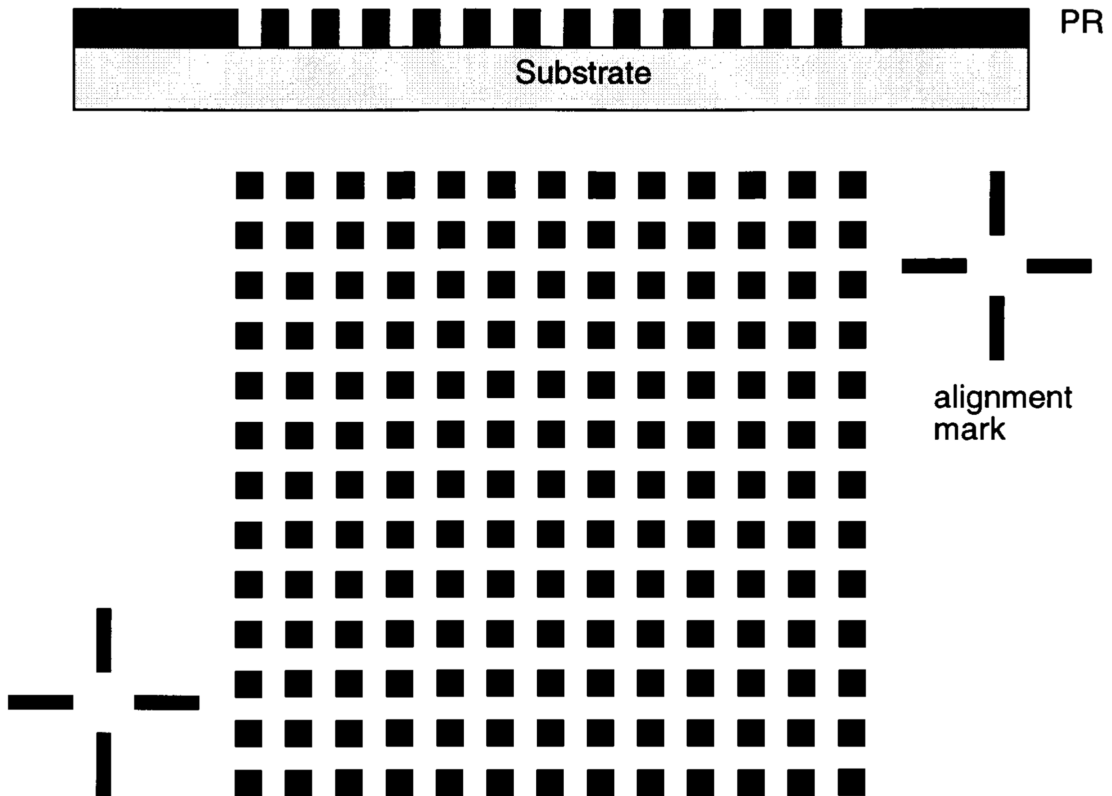

Figure 5.6 Photolithographic mask design used for the first EDP etch to create pits on the bottom surface of the silicon wafer.

various layers (corresponding to the different fabrication processes) are in position with the proper alignment marks. The PostScript version of each layer (1:1 times magnification) is generated and submitted to a local desktop publishing company, WYSIWYG[3]. At WYSIWYG, the layouts were then transferred onto transparencies and sent back to us for subsequent generating of the photographic glass plates.

The first photolithographic mask plate (used for the first EDP anisotropic etch on the back of the wafer) is shown in Figure 5.6. It consists of an array of small squares. The

3. WYSIWYG, 400 West Georgia Street, Vancouver, BC, V6B 1Z3, Canada.

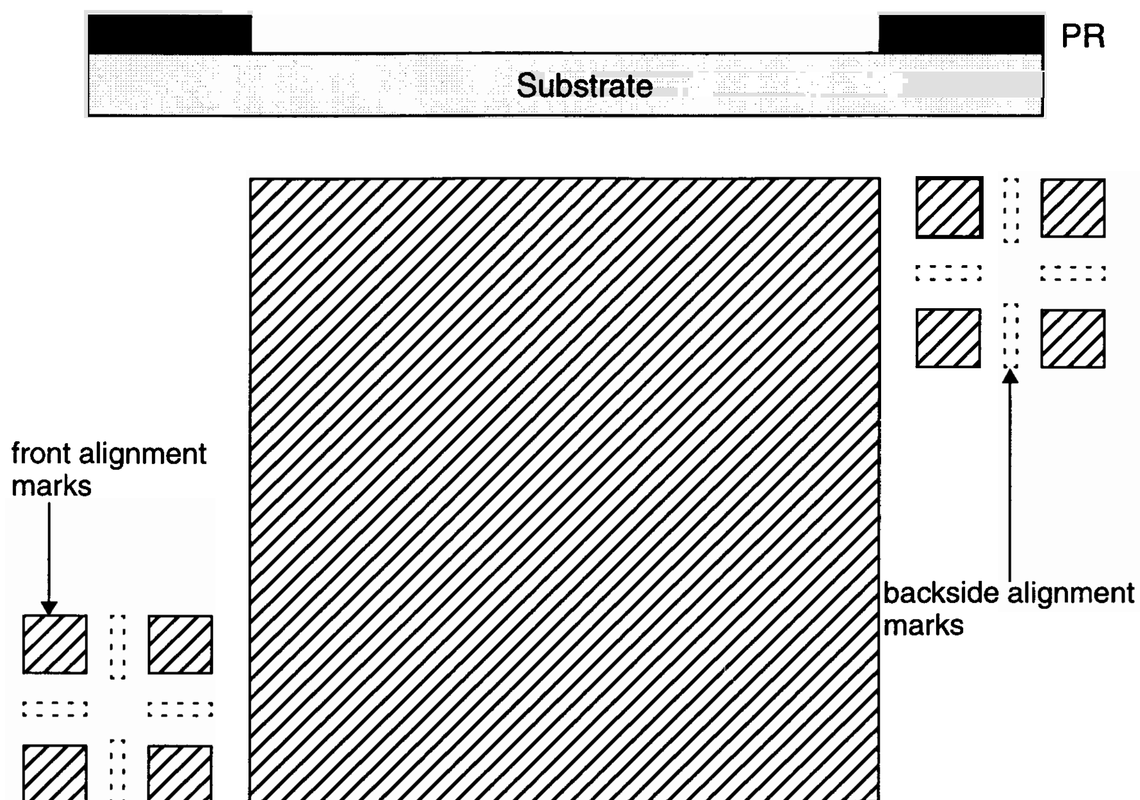

Figure 5.7 Photolithographic mask design used for the second EDP etch from the top surface of the silicon wafer.

dimension of each square is 500 x 500 μm with a 100 μm gap between them. The array consists of 13 by 13 squares. The minimum dimension that can be achieved is about 50μm by using the facility available at the local desktop publishing company.

The second photolithographic mask plate is used for the second EDP anisotropic etch on the front side of the silicon wafer (shown in Figure 5.7). It consists of one large square with the dimension of 1 cm x 1 cm. The purpose of this mask is to pattern and remove the silicon from the top surface to release the field ionization tips. This is discussed in the next section in more detail. In addition, there are narrow lines on this mask with a width of 300 μm, along the horizontal and vertical lines to partition the

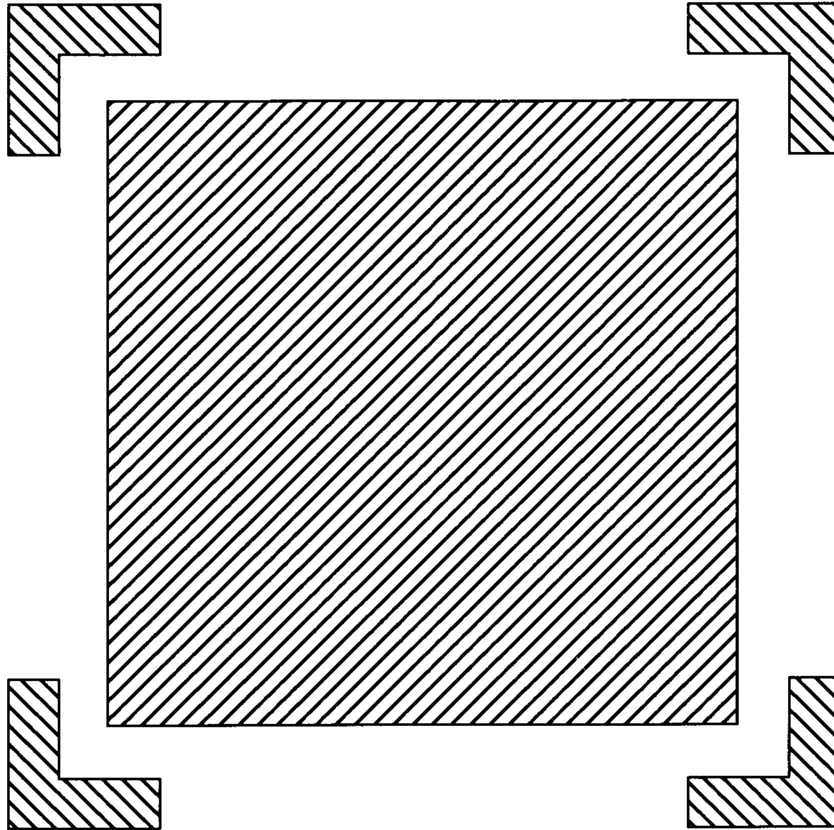

Figure 5.8 Photolithographic mask design used for patterning the metal plate on the top surface of the glass wafer.

detectors into chips for easy cleaving. The third photolithographic mask plate is used for patterning the metal on a glass wafer for a second or third metal (shown in Figure 5.8). This step is optional (as was mentioned in the previous chapter), as it can be replaced by a simple gold plate lid epoxy bonding to the silicon chip.

5•2•2 Design and Fabrication Phase

The following fabrication sequences and their related diagrams are intended to illustrate the formation of individual tip structures. While not specifically shown, multiple tip structures in any spatial pattern can be simultaneously fabricated. The fabrication is based on the US patent pending application [108].

The starting point in this process is a single-crystal silicon wafer with {100} crystal orientation. It may be of any convenient diameter and thick enough to be handled easily. The wafer is then subjected to an oxidation process to grow an oxide layer (for the masking layer) on both sides of the wafer (see Figure 5.9). While the masking layer may be a variety of materials, due to the need for a low-cost approach, silicon dioxide has been

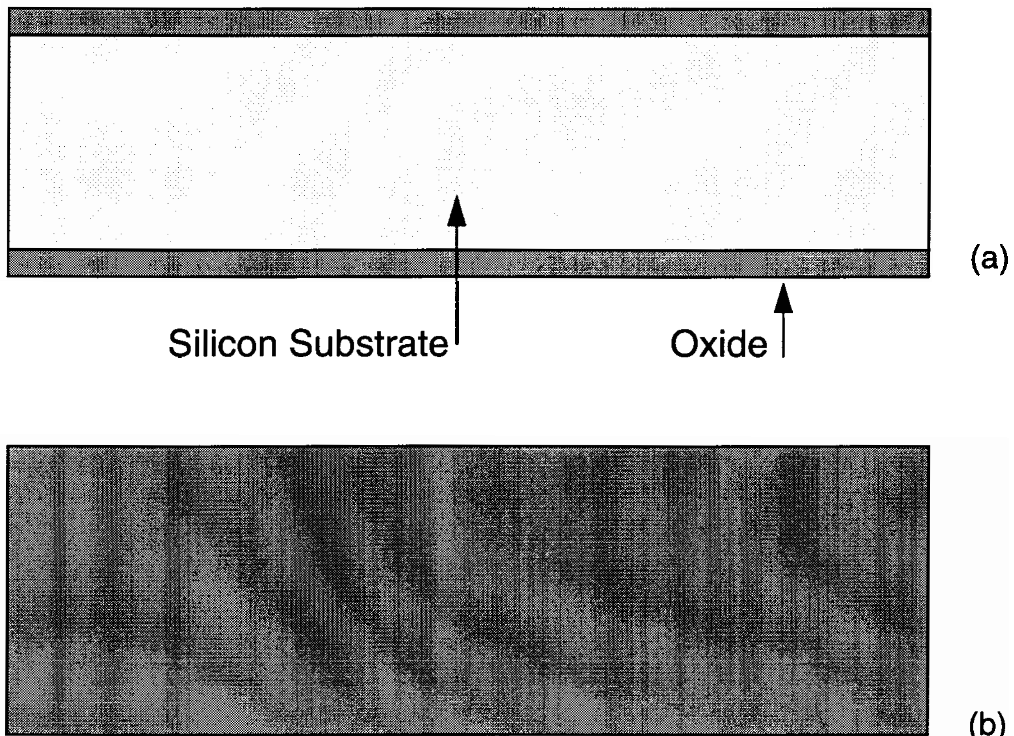

Figure 5.9 The cross-sectional (a) and the top view (b) of an oxidized wafer.

chosen as the preferred technique. It starts by cleaning the wafer in accordance with known standard techniques, such as the RCA cleaning process (see Appendix A). The surfaces are then subjected to oxidation to produce a thin (0.5 μm) masking layer, the silicon dioxide obtained by the wet thermal oxidation method shown in Figure 5.9. Next, the oxidized wafer is subjected to a photolithography process (using the mask shown in Figure 5.6) to create a photoresistive mask having at least a one square opening. This opening is located at the points on the surface of the wafer where it is desired to form the field ionization tip. Next, the portion of the masking layer, not protected by the photoresist layer, is etched away by a buffered-oxide-etch (B.O.E.[4]) solution, to open a window in the

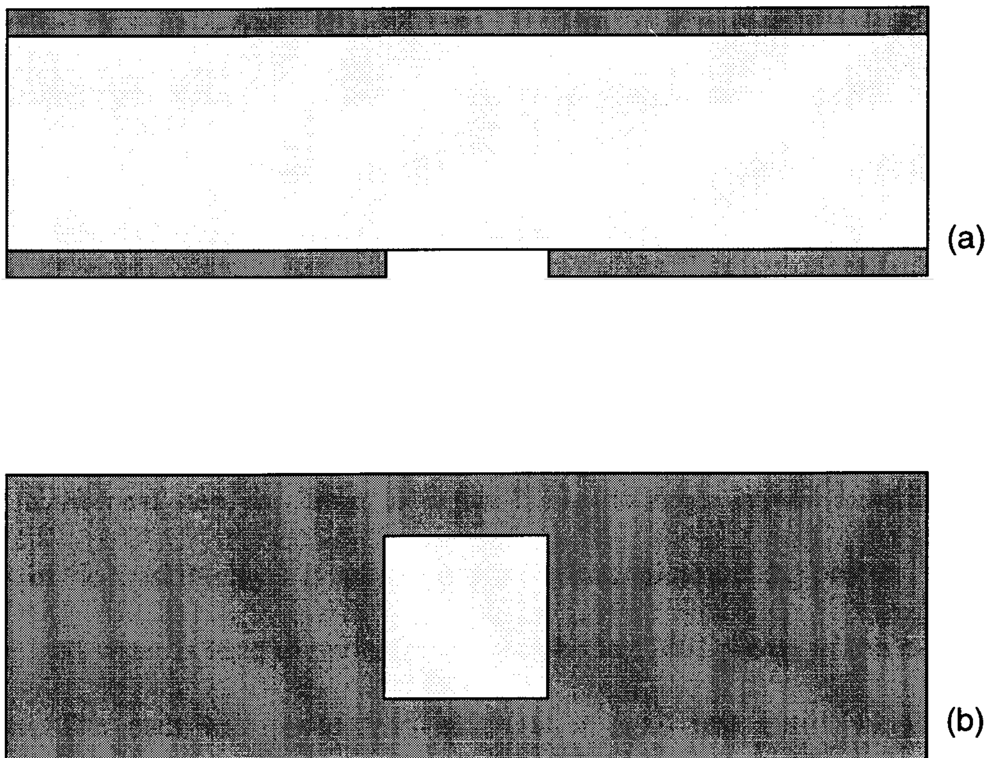

Figure 5.10 The cross-sectional (a) and the top view (b) of a single crystal substrate having the patterned silicon dioxide on one side of the wafer.

4. Transene Company Inc.

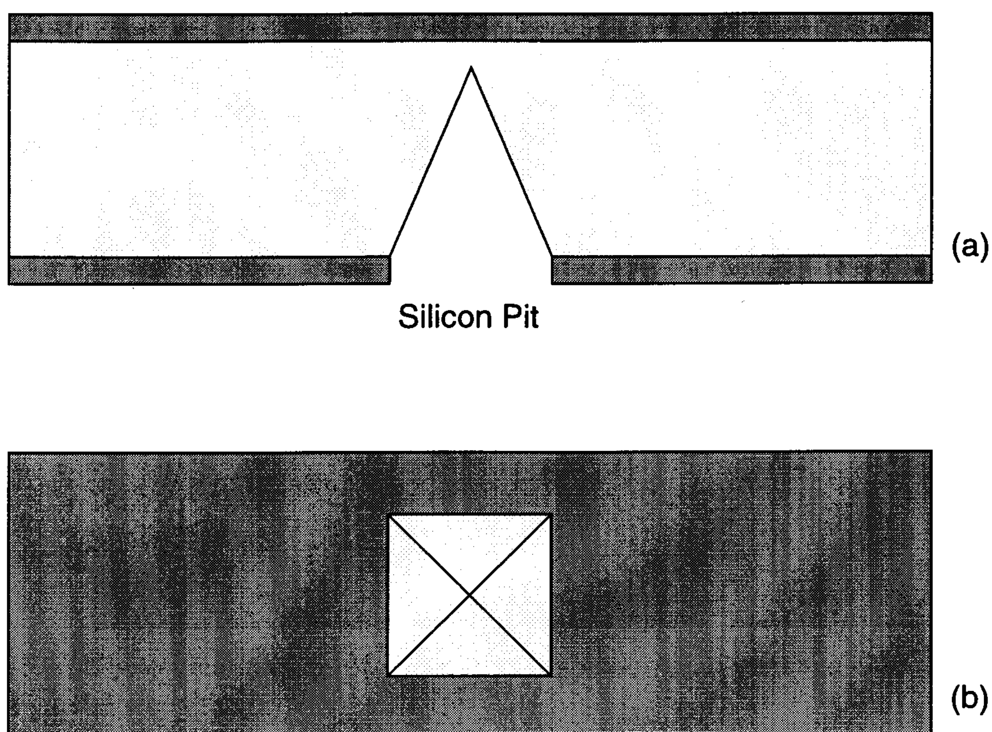

Figure 5.11 The cross-sectional (a) and the top view (b) of the etched pit in the substrate.

oxide layer. The time taken to etch the oxide layer for this case is about five minutes. The patterned oxide layer can then be used as a mask for the subsequent etching of the silicon substrate. The patterned photoresist is now removed by acetone (see Figure 5.10).

In the next step, as shown in Figure 5.11, the single crystal material under the window in the masking layer is subjected to an anisotropical etching process. In this step, the EDP and water is used to preferentially attack the {100} planes of the n-type silicon substrate. The etch will proceed to attack at a rapid rate until {111} planes are encountered; the etch then stops or is significantly slowed down. The total time taken to etch a pit like that is about five hours. This action tends to produce an inverted pyramidal

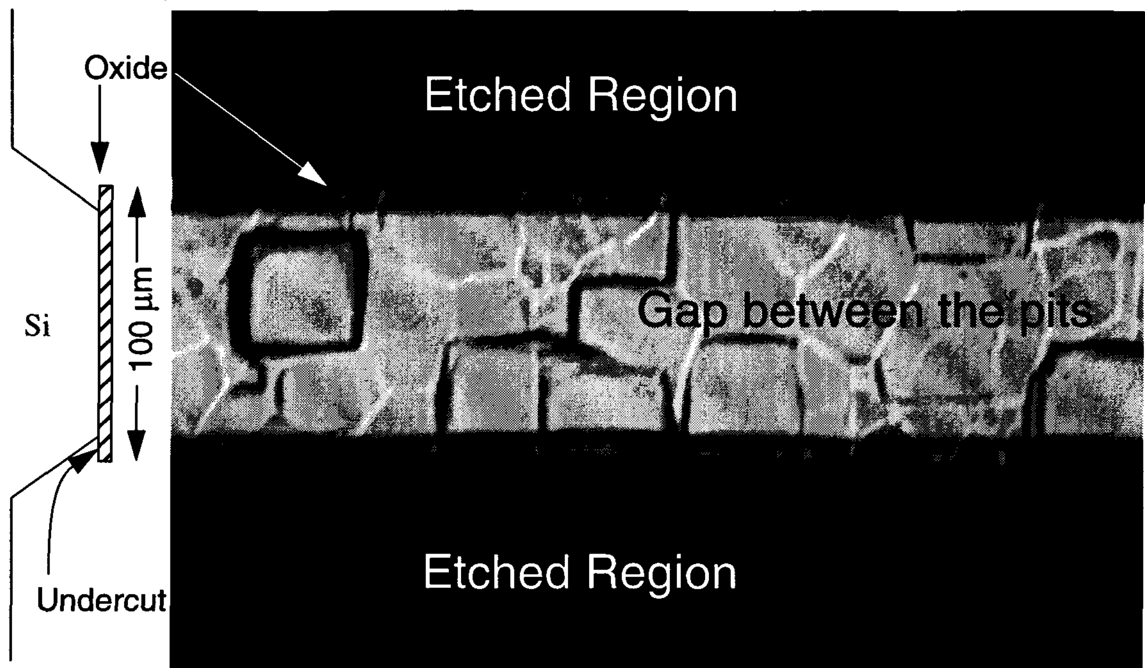

Figure 5.12 The optical picture of part of a two anisotropically etched silicon pits with a 100 µm gap between them.

pit whose {111} sides intersect at a crystallagraphically sharp point. Further etching only makes a given hole wider rather than deeper; but the sharpness of the {111} plane intersections is not changed. The average depth of the holes can be determined by the size of the masking dots initially used, the relative etch rates of the {100} versus {111} plane and the length of time of the etching process (see Section 4•2•1). Figure 5.12 illustrates the optical picture of the situation where the silicon is etched. As can be seen from this picture the gap between the pits is fairly important and if the etch process is maintained for a long time, the etched region may merged into each other. The patterns seen on the surface of the silicon wafer are due to roughness of the backside of the wafer. Following this step, the oxide layers on both sides of the wafer are etched away by a B.O.E. solution leaving only the pit structure.

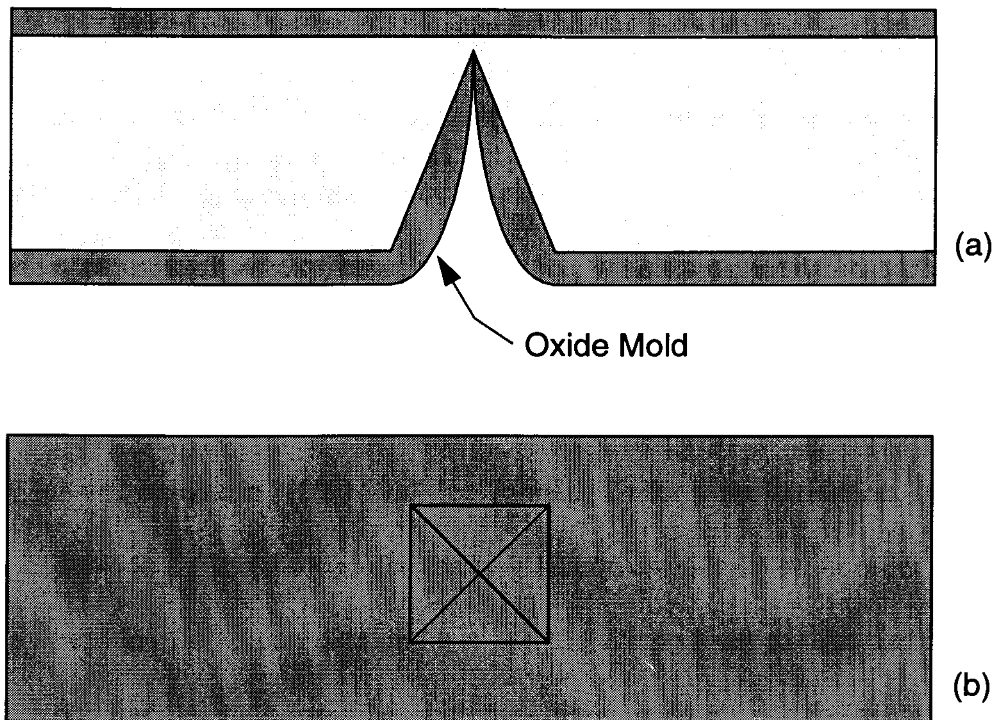

Figure 5.13 The cross-sectional (a) and the top view (b) of the oxidized pit in the substrate.

Figure 5.17 shows the SEM picture of a tip fabricated by filling the mold shown in Figure 5.11 with electroplated gold. Then the electroplated gold layer was peeled off the substrate to demonstrate its sharp structure. The peeling-off process was performed by a piece of sticky tape. In this case, nickel was used as the electroplating seed layer. The traces of what that are visible on the structure are the nickel seed-layer residual. This figure illustrates the sharpness and the smoothness of the tip structure. Also a tip fabricated even with this simple silicon mold method is as sharp as the tips fabricated with the anisotropic method shown in Figure 5.2 [89].

The next step, as shown in Figure 5.13, is achieved by subjecting the wafer to a wet thermal oxidation process to grow an oxide layer in the pit. The mechanisms with which the oxide is grown in the pit is not much different from the oxidation step in the previous step. In this step, the oxide formation in the pit is also established by the molecules of the oxidizing species, such as oxygen or water vapor, which must arrive in contact with the silicon molecule on the silicon surface. The mechanism becomes diffusion-controlled after a thin layer of oxide (usually a thickness of greater than 40 Å for dry oxidation, and 1000 Å for wet oxidation [109]) has been formed. Under these oxidation, the oxidizing molecules have to diffuse through the existing silicon dioxide layer, in order to reach the boundary between the silicon dioxide layer and the silicon itself to take part in a reaction where the oxygen molecule combines with the silicon molecule. As the oxidation reaction progresses, the silicon dioxide layer becomes so thick that virtually no new silicon dioxide forms, even at elevated temperatures or over extended periods of time. Thus, growth proceeds at an ever-decreasing rate as the thickness of intervening oxide layer increases.

Although this mechanism is well understood for surfaces of a {100}-oriented silicon wafer, but not other surfaces. However, Marcus *et al.* [110] have studied the formation of oxide by wet oxidation on {111}, {110} and {100} surfaces, at temperatures of 900°, 950°, 1050° and 1100° C to make a recommendation for an optimum oxidation temperature for formation of stress-free oxide on IC microelectronics chip. The parameters which they studied were the growth rate, temperature and crystal orientation, on formation of oxide on silicon. Their main conclusions from research were, that silicon dioxide formed on silicon at low temperatures between 900°-950°C, has a higher

compressive stress in the oxide on the sharp corner surfaces than on flat surfaces. They believe that the higher compressive stress within the oxide has a depressing effect on diffusibility of the oxidizing species into the silicon, resulting in a reduced oxidation rate and, therefore, a decreased oxide thickness on the corner surface as compared to a flat surface. At higher temperatures, the effect of stress on oxidation kinetics becomes less, and this results in a uniform growth rate [110]. The optical picture shown in Figure 5.18 illustrates a series of pits etched in the silicon wafer. The white dotted line shows the contour of the cross-section of the wafer.

The next step is shown in Figure 5.14. This step consists of opening a larger window in the oxide layer on the top side of the wafer where the surface of the wafer was

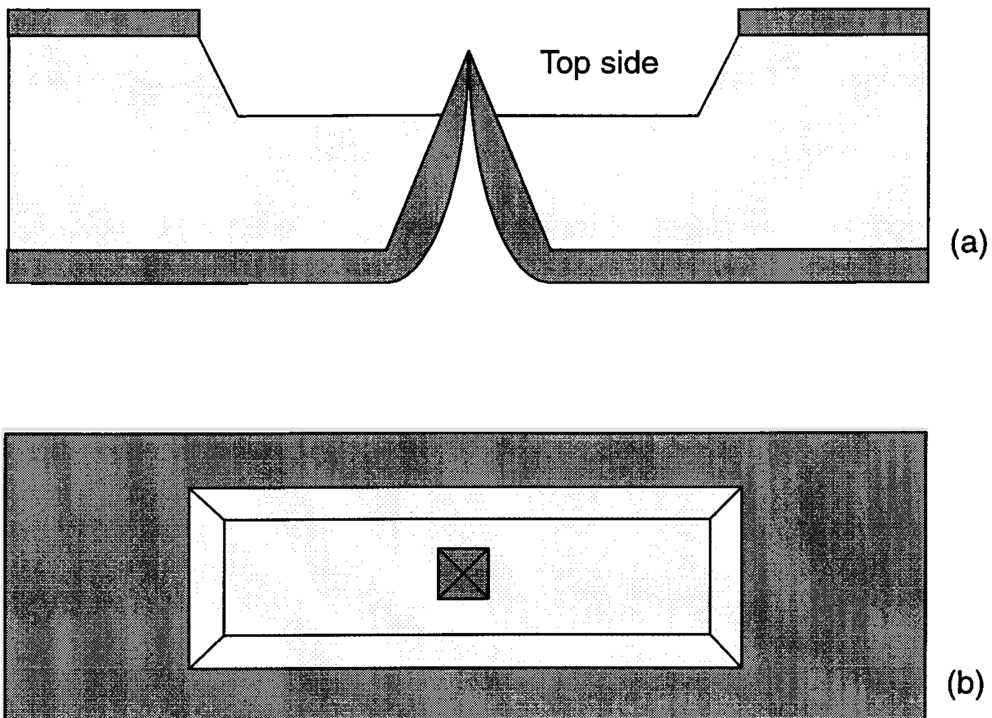

Figure 5.14 The cross-sectional (a) and the top view (b) of the case after the top part of the silicon substrate etched to release the oxide mold.

not etched in the previous anisotropic etching. Having opened the window in the oxide layer, the exposed single-crystal silicon was etched away EDP for 3 hours and 15 minutes. The etching time depends on the size of the pit etched, and can be estimated from the tables given in Chapter 4. The process is stopped as soon as the tip of the oxide mold becomes visible from the top (shown in Figure 5.14). Figure 5.19 shows the cross-sectional view of the wafer just before the tip of the mold becomes visible from the top. At this point the etching process proceeds at an ever-decreasing rate to allow the measurements to be taken under a microscope. This is done under an optical microscope with an electronic measuring gauge to measure the size of oxide mold while an light source is used to illuminate the wafer from beneath.

As discussed earlier, one of the purposes of the low temperature oxidation is to introduce a compressive stress to create curvature inside the mold for sharpening the tip. The other purpose of the oxide layer is to define the distance between the tip and the counter electrode. This gap is then essentially controlled by the oxide thickness, which, in turn, is controlled by the oxidation time. The SEM pictures shown in Figures 5.21 and 5.23 are the tip of the oxide mold. Figure 5.22 illustrates the position of the tip with respect to the counter electrodes.

In this step, first a thin layer of nickel is sputtered into the oxide mold shown in Figure 5.15. This layer, as was discussed in the previous chapter, is the seed layer for the subsequent electroplating process. The choice of metal for the seed layer is based on its resilience to a subsequent B.O.E. etching. Having sputtered the seed layer into the oxide mold, then a thick layer of a conductive material, such as gold, is electroplated onto the intermediate structure shown in Figure 5.15. Gold is an appropriate choice for the tip material as it is capable of initiating ionization under the influence of an electric field without allowing any reaction with the sample gases. The electroplated layer fills the hole and can extend over the pit if the depth is smaller than the thickness of the deposited material. In this case, it is possible to have a solid structure as opposed to a hollow one.

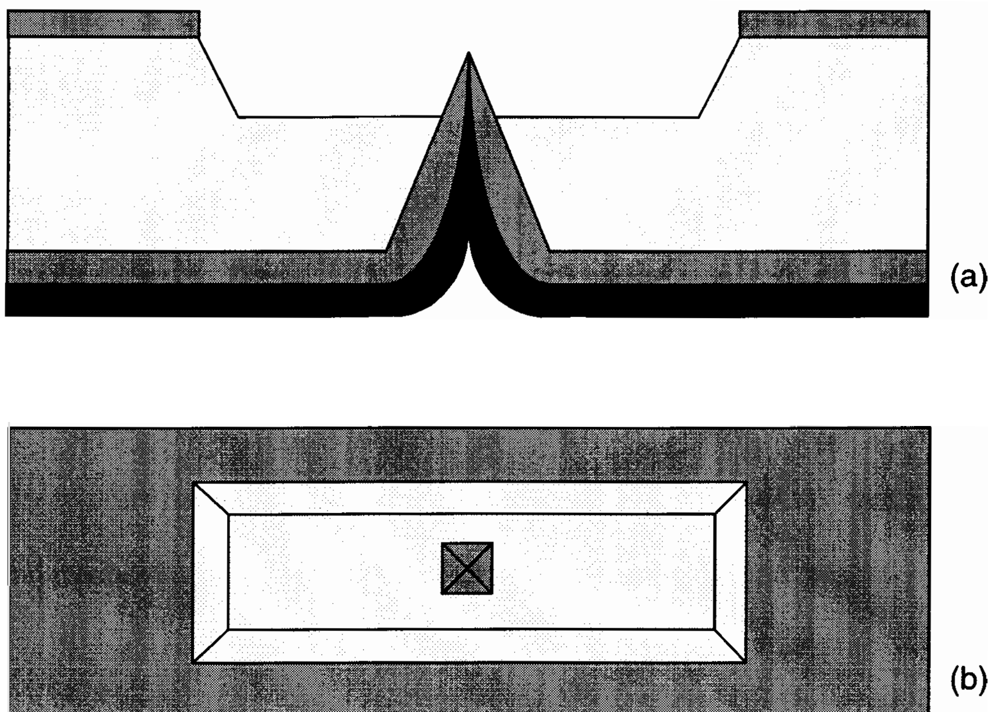

Figure 5.15 The cross-sectional view of the electroplated gold into the silicon dioxide mold.

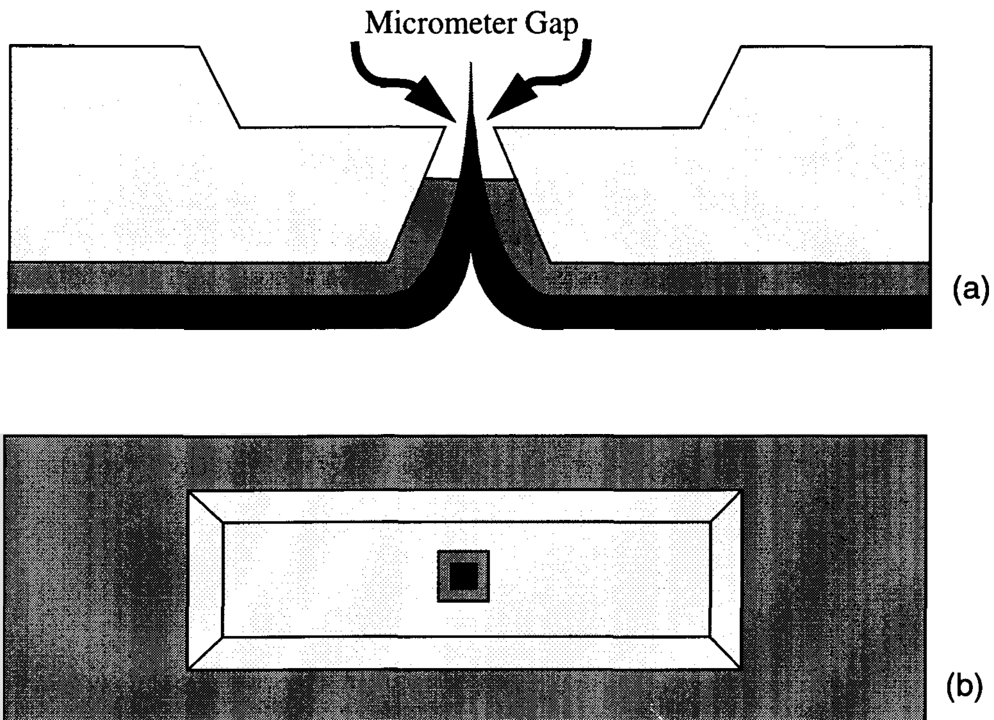

Figure 5.16 The cross-sectional (a) and top (b) view of the released tip.

The thickness of the deposited gold layer measured by a profilometer is approximately 40μm. Figure 5.17 shows one such tip that was created by electroplating gold into the silicon mold shown in Figure 5.15. The final processing step is to etch away the oxide mold from the top, using a suitable chemical etchant such as B.O.E.. Since the cavity where the tips are going to be is 1 cm by 1 cm, then a few drops of B.O.E. were placed in the cavity to observe the process under a microscope. Once the B.O.E. etches through the oxide and reaches the seed layer, bubbles starts to appear on the surface of the etchant. The etching is then stopped, leaving the structure shown in Figure 5.16, wherein is seen a sharp tip aligned to a counter electrode [111]. Figure 5.23 illustrates the final stage of the fabrication processing.

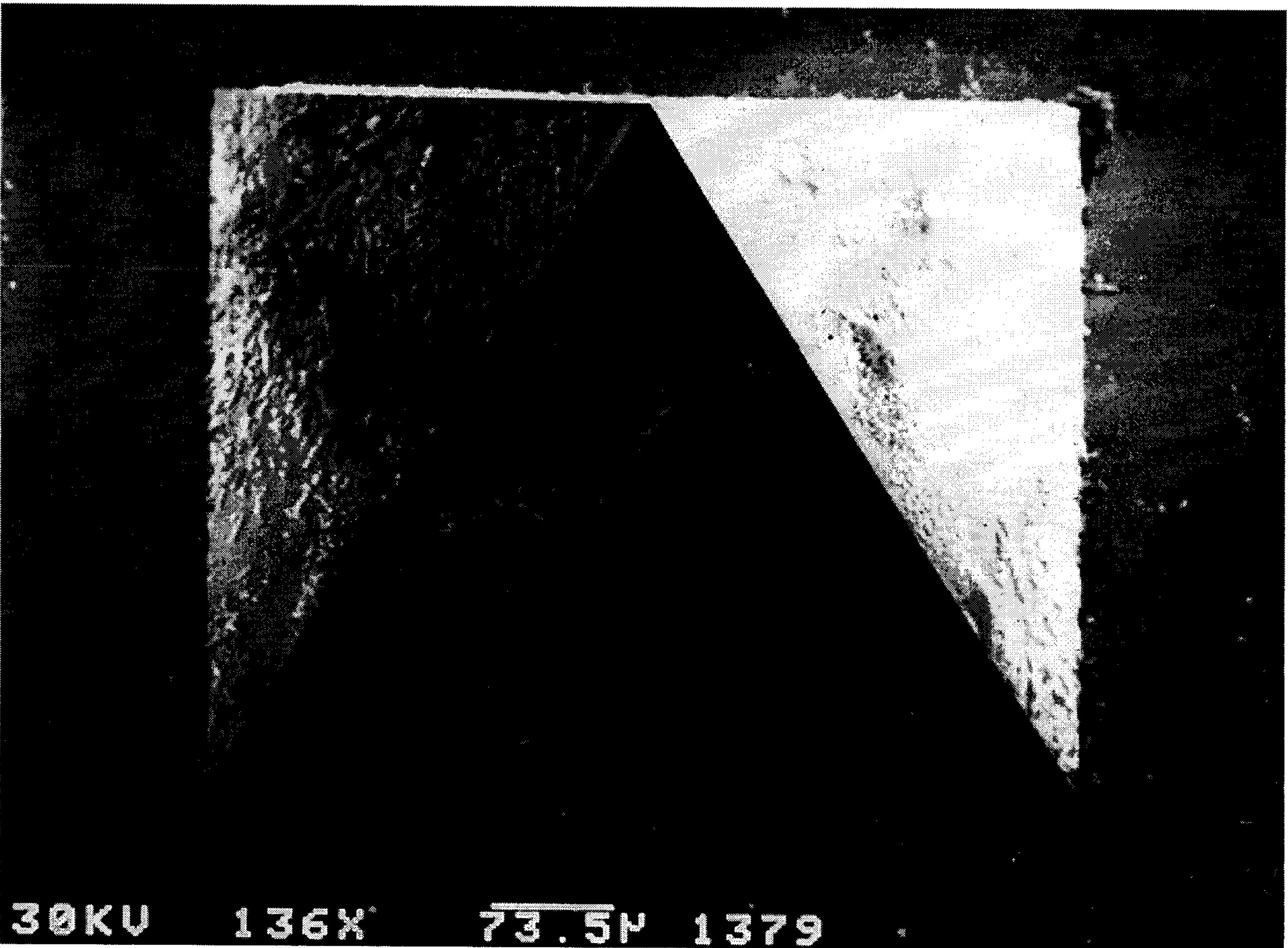

Figure 5.17 SEM picture of a tip in micromachined by electroplating gold into a silicon mold as fabricated in Figure 5.11. This is achieved without oxide formation in the fabricated pit [89]

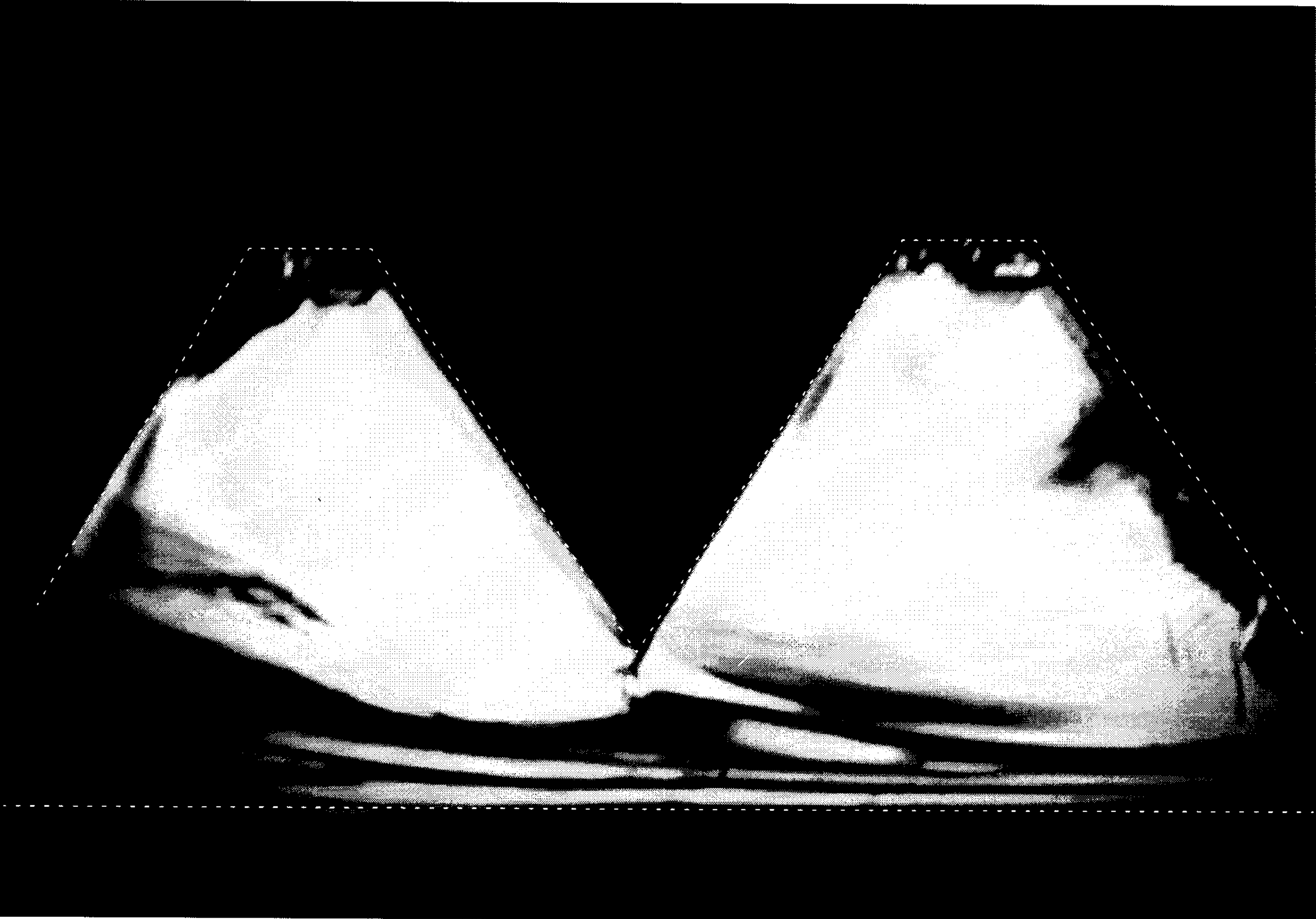

Figure 5.18 Optical picture of an array of pits.

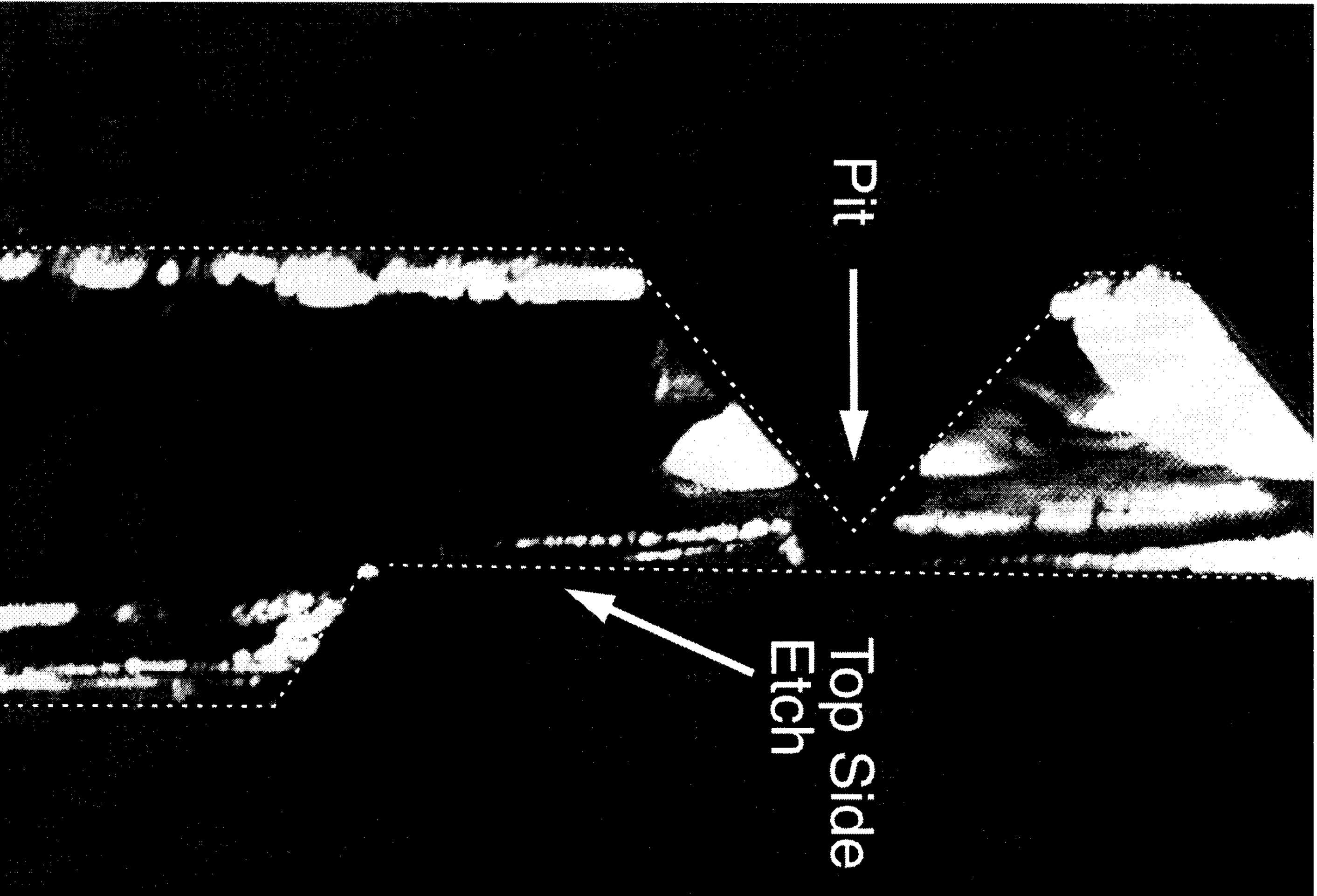

Figure 5.19 The cross-section of the silicon wafer after it was etched from both sides.

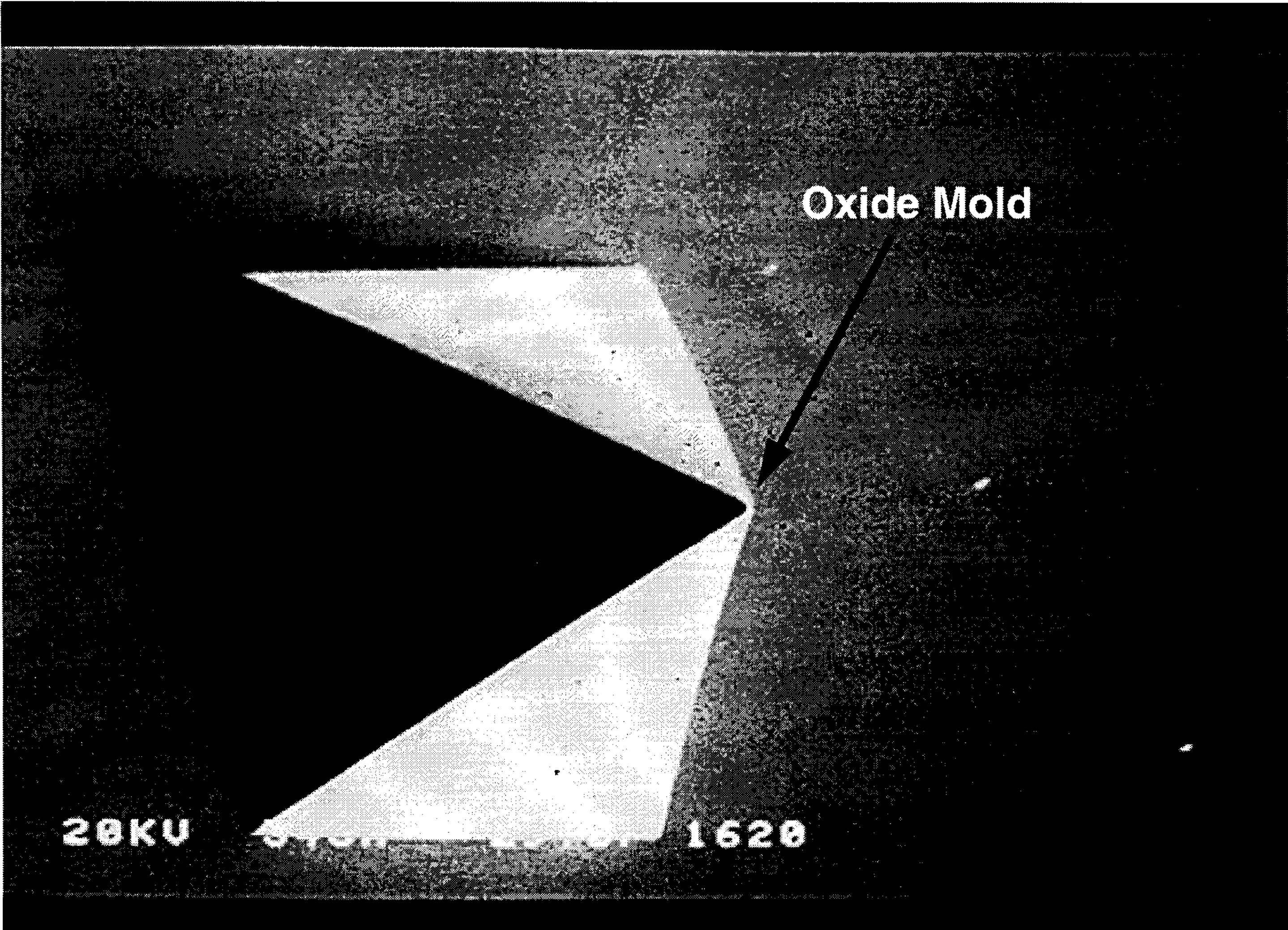

Figure 5.20 SEM picture of the oxide mold visible from the top of the wafer.

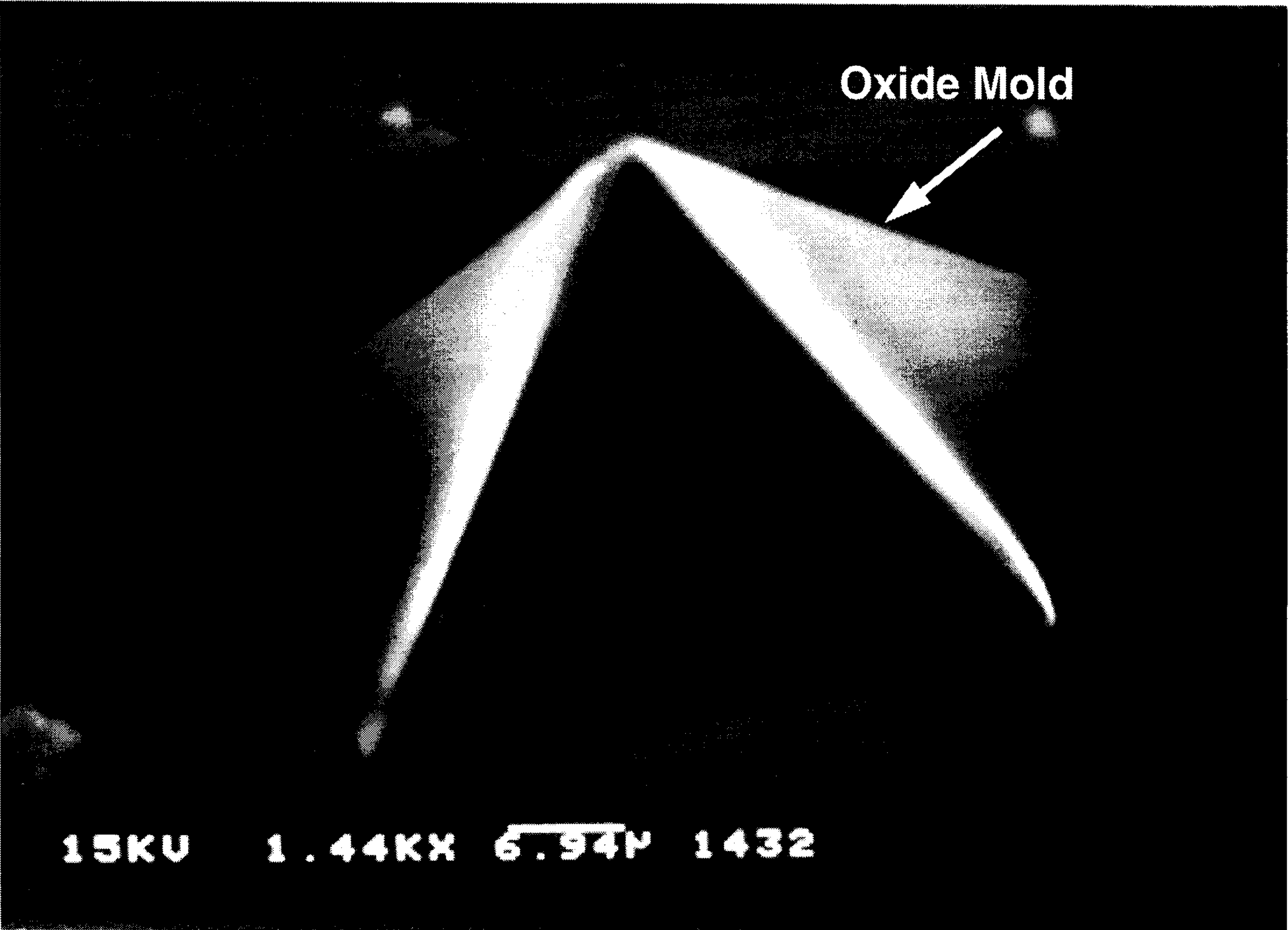

Figure 5.21 Another SEM picture of the oxide mold visible from the top.

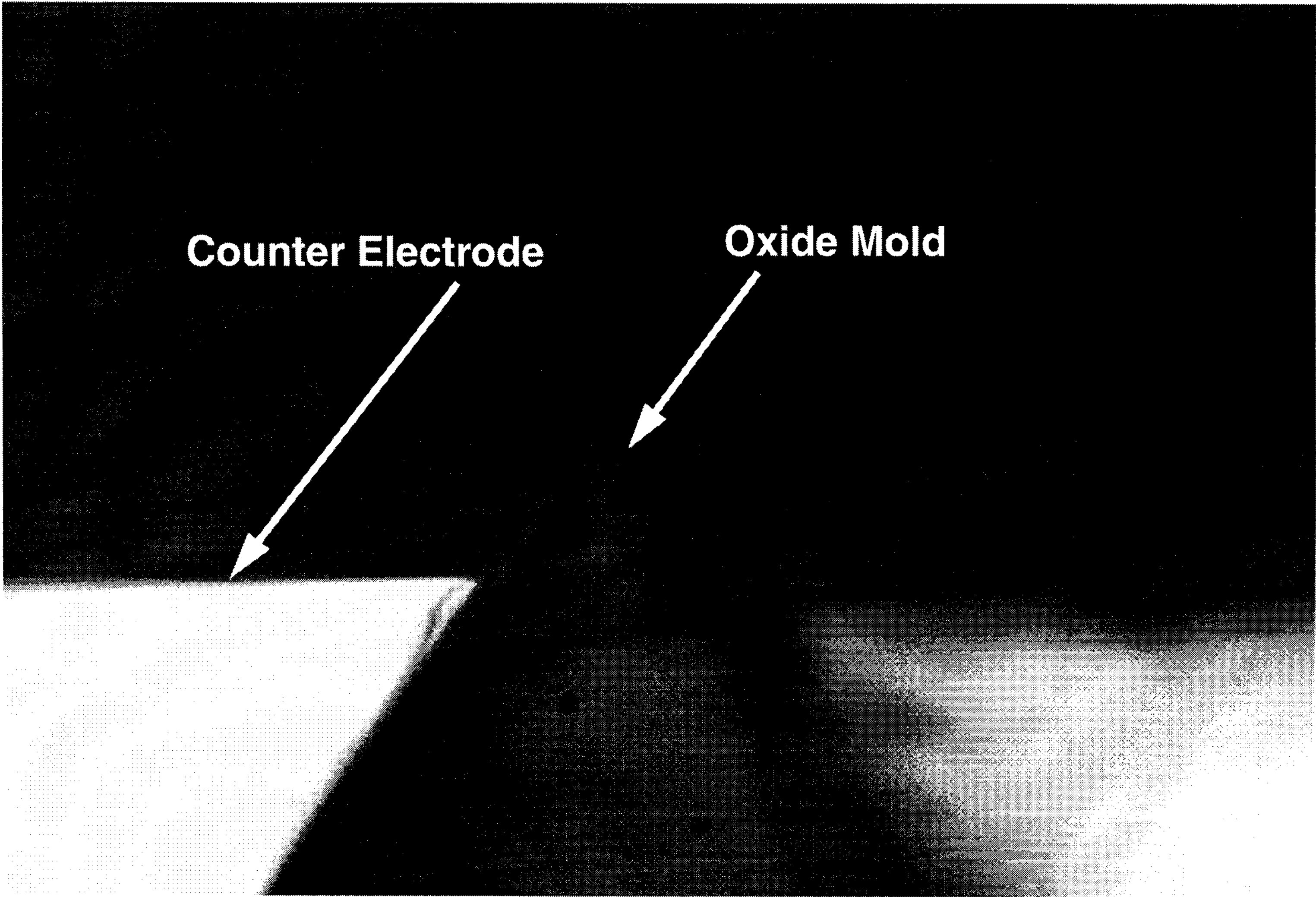

Figure 5.22 Optical picture of the cross-section of the oxide mold with respect to counter electrode.

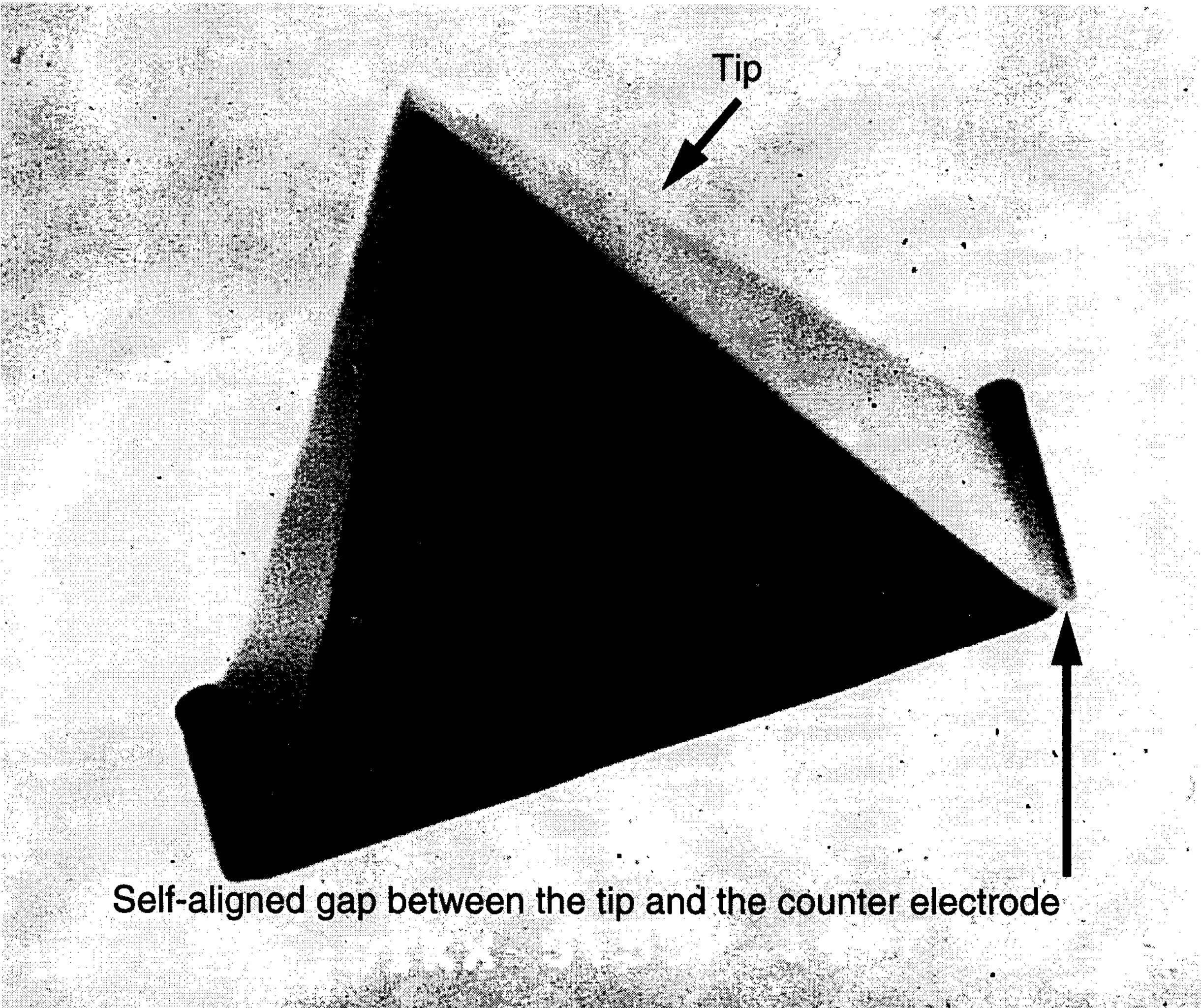

Figure 5.23 SEM picture of the oxide mold visible from the top of the wafer.

The basic process which was described can be modified by adding dopant to the counter electrode to increase its conductivity. This step is optional for wafers whose conductivity is rather low. This expanded process proceeds from the processing stage depicted in Figure 5.14 wherein the top side of the wafer with the silicon oxide mold is subjected to diffusion. This step is shown in Figure 5.24. During the diffusion a thin layer of oxide is also grown on the diffused area. After this step, a seed layer is deposited into the silicon dioxide mold structure followed by an electrodeposition of a thick layer of gold to fill the hole (see Figure 5.25). This can be extended over the mold if the depth is smaller than the thickness of the deposition. The final processing step is similar to the previous method, which was to etch away the silicon as shown in Figure 5.26.

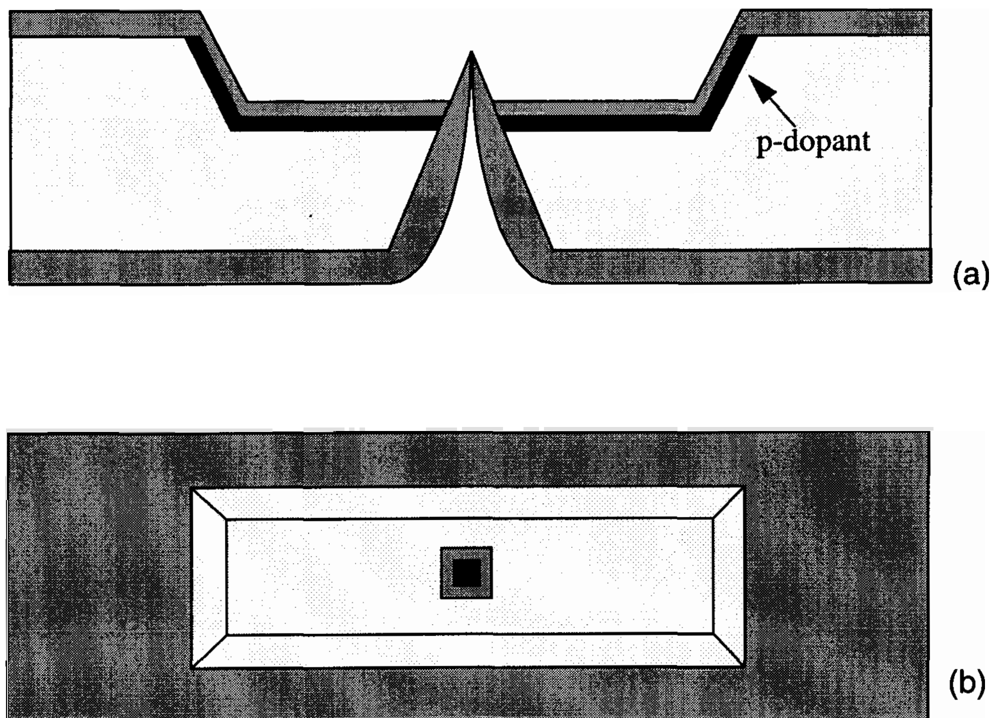

Figure 5.24 The cross-sectional view (a) and the top view (b) of a single-layered substrate having dopant on the top surface for the counter electrode.

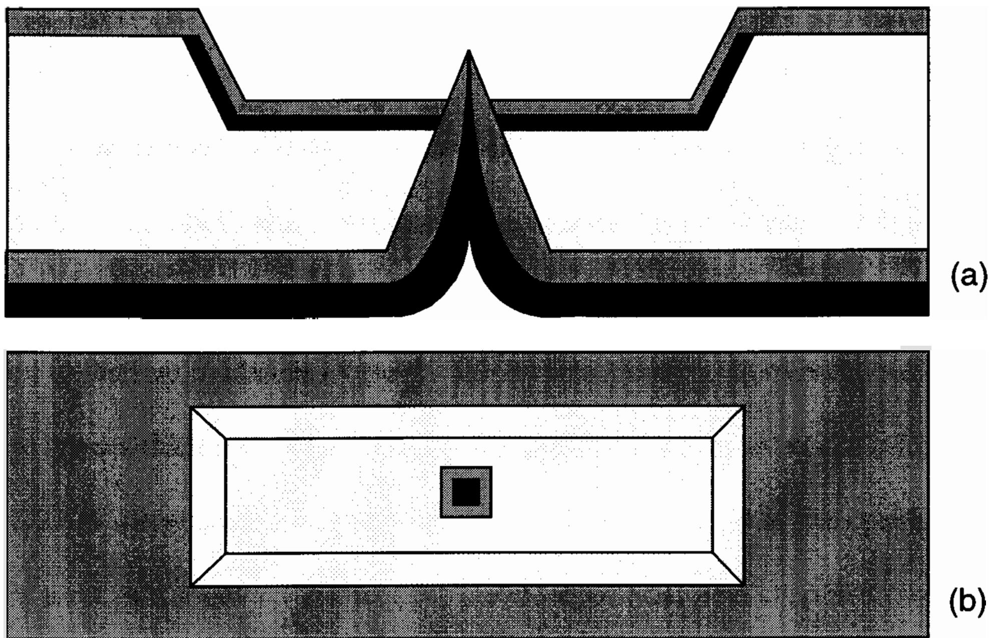

Figure 5.25 The cross-sectional (a) and the top view (b) of a single-layered substrate having a metal electroplated into the oxide mold.

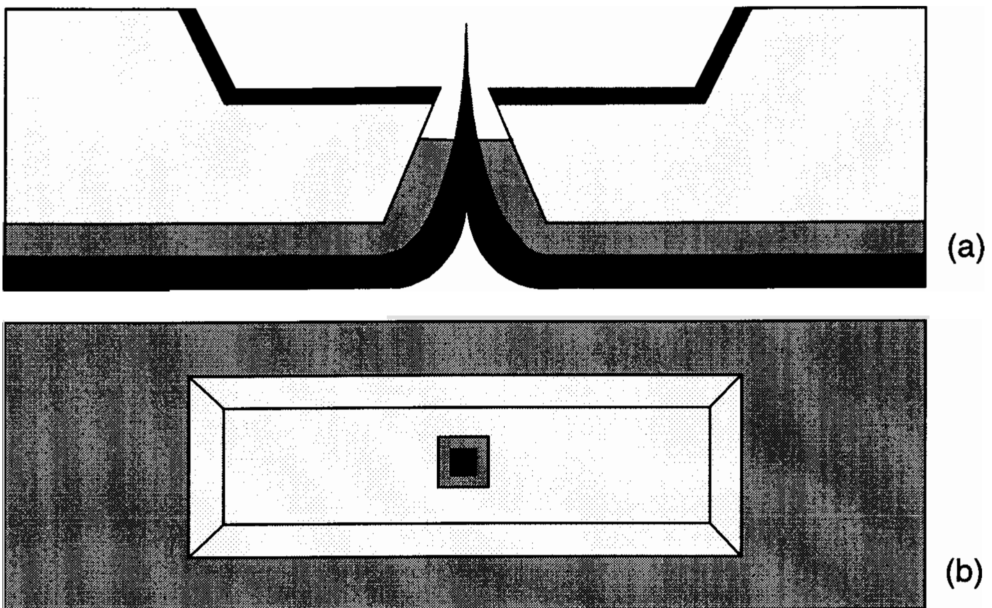

Figure 5.26 The cross-sectional (a) and the top view (b) of a single-layered substrate having the highly doped counter electrode.

5•2•2•1 An Alternative Fabrication Process

Here, an alternative method of creating a self-aligned tip is proposed and discussed. This method basically continues from the step shown in Figure 5.14. The next step in this method is to etch away the entire silicon dioxide layer on both sides of the wafer by a B.O.E. solution, leaving the structure shown in Figure 5.27. The wafer is then subjected to thermal oxidation to grow a silicon dioxide layer all over the wafer. The idea here is to grow a thick layer of silicon dioxide to allow the four sides of the hole shown in Figure 5.27 to merge and close the hole. This will create a cusp at the opening of the pit which is used as a mold for subsequent metal deposition. The cusp is shown in Figure 5.28. This is in fact created because the oxide growth is dependent on crystal orientation. This was investigated by Deal [93] and is shown in Figure 5.29. This graph illustrates that the oxide growth is larger in the {111} than the {100} plane only if the oxidation process

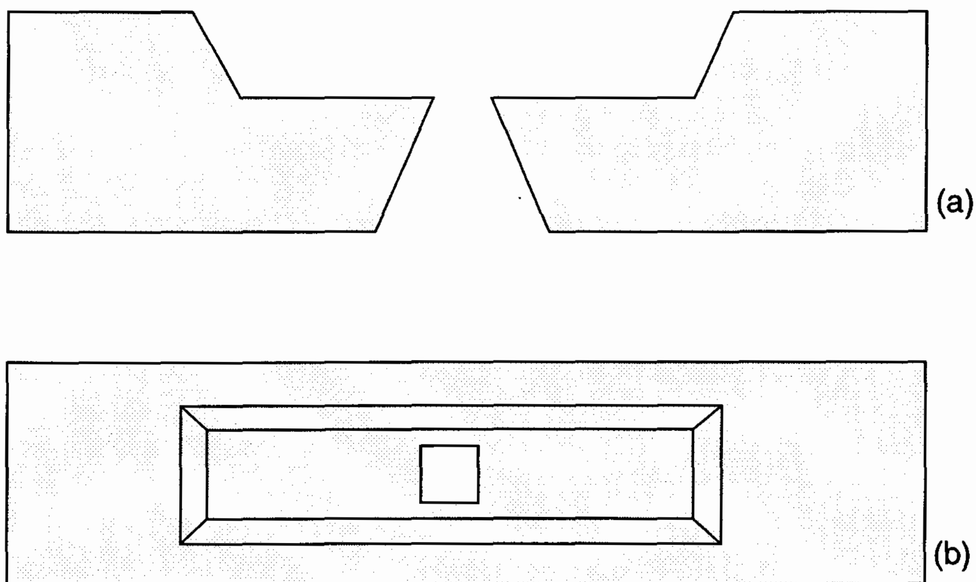

Figure 5.27 The cross-sectional (a) and the top view (b) of a single-layered substrate having silicon dioxide layer removed from both sides of the wafer.

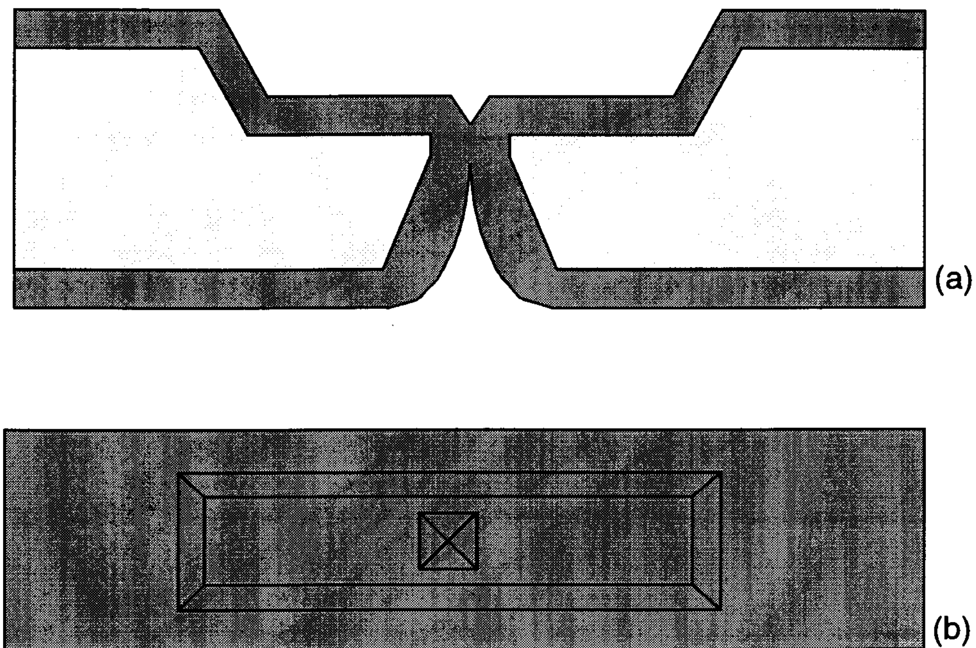

Figure 5.28 The cross-sectional (a) and the top view (b) of a single-layered substrate having the silicon dioxide grown on both sides of the wafer.

is done at temperature lower than 1100° C. At or above this temperature, the rate of the growth on this two planes becomes identical. However, at a temperature of 900°C, it can be seen that there is a maximum difference between the two rates. Figure 5.30 illustrates the oxide thickness for the three important crystal planes in micromachining at 900°C. It is evident that as time goes on, the difference between the three planes become more noticeable. The rate is highest on {111} and lowest for {110} plane.

The oxide formation shown in Figure 5.28 was investigated using a process simulation package called ATHENA by Silvaco. ATHENA is computer software that is used to simulate various processing steps used in making semiconductor integrated circuits. Instructions for its use are contained in its operating manual [91]. For the purpose of the simulation a rather narrow gap was defined to speed up the simulation process, as it

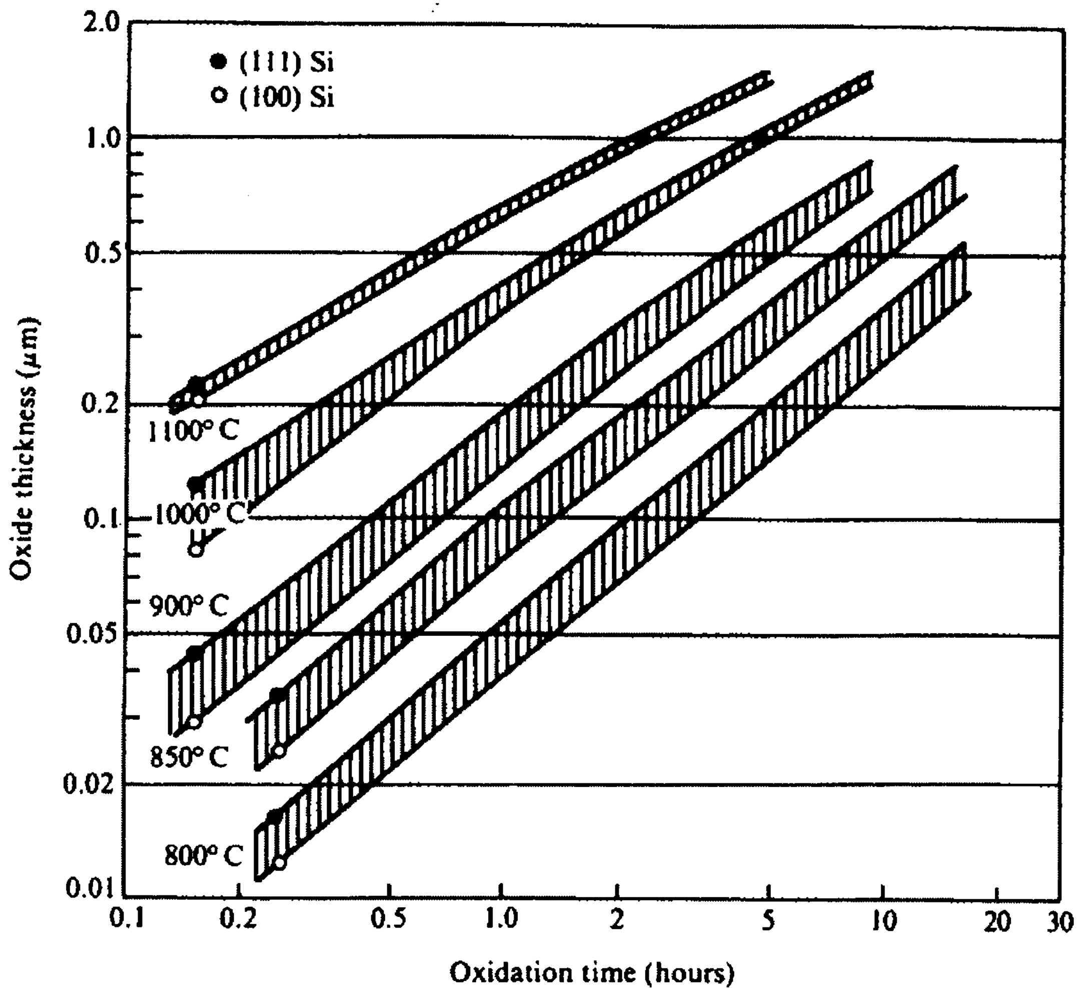

Figure 5.29 Oxide thickness versus oxidation time for silicon oxidation in water vapor (0.87 atm.) [93].

usually takes a while to simulate the actual sized structure. It can be seen from the results of the simulation shown in Figure 5.31-5.39 that the rate of oxide growth on the {111} planes at 900°C is in fact faster than the {100} plane. And, as time passes, the oxide at the opening of the pit merges (see and Figure 5.34). It is also evident that the sharp corners of the silicon pit gradually disappear. Because the oxide that surrounds this area becomes thicker than the rest of the region, the oxidation rate becomes slower.

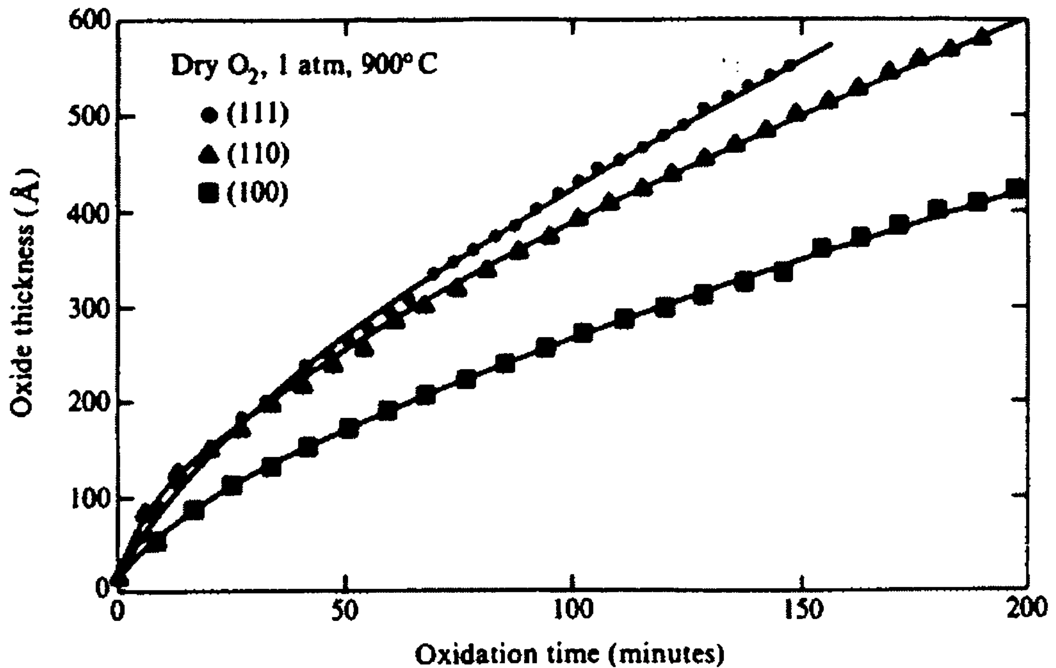

Figure 5.30 Oxide thickness versus oxidation time during initial stages of silicon thermal oxidation [92].

After this step, a thick gold layer is electroplated onto the seed layer inside the silicon dioxide mold structure (see Figure 5.35). This step is performed as in the previous technique. The final processing step is to etch away the silicon dioxide layer from the top, using a B.O.E. solution, leaving the structure shown in Figure 5.36.

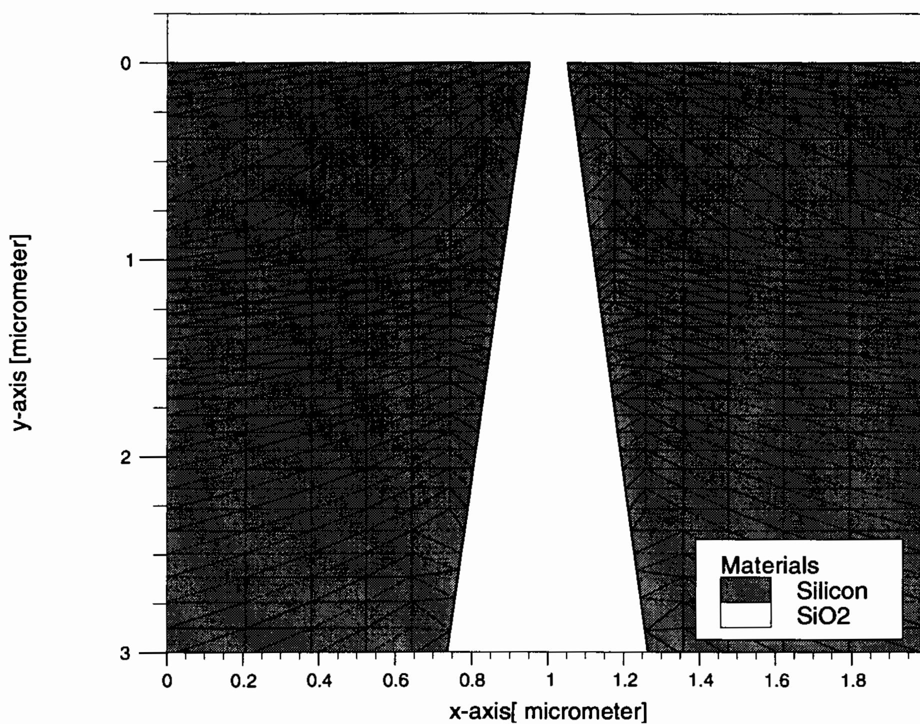

Figure 5.31 The oxide thickness at beginning.

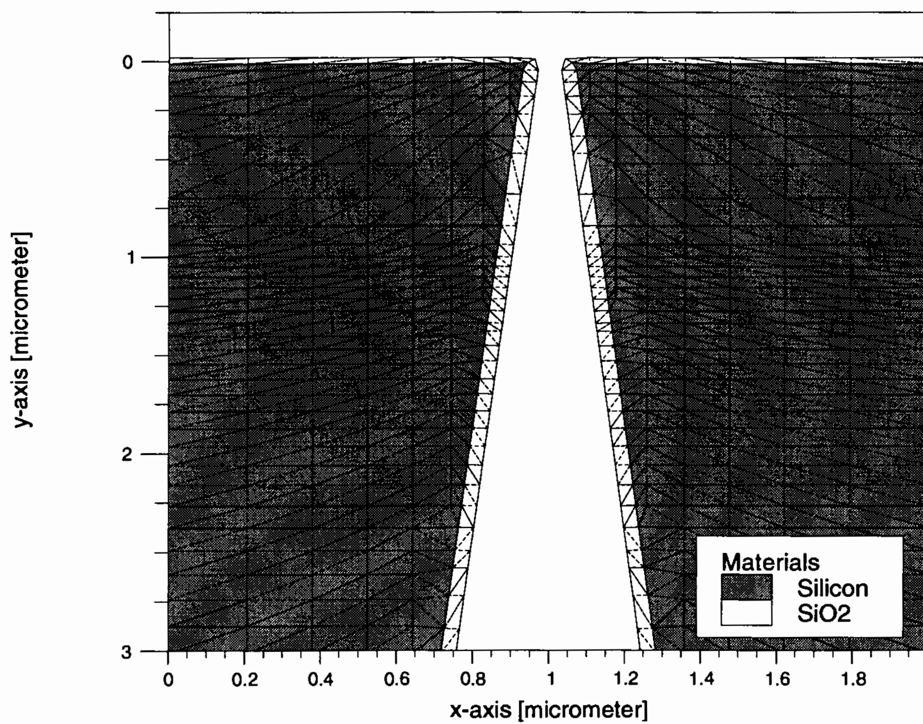

Figure 5.32 The oxide thickness after 1 minute.

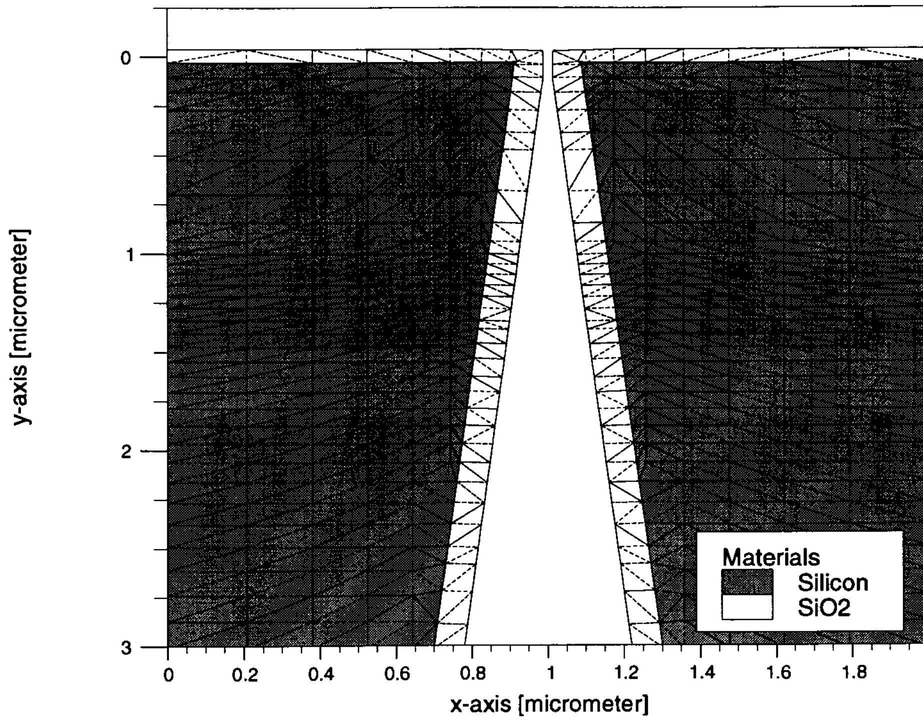

Figure 5.33 The oxide thickness after 1.3 minutes.

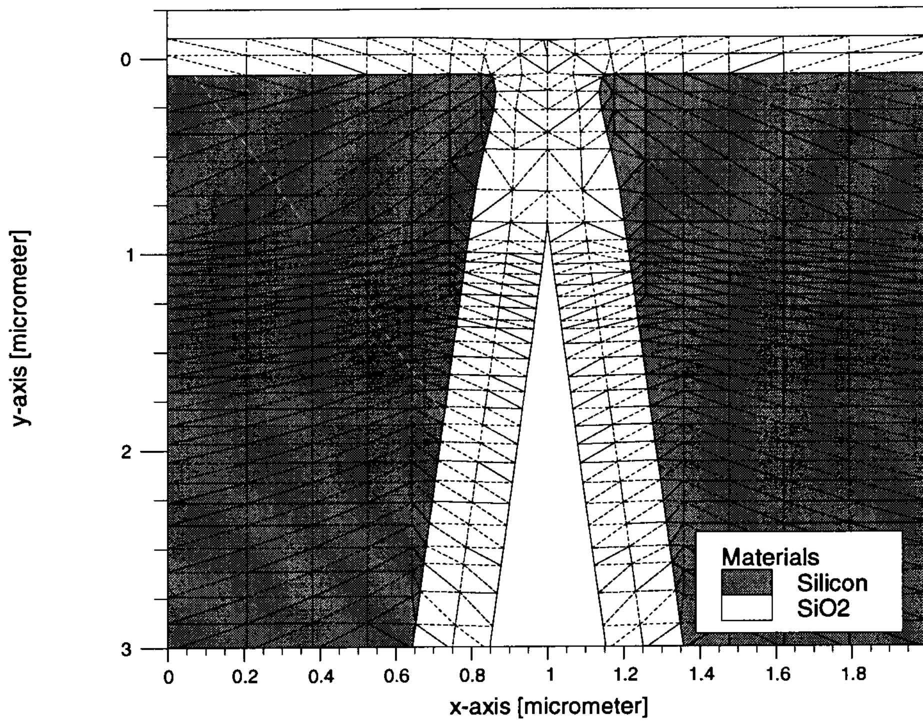

Figure 5.34 The oxide thickness after 4.5 minutes.

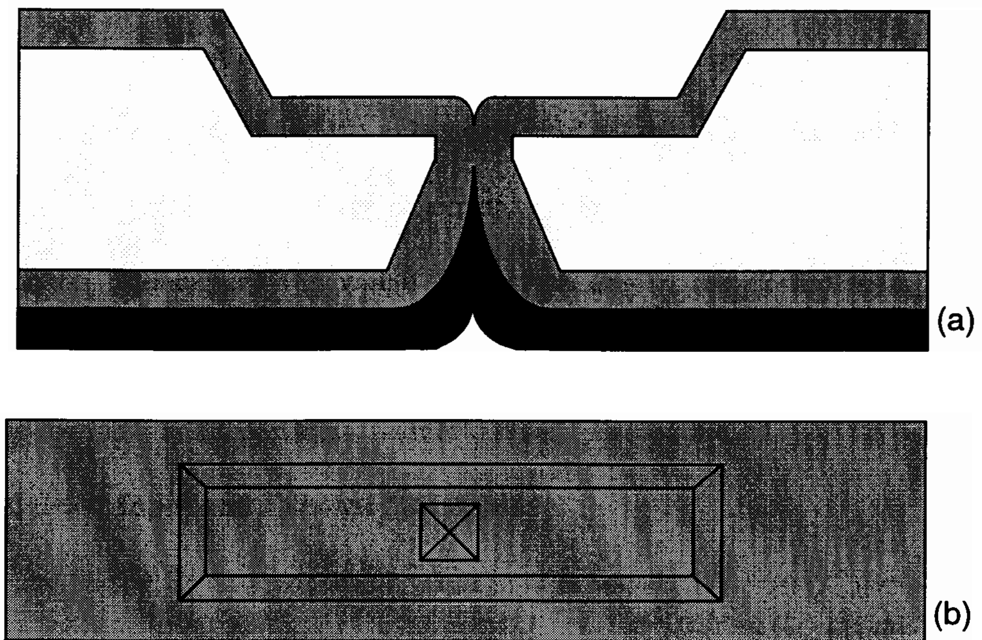

Figure 5.35 The cross-sectional (a) and the top view (b) of the electroplated metal into the silicon dioxide mold.

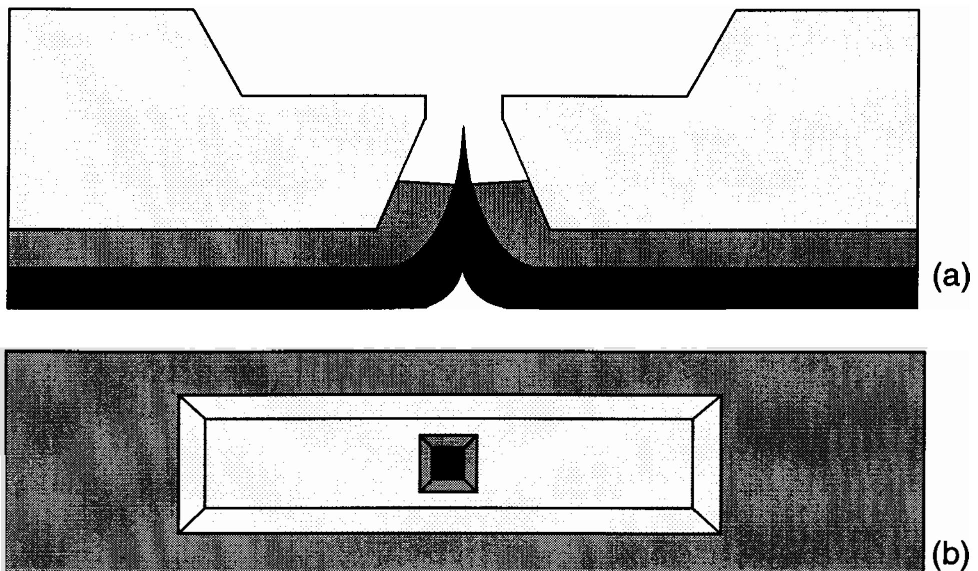

Figure 5.36 The cross-sectional (a) and the top view (b) of the removed oxide from the top part of the wafer.

5•2•3 Assembly Phase

The final assembly phase involves mounting the internal (i.e., counter electrode) and the external (i.e., input and the exhaust manifolds tubing) hardware and the electrical connections. Figure 5.37 shows the schematic diagram of the final device with one field ionization tip. The sequence in which these steps were accomplished is important with respect to being able to rapidly correct process-induced defects. The first step involved attaching the input and the exhaust manifold tubes to a metallic lid.

5•2•3•1 Input and Exhaust Manifolds

The reason for this step to be taken first, is because the epoxy[5] used to bond the glass tubes to the metallic lid can flow too much during curing, which may obstruct the opening in the metallic lid. As long as access is maintained to the back surface of the metallic lid, a small metal probe can be used to clear the opening. However, if the tube were to be attached after connection to the silicon wafer, the epoxy obstruction problem would be irreversible. Figure 5.38 shows the results of a successful glass tube attachment.

5•2•3•2 Electrical Connection

Once the gas inlet epoxy cured (and was visually inspected to ensure that there was no obstruction on the interconnect tubes), the interconnects are carefully connected to the tip and the counter electrode by silver conductive paint[6]. Each lead was threaded separately to its respective electrode using a pair of wire-bonding tweezers. Then the device, with the paint, is left inside an oven at 80°C for a few hours to be cured. The other end of the leads are connected to a triaxial connector for an easy hookup to a

---

5. 5 MINUTE EPOXY^R, manufactured exclusively by Devcon Corporation, Danvers, MA, USA.
6. Silver conductive paint, Acheson Colloids Canada, P.O.Box 665, Brantford, ON,N3T 5P9.

semiconductor parameter analyzer. Figure 5.39 shows the result of a successful connection of the electrical leads to the gold plate and the fabricated tip.

5•2•3•3 Counter Electrode-to-Wafer Bonding

Once the input and the exhaust manifold tubing were successfully attached to the metallic lid, then it was positioned over the micromachined cavity where the tips are located. With the help of a low-power binocular microscope, the metallic lid and the micromachined cavity on the silicon chip were carefully aligned so that the plate is right on the centre of the chip and covers the cavity. Next, the metallic lid was secured to the chip with adhesive tape on two opposite sides. Finally, the edges of the metallic lid were carefully covered with epoxy to seal the electrode to the chip. After the epoxy cured the adhesive tape was removed and the epoxy was applied to seal all edges. After this, a visual

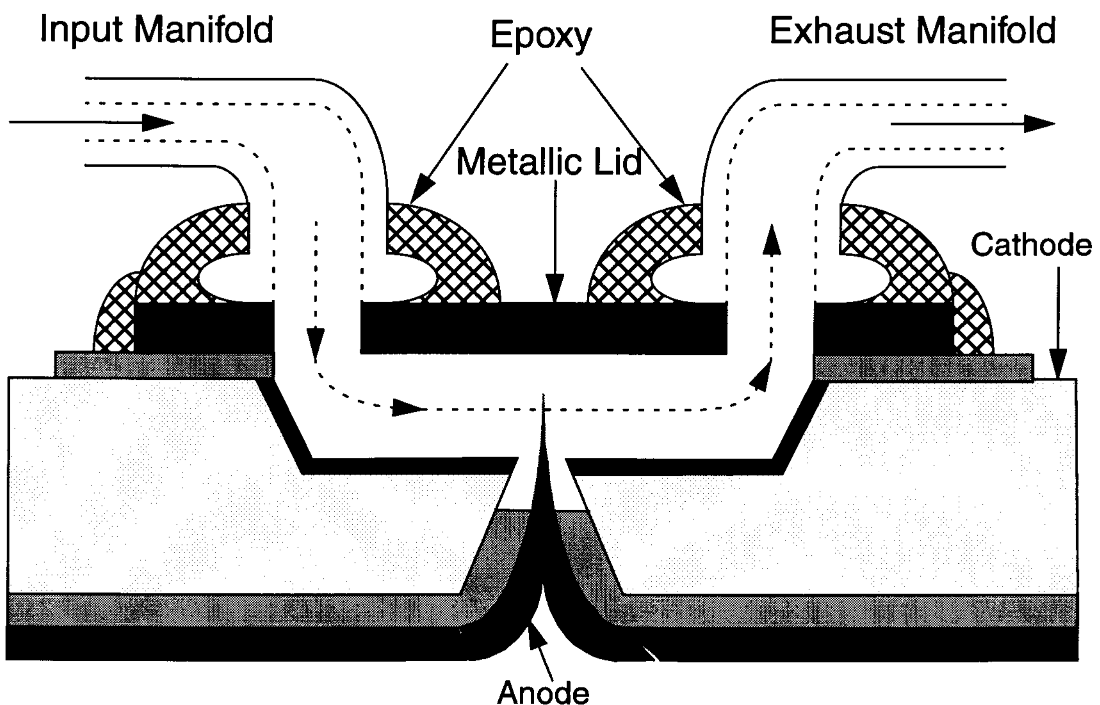

Figure 5.37 The cross-sectional view of the final micromachined field ionization detector.

inspection was carried out by a microscope to look for any voids in the epoxy.

5•2•3•4 Packaged Device

The last step in the assembly of the micromachined field ionization detector involved installing the detector inside an aluminum box to reduce the noise level as much as possible and to provide a mechanical support for the triaxial connector as well as the connection tubes. The packed device is shown in Figure 5.40.

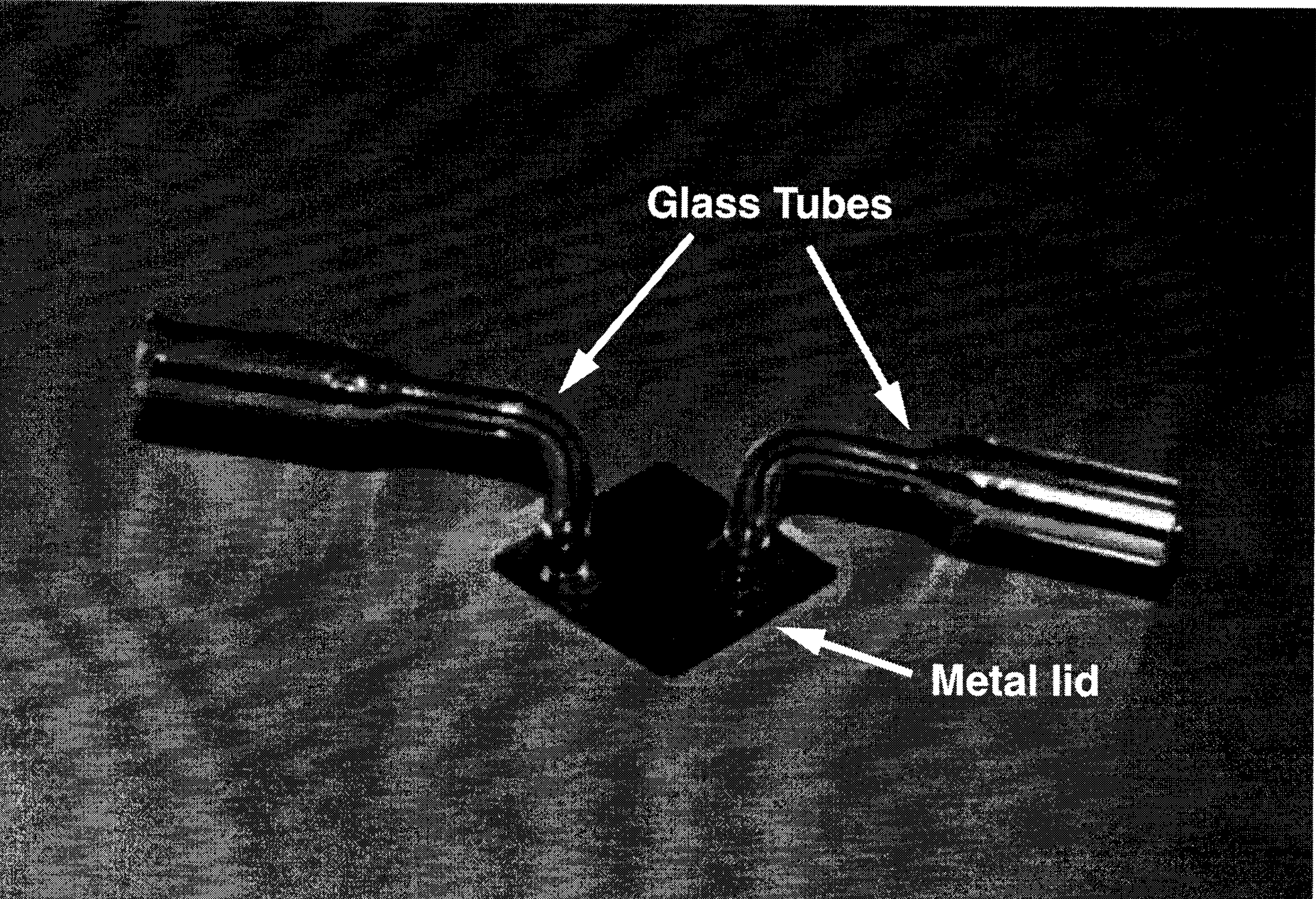

Figure 5.38 Picture of the input and exhaust manifolds attached to the metallic lid.

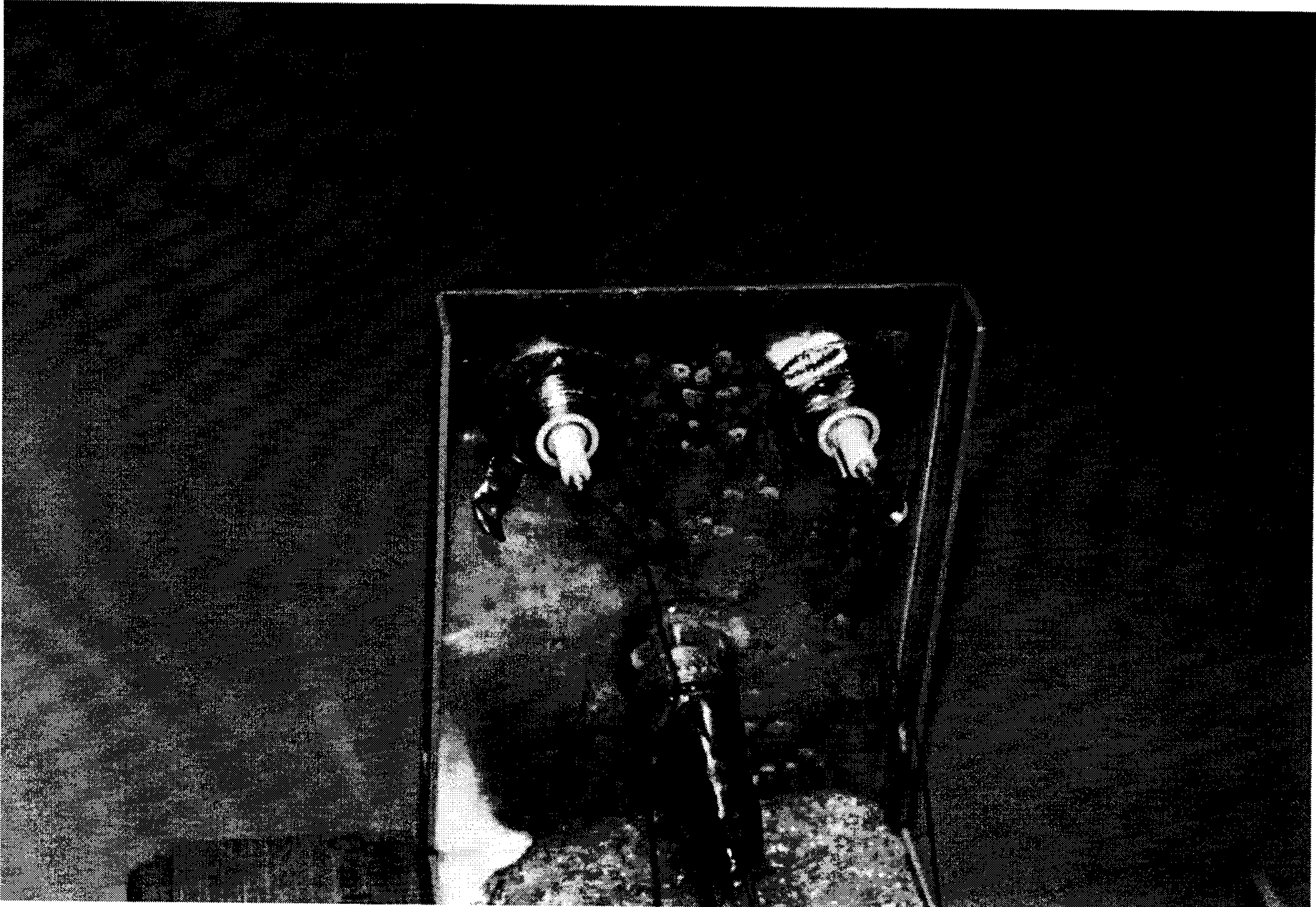

Figure 5.39 Picture of the electrical connector.

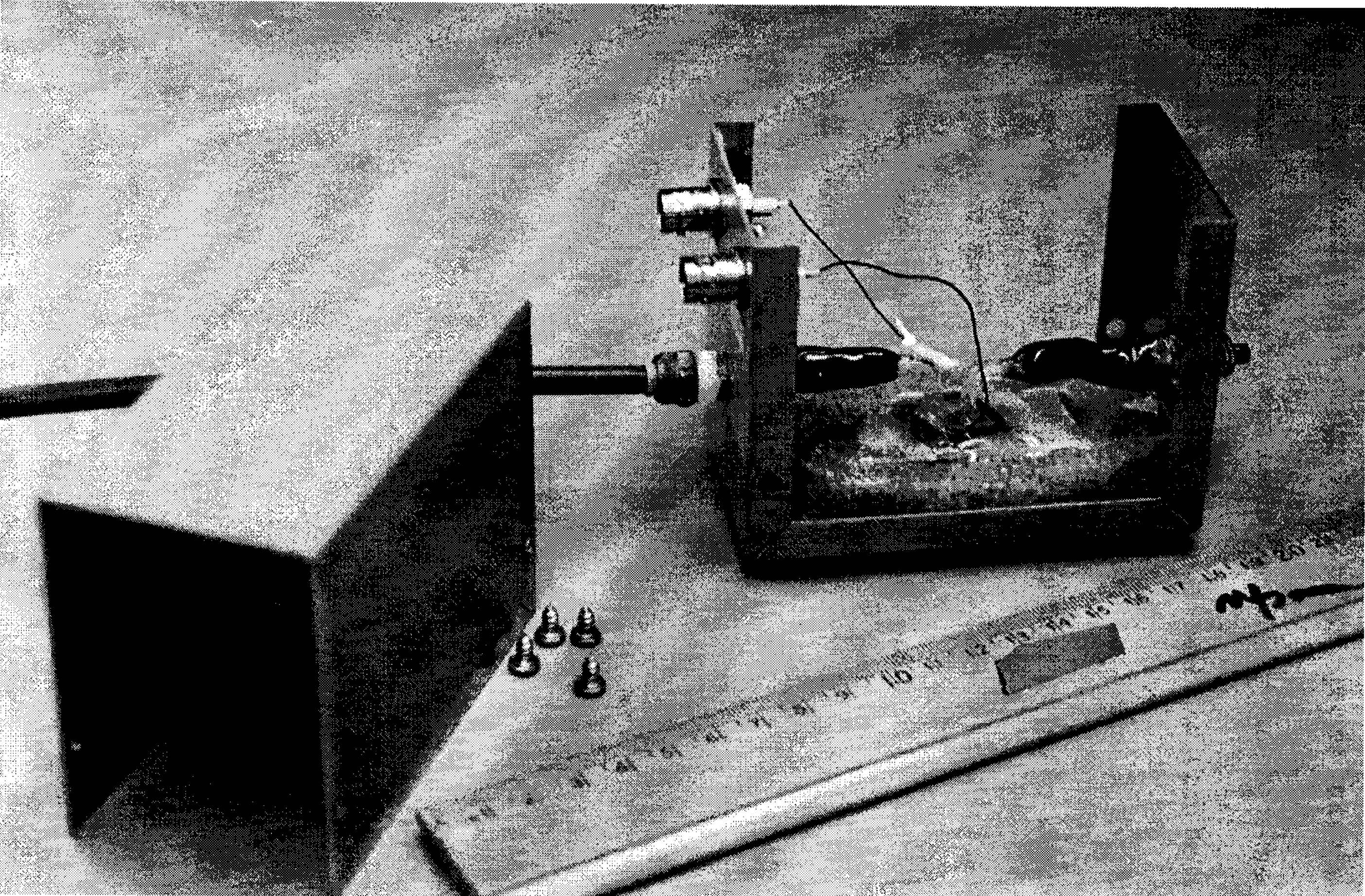

Figure 5.40 The view from one side of the aluminum box.

5•3 Summary

This chapter discussed the design issues of the specific micromachined field ionization tip based upon the theory presented in Chapter 3. Beginning with a justification for the low-cost method for the formation of a sharp tip and how it can be achieved with standard equipment, the geometrical and fabrication sequences of the detector were established. The next aspect of the micromachined field ionization detector involved devising an appropriate sample gas generation and delivery system, as well as an instrumentation interface capable of recording signals produced by the field ionization detector. This is discussed within next chapter.

Chapter 6

Characterization of Micromachined Field Ionization Detector

This chapter presents and discusses the results of various measurements performed on the micromachined field ionization detector that was fabricated using the fabrication method, discussed in Chapter 5. These measurements are intended to prove the usefulness of the concept of field ionization for the detection of gases and its sensitivity to some sample gases. In this respect, this chapter is divided into two sections. The first section describes the experimental setup that was selected to perform the gas generation and delivery function, and the necessary electrical measuring instrumentation interface to measure and record the data points.

The second section discusses the results obtained by various measurements performed to characterize the detector. This allows the detector to be calibrated under a few important operating conditions such as the sensitivity to different sample gases, applied voltages, and sample gas concentration. These specific conditions are necessary to know in order to understand the detector behavior for the purpose of its integration in future micromachined gas chromatography system designs.

6•1 Experimental Setup

The micromachined field ionization detector characterization system setup consists of two subsystems, the gas generation and delivery system and the electrical measurement system. In order to generate a reproducible concentration of sample gases

and deliver them to a detector consistently for all gases, a number of different approaches have been experimented with. However, the approach which proved to be the most reliable one is the one used widely by chemical analytical laboratories to characterize their instruments. This approach uses permeation tubes[8] and was utilized by Reston in his thesis to characterize his micromachined detector [24], and so it was used as the basis of the characterization technique in this work. The method he presented is simpler than its predecessors in both equipment and application.

This method requires no cumbersome or delicate equipment and can be easily set up with simple off-the-shelf equipment. The basic setup requires two gas flowmeters[9], one of them to measure the flow of carrier gas which goes through the U-tube. The other one is used to measure the flow of gas through the detector. Their functions will be explained later in this chapter. Flow rate is very important for the calculation of the sample gas concentration. For a specific value of the flow rate of carrier gas there will be a constant generation of the desirable diluted sample gas.

6•1•1 Gas Generation and Delivery System

The schematic diagram of the gas generation and delivery system used for the calibration of the detector is shown in Figures 6.1 and 6.2. In this system the measurement is designed to characterize the detector for a steady-state condition. There are three main components: the carrier gas, the sample gases generation tube and the detector measurement interface (not shown here, but shown in Figure 5.37). These individual components will be elaborated upon in the next few sub-sections.

---

8. VICI Meteronics Inc., 2991 Corvin Drive, Santa Clara, CA 95051 USA.
9. Matheson Gas Products Canada, 12143-68 Street, Edmonton, AB, T5B 1P9, CANADA.

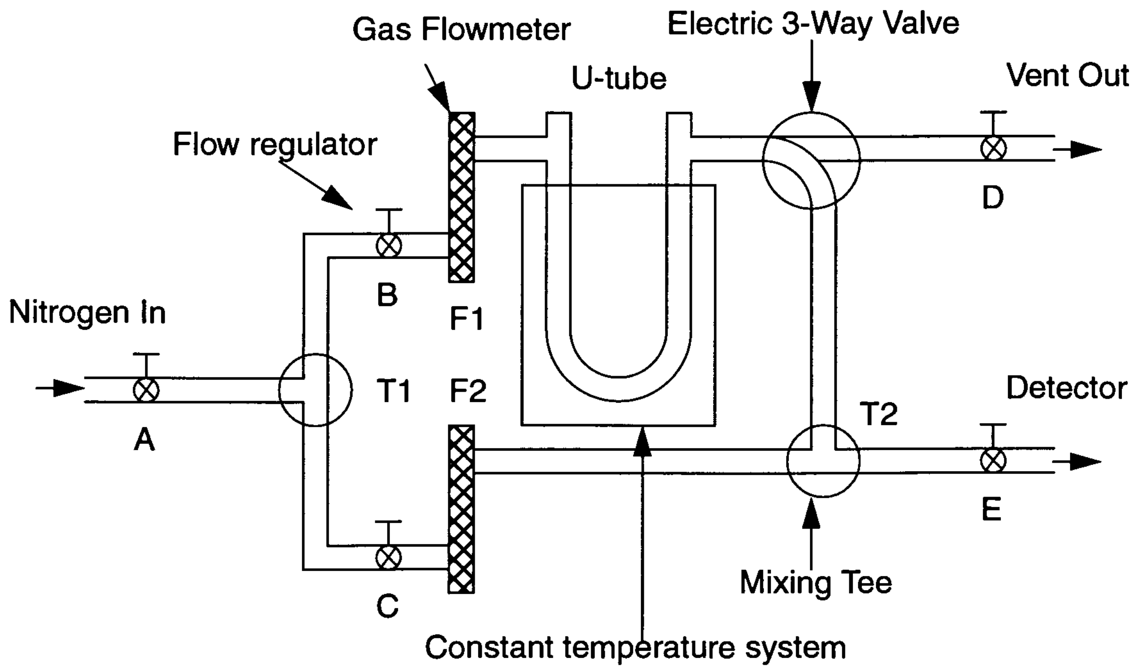

Figure 6.1 The schematic representation of the basic gas generation and delivery system.

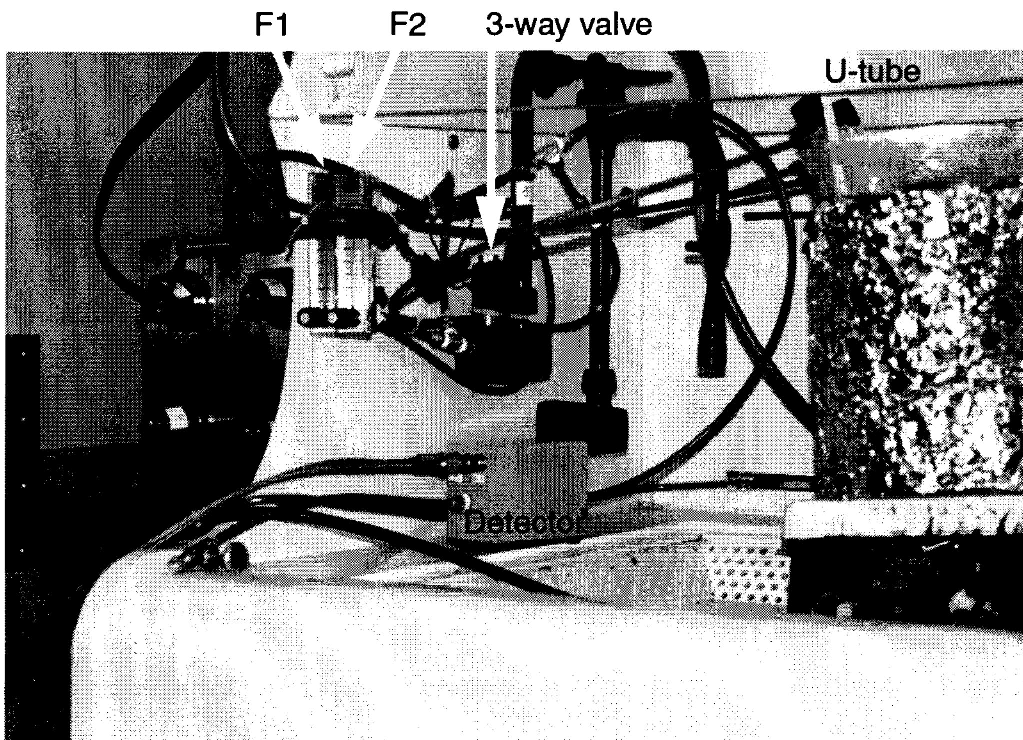

Figure 6.2 The picture of the basic gas generation and delivery system.

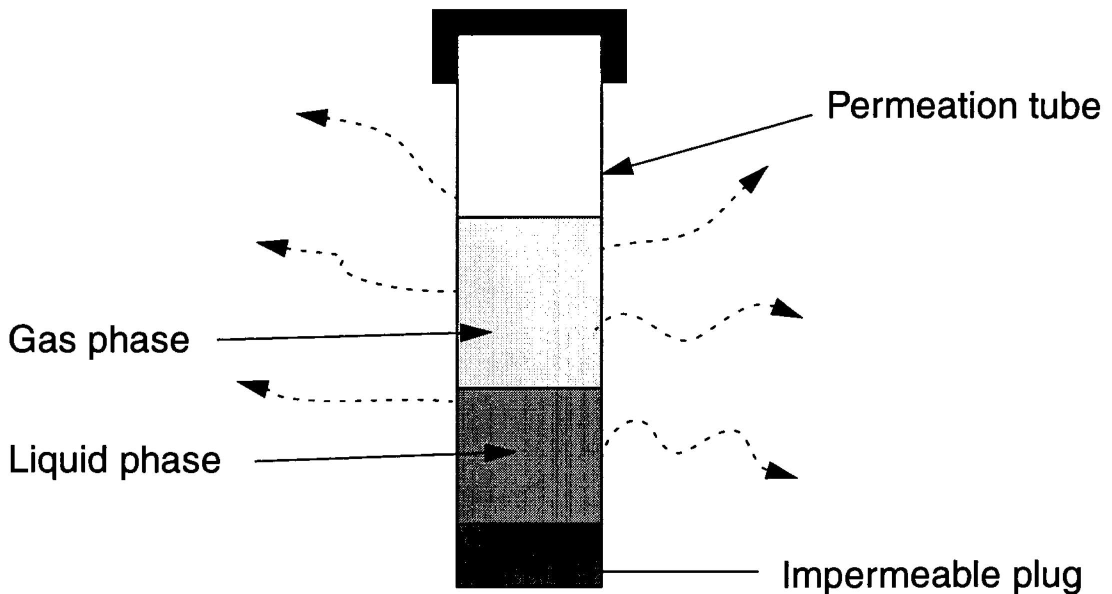

Figure 6.3 Schematic diagram of a permeation tube.

6•1•2 Carrier Gas

In a field ionization gas detector, the choice of the carrier gas basically depends on the ionization potential of the carrier gas used and its inertness to sample gases. In order to detect the sample gas effectively in the carrier gas, the carrier gas is required to have a significantly higher ionization potential relative to sample gases. Helium has the highest first ionization energy (2372 kJ mol^{-1}). However, we used nitrogen (1402 kJ mol^{-1}), which is also a high ionization energy relative to the sample gases, simply because of the easy accessibility and low cost. As will be shown later in this chapter, this choice was sufficient choice for the detection of the sample gases.

6•1•3 Sample Gases

We have chosen three sample gases to calibrate the micromachined field ionization detector. These are NO_2, NH_3, and CH_3COOH. In our approach the permeation tubes

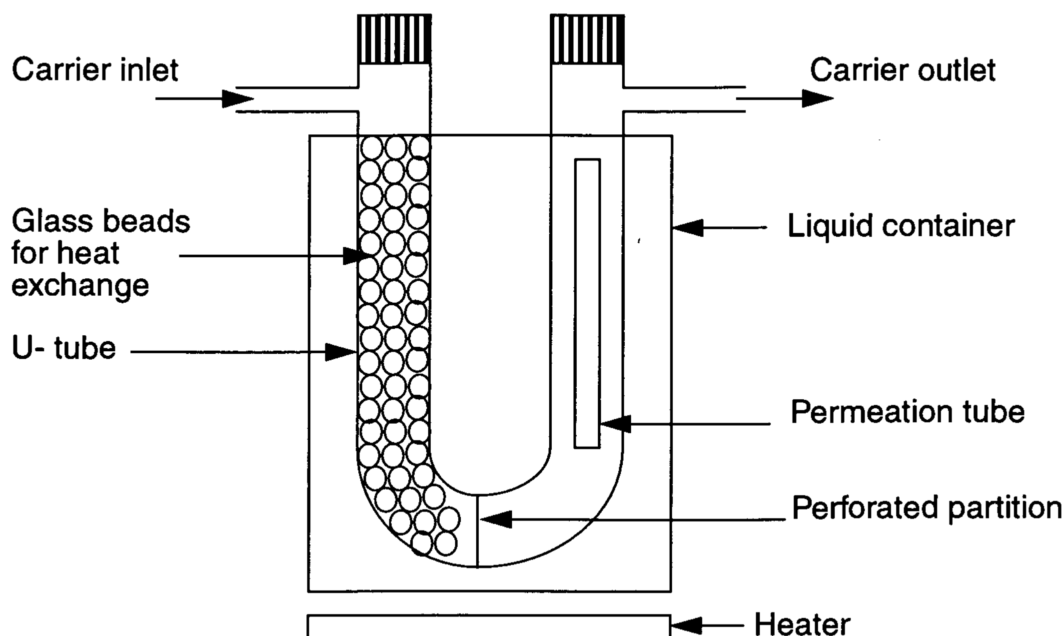

Figure 6.4 The schematic diagram of the permeation tube in a U-tube holder.

were used for the generation of the sample gases. These tubes provide a good method of producing a gas concentration in the ppm level for the calibration of the detector. The basic parameters needed to estimate the sample gas concentration are the constant temperatures at which the tubes are maintained and the constant carrier flow rate over the tubes. At constant temperature, the tube permeates the compound through its permeable portion at a constant rate, as shown in Figure 6.3. When the permeation tube is inserted into a constant carrier gas flow, as shown in Figure 6.4, then the concentration of the sample gas is calculated from the parameters mentioned.

Since the permeation process in the tube is strongly temperature dependent, provision is made within the gas generation system to monitor it by a thermocouple attached to the permeation tube's surface. The temperature is then used to maintain the

system at a given constant temperature.

For interconnect tubing, tubes, with 1/4" in diameter, were used. They are made out of a polymer (fluorinated ethylene propylene resin) which are inert to most compounds, sufficiently elastic and commercially available [112].

6•1•3•1 Calculation

Concentration

The sample gas concentration is calculated using equation (6.1), provided to us by the manufacturer. In this equation, the reference condition is defined to be at room temperature (25 °C) and atmospheric pressure (760 mm Hg)

$$C = \frac{R\left(\frac{24.46}{W_a}\right)}{F_c} \tag{6.1}$$

where C is the concentration of the sample gas generated in ppm by volume, R the permeation rate in ng/min, W_a the molecular weight of the pollutant gas, F_c the total flow rate of the carrier gas in ml/min, corrected to the standard condition. The constant 24.46 is the molar volume at the reference condition.

Temperature Change

The rate of permeation is temperature dependent, too. And so the temperature parameter can also be used to specify a certain sample gas concentration. Equation (6.2)[10] is used for calculating the rate of permeation at a given temperature is

$$\log R_1 = \log R_0 + \alpha(T_1 - T_0) \tag{6.2}$$

10. Provided to us by VICI Metronics Inc.

where R_0 is the rate at temperature T_0(°C); R_1 is the required rate at temperature T_1(°C); and α is the temperature coefficient[11]. The rule of thumb is for each 1 °C increase in temperature, there will be a 10% increase in the permeation rate.

By using the system shown in Figure 6.1, a limited range of sample gas' concentration can be obtained for NO_2, NH_3 and CH_3COOH. For example, if the lowest flowrate setting is used (100 ml/min), the NO_2 permeation tube is able to generate a concentration of 14 ppm (at 35 °C), for NH_3 7 ppm (at 35 °C), for CH_3COOH a 4 ppm (at 35 °C) to 57 ppm (at 110 °C). Thus, concentration ranges from 0 ppm (with the tube disconnected) to these maximums (at their respective temperatures given in Table 6.1) to generate the diluted sample gas. Once generated, the sample gases can be delivered to the detector for detection.

	NO_2	NH_3	CH_3COOH
Emission Rate [ng/min]	2600	490	890
Molecular Weight [g]	46.0055	17.0304	60.0524
Flow Rate [ml/min]	100	100	100
Temperature [°C]	35	35	70 (110)

Table 6.1 The specific constants for the permeation tube of sample gases. The number in brackets for temperature specifies the maximum applied temperature recommended by the manufacture.

All three gases (NO_2, NH_3 and CH_3COOH), were previously tested by the field ionization process [26] at 1000 ppm. In this case, we obtained permeation tubes that will take down the concentration to even lower a level.

11. The manufacturer suggested the constants 0.03 for high emission tubes and 0.034 for standard emission tubes.

The measuring instruments consist of a magnetically actuated *3-way valve* and a semiconductor parameter analyzer. These will be described next:

6•1•3•2 Magnetic Actuated 3-Way Valve

The gas generation and delivery system is connected through a 1/4" teflon tube to the input manifold (see Figure 5.37) of the micromachined field ionization detector as shown in Figure 6.1. Normally (prior to injection of sample gas), the *3-way valve* is configured in a position which vents out the sample gas generated in the U-tube. When the *3-way valve* is in this position, nitrogen carrier gas is flowing through the detector instead, to purge it. When injection is desired, the control switch which is connected to the *3-way valve* is activated to toggle the valve to its second position. In this second position, the sample generated gas is directed to the detector.

6•1•3•3 Semiconductor Parameter Analyzer[12]

A parameter analyzer was used to perform the measurements to record the current versus the time signal generated. The measurement equipment requirements for the field ionization detector involves current measurement in the picoampere range while the applied voltage required is in the 5-40 V range. The semiconductor parameter analyzers (HP 4155 A model) is well suited to fulfill both these objectives. This model allows measurement intervals as short as 4 ms to as long as 10 s And it also allows 10000 data points to be stored for a single measurement cycle. For purpose of our experiments we chose the 4 ms interval, as it reduces noise to a large degree.

---

12. Model HP 4155 A, Hewlett Packard, Palo Alto, CA, USA.

6•2 Steady-State Response of the Detector

Since the response of the micromachined field ionization detector to sample gas concentration and applied voltage is crucial to final design of the detector in the micromachined gas chromatography system, detector is characterized to find its dependency to these parameters independently. To this effect, a series of experiments were performed where the applied voltage and the sample gas concentration were varied, the latter by adjusting the operating temperature of gas generation and delivery system and evaluate the detector response to these changes.

6•2•1 Gas Generation/Delivery System Concentration

According to equations (6.1) and (6.2), the concentration of sample gas generated can be controlled by two parameters namely the flow rate of the carrier gas and the temperature at which the permeation tube is maintained. In this respect, this experiment has been performed so that the concentration of the gas generated can be controlled reproducibly. Temperature was selected as the controlling parameter, even though the temperature is more difficult and tedious to control than is the flow. Flow rate measurement turned out to be less accurate than temperature measurement simply because of inaccuracy in reading the value off the flowmeter. Hence, the detector's response to concentration was investigated by temperature control.

The experiment with the effect of permeation tube's temperature involves setting the flow meter *F1* (see Figure 6.1) at a constant value and maintaining it at that value at all times. For this purpose, the flowrate is chosen to be at 100 ml/min, simply because this is the minimum value given to us by the manufacture for generating the maximum

concentration of the sample gas. Having selected the flow rate, then the permeation tube's temperature of a sample gas was varied for five temperatures; 90 °, 95 °, 100 °, 105 °C and 110 °C. Some preliminary testing was performed to evaluate the detector's response to generate sample gas. However, it was established that the gas concentration, generated below 90 °C at 100ml/min is not measurable by the detector due to low level of signal-to-noise ratio. The 110 °C temperature is the maximum temperature the CH_3COOH permeation tube can tolerate. Above this temperature, the gas generation rate in the permeation tube is much faster than the permeation rate from the tube to its surroundings. This usually results in an explosion of the teflon permeation tube if continued for long.

6•2•1•1 Concentration Test Procedure

In the concentration test procedure, the temperature of the permeation tube is used to adjusted the level of the concentration of the sample gas. After each run, the sample gas concentration was varied by adjusting the temperature and allowing the flow to stabilize the permeation rate. This usually takes approximately 10 hours (from the moment the temperature is adjusted to the desirable temperature value) to stabilize. Prior to injecting the sample gas by the *3-way valve* (see Figure 6.1), the detector is purged at ambient temperature with nitrogen gas for approximately 60 min. The flow regulator *C* is then shut off to stop the nitrogen flow to the detector. With the flow regulator D and E open, the *3-way valve* is switched to its second position to allow the flow of sample gas to the detector. Approximately five minutes prior to activation of the *3-way valve* to inject the sample gas, the parameter analyzer is switched on to record the detector's response. In this particular experiment CH_3COOH is used as the sample gas. With the use of (6.1) to (6.2), the concentration of the sample gas is increased from 10 to 60 ppm, by increasing the

temperature from 90 °C to 110°C (corresponding to the minimum reproducible flow rate of approximately 100 ml/min).

6•2•1•2 CH_3COOH Response

The procedure was implemented at each permeation tube's temperature value in order to generate five different concentration levels of the sample gas CH_3COOH. The detector signal was then processed according to the procedure described in Appendix B (where the response is defined as the magnitude of the amplitude of the fitting function, and the error is calculated from the standard deviation of the fitted and the measured signal). The results are summarized in Figure 6.10. The actual data collected is presented in Figures 6.5 to 6.9.

For CH_3COOH, there is an approximate linear relationship (given by (6.3)) between the injected concentration and the field ionization detector's response. As expected, when the temperature of the permeation tube is increased, the rate of emission from the permeation tube increases according to equation (6.2). This results in an increase in the signal picked up by the detector. The error in the sample gas concentration is $\pm 15\%$ as specified by the manufacturer for each permeation tube.

$$D_{response} = -4.8929 + 0.81853 \bullet C \qquad (6.3)$$

where $D_{response}$ is the detector response in pA and C is the sample gas concentration in ppm. The minimum detectable level is about 14 ppm.

6•2•1•3 NO_2 and NH_3 Response

In the case of the other two sample gases, NO_2 and NH_3, the experiment confirmed that the field ionization detector does not show any response to these gases at their maximum generated concentration level (14 ppm and 7 ppm respectively). The temperature of their respective tubes were raised 35 °C to be able to generate these levels of concentration. The tubes' temperature could not be raised any further to increase the concentration level because further increase in the temperature could results in damage to the tubes. The purpose of performing this experiment is to verify Madou *et al.* [45] also reported that these two gases can be detected by field ionization. They showed that the gases can only be detected at the presence of water vapor. This is discussed later in this chapter.

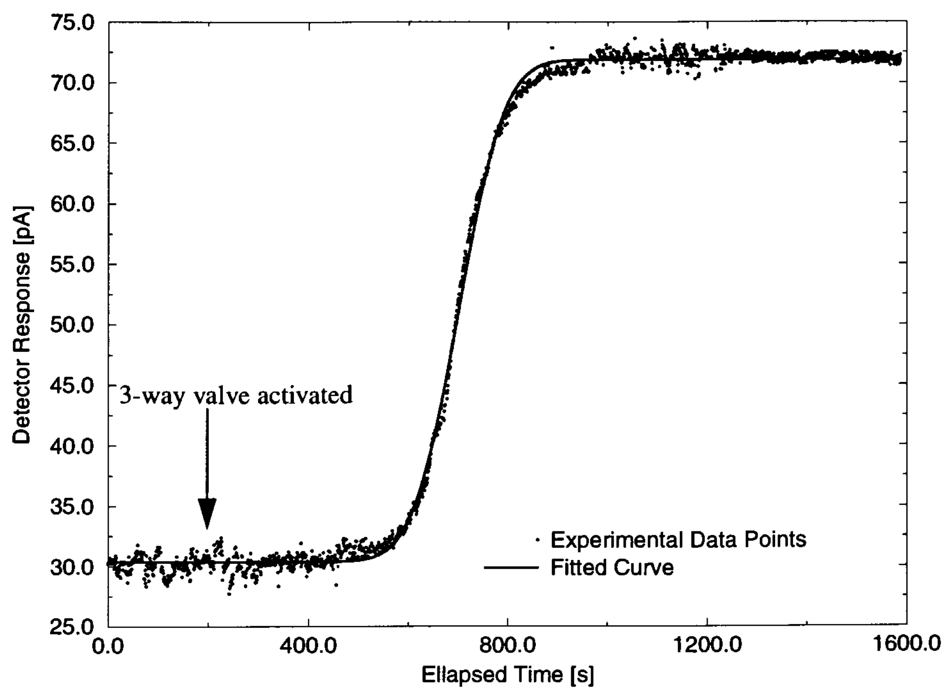

Figure 6.5 Detector performance for acetic acid vapor at a concentration of 57 ppm.

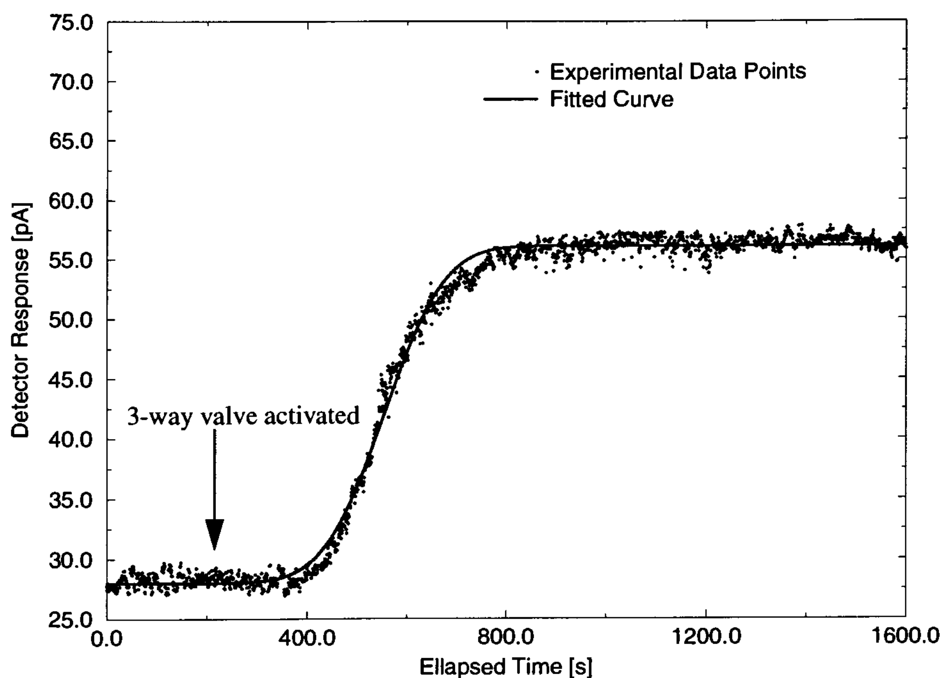

Figure 6.6 Detector performance for acetic acid vapor at a concentration of 41 ppm.

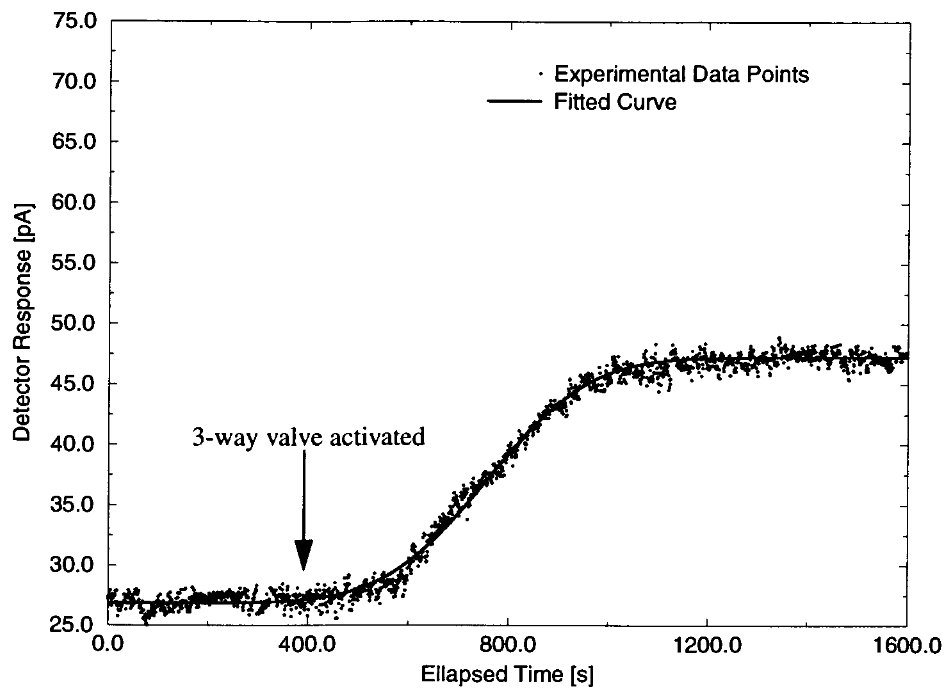

Figure 6.7 Detector performance for acetic acid vapor at concentration of 29 ppm.

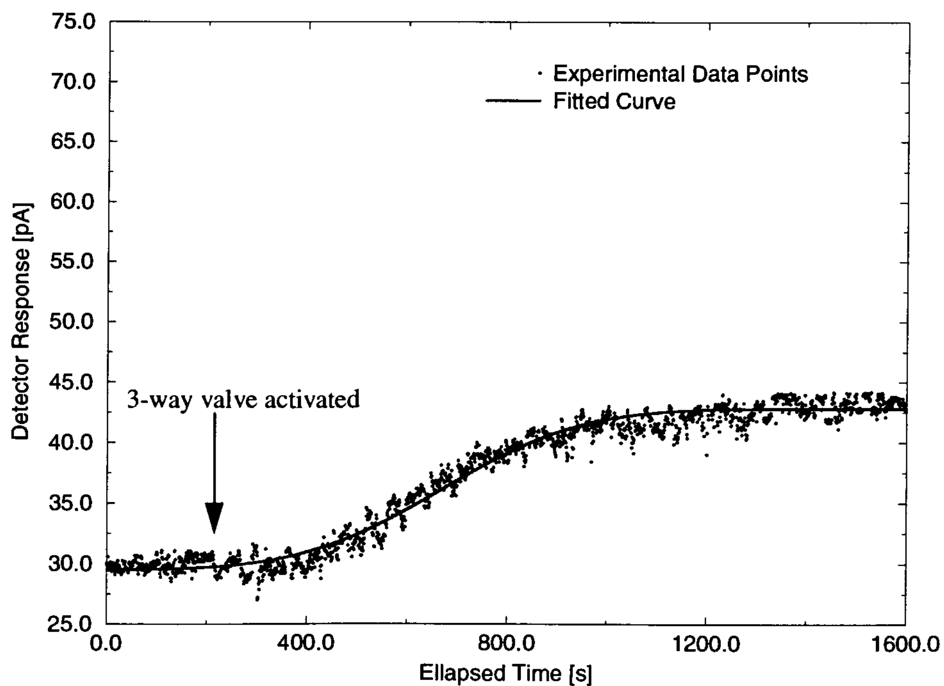

Figure 6.8 Detector performance for acetic acid vapor at a concentration of 20 ppm.

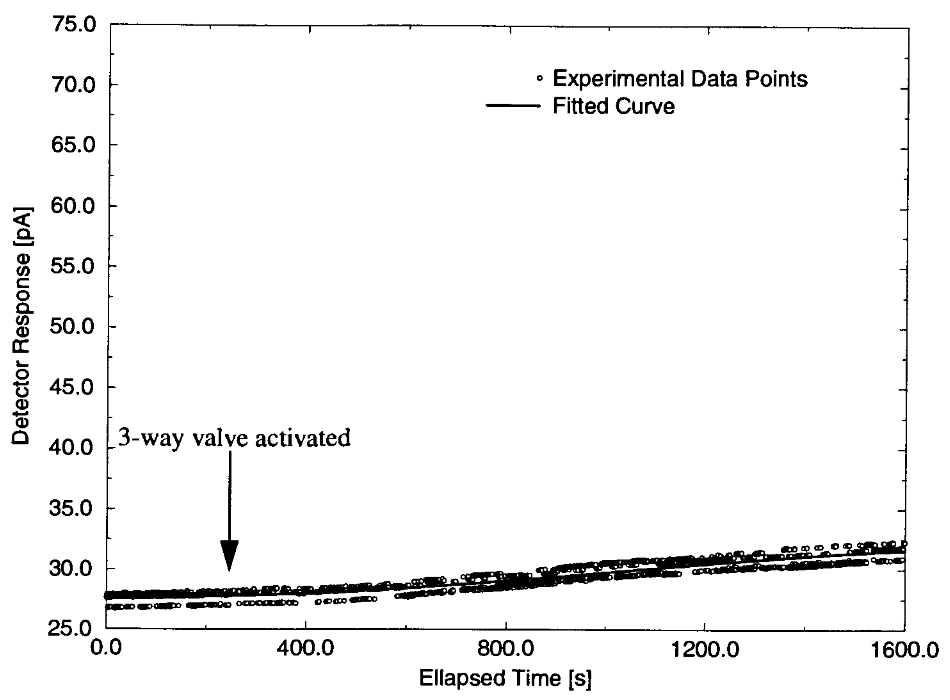

Figure 6.9 Detector performance for acetic acid vapor at concentration of 14 ppm.

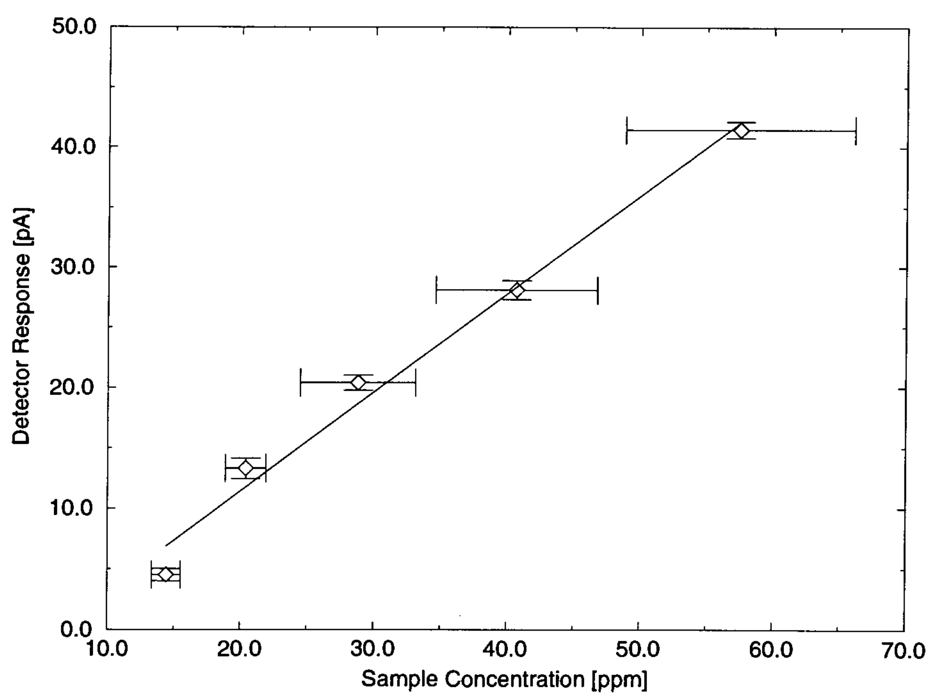

Figure 6.10 Dependence of the field ionization detector on acetic acid vapor concentration with 5 volts applied to electrodes.

6•2•2 Applied Voltage Dependence

In this experiment, as in the previous one, the NO_2, NH_3 and CH_3COOH were selected as the sample gas to characterize the detector's response with respect to the applied voltage as the variable. The applied voltage varied for four different values: 5, 20, 30 and 40, with 40 V being the maximum value that can be generated by the SPA (without a high voltage protection circuit) to be applied to the detector. The concentration of the sample gas has maintained at a constant value at all time. In the case of CH_3COOH, the tube temperature was maintained at 105 °C to have a measurable concentration level, whereas for NO_2 and NH_3 the temperatures of the tubes were maintained at 50 °C to set the maximum concentration level.

6•2•2•1 Test Procedure

The test procedure is very similar to the one used in the prior experiment with concentration characterization process (Section 6•2•1•1). In this experiment, the carrier gas flow to maintained at a constant value of 100 ml/min. After each run, the applied voltage to the tip was varied and then the flow was allowed to stabilize over the permeation tube. This usually takes approximately 10 hours (from the moment the temperature is adjusted to reach the desirable temperature value) to stabilize. Prior to injecting the sample gas by the *3-way valve* (see Figure 6.1), the detector is purged at ambient temperature with nitrogen gas for approximately 60 min. The flow regulator *C* is then shut off to stop the nitrogen flow to detector. With the flow regulator D and E open, *3-way valve* is switched to its second position to allow the flow of sample gas to the detector. A few minutes prior to activation of the *3-way valve* to inject the sample gas, the SPA is switched on to record the detector's response. The SPA records the data for approximately

half an hour, before its memory overflows.

6•2•2•2 CH_3COOH Response

The procedure described was implemented at each applied voltage to in order to monitor the response of the detector for the sample gas CH_3COOH. The detector signal was then processed according to the procedure described in Appendix B (where the response is defined as the magnitude of the amplitude of fitting function, and the error is calculated from the standard deviation of the fitted and the measured signal). The results are summarized in Figure 6.14. The actual data collected are presented in Figures 6.11 and 6.12.

As can be seen from the graph shown in Figure 6.14, there is a linear dependency between the detector response and the applied voltage on a linear-log plot. This indicates that the actual relationship between detector response and applied voltage is exponential. This observation agrees with the equation (3.12) derived in Chapter 3. In addition, for comparison, the experimental data from Madou *et al.* [45] obtained with formic acid as the sample gas is plotted on same graph. Their results similarly shows an exponential relationship. However, there are some differences which will be pointed out here and discussed in this section.

Firstly, the gradient of the two straight lines are different. As was point out in Chapter 3, this is related to factor n in equation (3.12). This is related to the conductive material used for the tip. The tip in this experiment is made of gold whereas the tip for Madou *et al.* [45] is made of molybdenum coated with a very thin gold layer (see Figure 5.1). Since Madou's tip is a of multi-conductive material, the deviation of the two gradients can be associated with the tip's material.

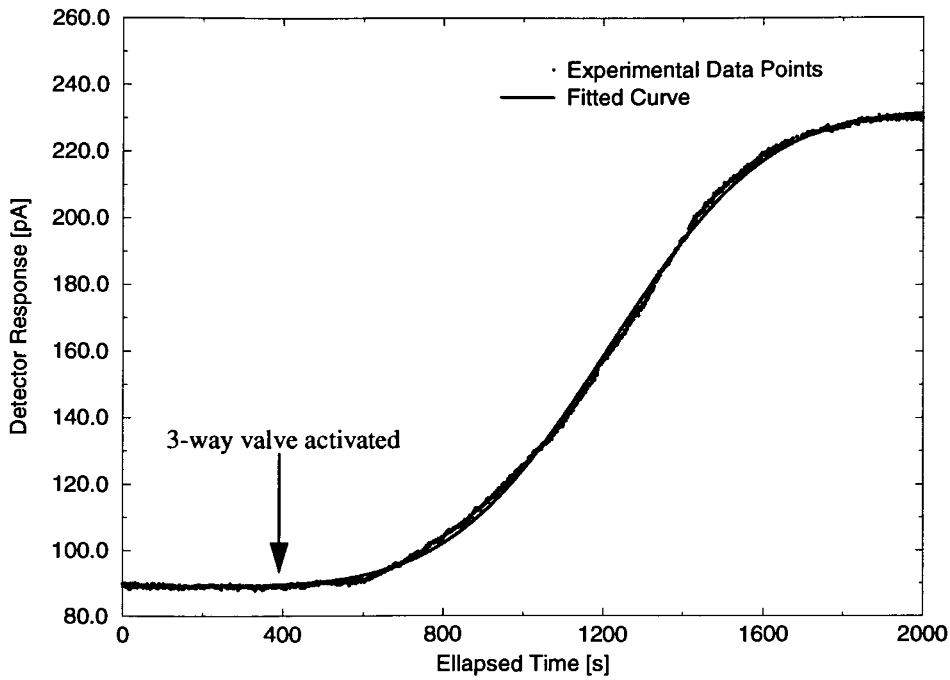

Figure 6.11 Detector performance for the acetic acid vapor concentration of 57 ppm at 40V.

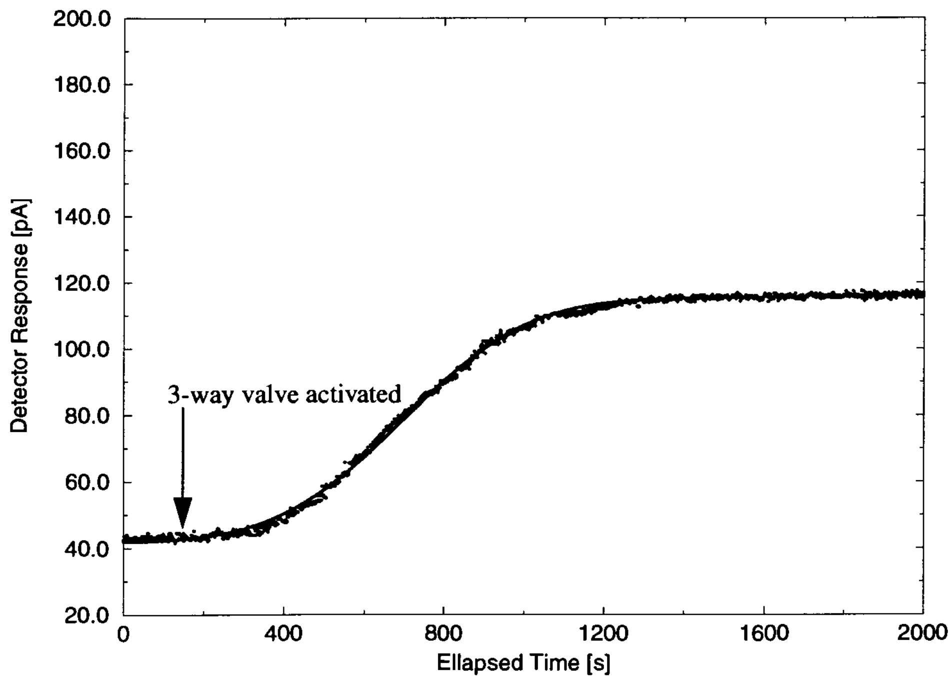

Figure 6.12 Detector performance for the acetic acid vapor concentration of 57 ppm at 30V.

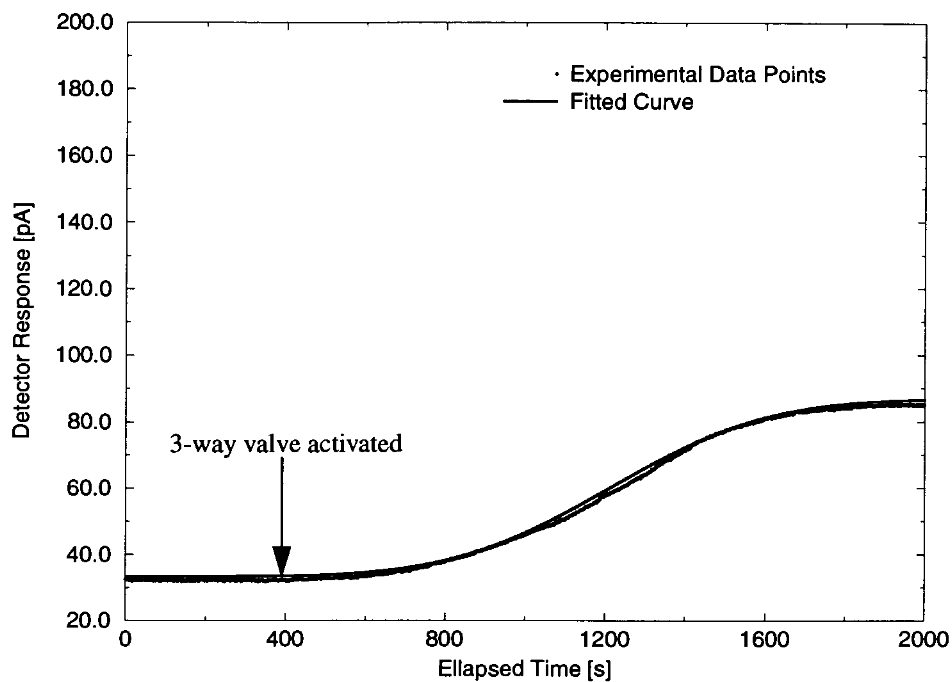

Figure 6.12 Detector performance for the acetic acid vapor concentration of 57 ppm at 20V.

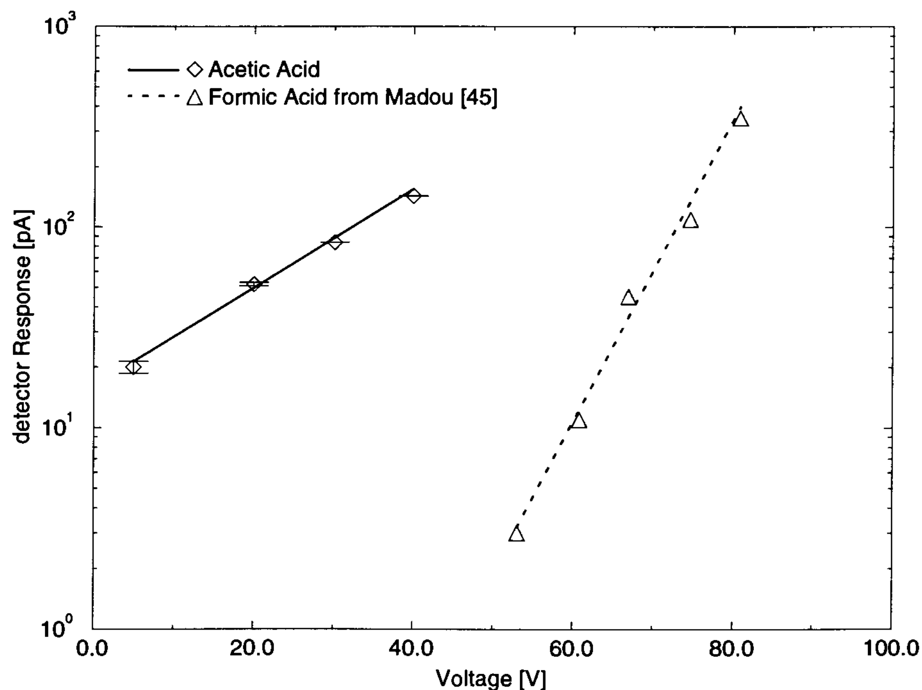

Figure 6.14 Dependence of the field ionization detector for acetic acid vapor with applied voltage as the variable.

The second obvious difference between the two plots is the magnitude of the current in the region between 5 to 40 volts. Although the results are for two different gases, nevertheless, it can be seen from the graph that there is a measurable current from tips fabricated with the technology described in this thesis than the one used by Madou *et al.* [45]. This may indicate that the electric field created on the tips fabricated with our technology is much greater than the field produced by Madou's tip. This higher intensity of the electric field increases the probability of ionization of the sample gas molecule at low applied voltages. This is specially interesting because formic acid has higher ionization coefficient (k_b=1.86 x 10^{-4}) than acetic acid (k_b=1.75 x 10^{-5})(see Table 6.3).

6•2•2•3 NO_2 and NH_3 Response

In the case of these two gases, the detector does not show any responses even at higher applied voltage (up to 40 V). The NO_2 result agrees with that of Madou *et al.* [45] whose preliminary result also showed no response to NO_2. This is discussed further in the next section.

6•3 Discussion of the Results

Given the total number of chemical compounds known, it is a most formidable task to characterize any gas detector to every single chemical compounds. Therefore, in this discussion, it is intended to make an argument based on the work performed in this thesis and the one performed by Madou *et al.* [45]. This argument is then used to propose a model which outlines the class of chemical compounds that can/can not be detected with a field ionization detector.

Table 6.2 shows the gases Madou *et al.* [45] used to test their detectability to a field

ionization detector. As it can be seen from this table and the results performed in this thesis, gases with acidic properties are more likely to be detected by a field ionization detector. In Addition, inert and solvent gases appeare to be undetected. This is believed to

Inactive Gases	Active Gases
O_2	HCOOH (Formic Acid)
N_2	CH_3COOH (Acetic Acid)
Ar	NO_2+H_2O
NO_2	$(C_2H_5)_2NH_2$ (Diethylamine) + H_2O
CH_3COCH_3 (Acetone)	NH_4OH (Ammonia Hydroxide)
H_2O	-
$(CH_3)_2CHOH$ (Isopropyl Alcohol)	-

Table 6.2 Inactive and active atmospheric impurities [45].

be due to fact that these gases may require a much higher electric field intensity to be ionized. For instance, CH_3COOH, which is considered to be a weak acid, has an ionization coefficient of 1.75 x 10^{-5}, and could be easily detected in the field ionization detector (with applied voltage of 5 volts), whereas NO_2 was not detected even at 40 volts. However, Madou *et al.* [45] showed NO_2 in the presence of water vapor can be detected. This is believed to be associated with the fact that addition of water vapor to NO_2 during the sample gas generation process produces nitric acid HNO_3 vapor, which is a strong acid with an ionization coefficient of 27.79. This high ionization coefficient helps its detection. However, ammonia NH_3, one of the sample gases tested in this thesis, produced no measurable current. The low concentration of NH_3 is mainly believed to be the reason for its unsuccessful detection. As NH_3 has an ionization coefficient of

$1.77x10^{-5}$, which is comparable to that of CH_3COOH. In addition, Madou *et al.* [45] experimented with NH_4OH (at 1000 ppm) which is a solution of $NH_3 + H_2O$ and reported on its detection by field ionization detectors. This does not indicate that addition of water to NH_3 vapor had any effects on its detection, but it merely indicates a high concentration of NH_4OH can be detected.

By looking at these results we can see that the class of gases that tend to be detected by field ionization detectors are the gases with high ionization coefficient. In addition to this, due to variation of ionization coefficients of different gases, there will be a need for different value of applied voltage. By looking at Table 6.3, it can be argued, since CH_3COOH was detected in the field ionization detector with an applied voltage of 5 volt or more, then all gases with a higher ionization coefficient (see Table 6.3), must be detectable by field ionization.

Acid	Formula	(Ionization Coff.) K_a
nitric acid	HNO_3	27.79
dichloroacetic acid	$CHCl_2COOH$	5.68×10^{-2}
chloroacetic acid	$CH_2ClCOOH$	1.36×10^{-3}
hydrofluoric acid	HF	6.94×10^{-4}
nitrous acid	HNO_2	5.98×10^{-4}
cyanic acid	$HOCN$	3.54×10^{-4}
formic acid	$HCOOH$	1.86×10^{-4}
lactic acid	$H_3CCHOHCOOH$	1.37×10^{-4}
benzoic acid	C_6H_5COOH	6.31×10^{-5}
hydrazoic acid	HN_3	2.37×10^{-5}
Ammonia	NH_3	1.77×10^{-5}
Acetic Acid	CH_3COOH	1.75×10^{-5}
hydrocyanic acid	HCN	5.85×10^{-10}
Ammonium	NH_4	5.60×10^{-10}
phenol	C_6H_5OH	1.08×10^{-10}
dimethylammonium	$(H_3C)_2NH_2$	1.82×10^{-11}
ethanol	CH_3CH_2OH	1.31×10^{-14}
water	H_2O	1.01×10^{-14}

Table 6.3 Selected values of aqueous and their ionization constants at 25°C.

6•4 Summary

In this chapter, the results of the micromachined field ionization detector characterization is presented and discussed. The initial effort was to set up the gas generation and delivery system to perform the steady-state characterization. This was accomplished by using permeation tubes of the sample gases.

Overall, the detector characterization is considered successful, and the performance information gained can be used as the basis for establishing the applied voltage and concentration operational parameters used in future micromachined gas chromatography systems.

Chapter 7

Conclusions and Recommendations for Future Research

7•1 Conclusions

This research has demonstrated the use of single-crystal silicon bulk micromachining to implement a gas detector based upon the field ionization process. These type of detectors have been demonstrated to detect gases that have large ionization coefficient such as CH_3COOH. Additionally, valuable information concerning the field ionization properties has been revealed through the detector characterization stage. The major contributions ascertained from this research can be discussed with respect to two areas: novel micromachining techniques for manufacturing micro-gas detectors and gas sensing by the field ionization process.

In the micromachining area, two novel techniques have been proposed for fabrication of field ionization tips, of which one of them has been developed here. The key features of these two fabrication techniques relative to previously reported work include:

(a) manufacturing cost. Most of the state-of-the-art techniques for the formation of the sharp tip use expensive non-standard processes such as CVD, RIE and rotating source e-beam evaporators. Most importantly, they require masks with the resolution in the order of micrometers or sub-micrometers to position the tip close to a counter electrode (about a micrometer). These requirements considerably increase the manufacturing costs. The techniques described in this thesis provide a significant reduction in the cost achieved by the use of only standard fabrication processes such as oxidation, sputtering, wet silicon

anisotropic etching, an electroplating process for thick metal deposition and a sub-millimeter resolution mask to produce ionization tips with a sub-micrometer gap between the tip and cathode.

(b) As the tips in this technique are created at the last stage, the process has the potential to maintain a high yield. The other techniques tend to create the tips at the first few steps and as a result, some of them get destroyed by the end of the process.

(c) Finally, since the technology is based on bulk micromachining, it can easily be integrated with the micromachined gas chromatography system designed by Terry [2] or Reston [21]. This will in turn improve the yield and manufacturing cost of micromachined gas chromatography systems dramatically.

In the chemical sensing area, the primary accomplishment was to undertake an experimental study to test and characterize the proposed detector. The research results show that: (a) The class of gases that can be detected using the proposed detector encompasses gases with large ionization coefficients ($>1.75 \times 10^{-5}$ for acetic acid). Gases with a small ionization coefficient, for example nitrogen dioxide could not be detected within 0 to 14ppm. (b) The minimum detectable concentration level in the case of acetic acid was 14 ppm. (c) The minimum applied voltage required to detect acetic acid at 14 ppm was 5 V.

7•2 Summary of Contributions

The contributions to research described in this thesis can be summarized as:

- an affordable technique for electrodeposition of thick metallic film has been developed

- a simple economical process for fabrication of the field ionization tips with a low-resolution mask has been proposed and tried experimentally with good results

- micromachining submicrometer gaps between two electrodes using a low-resolution lithography mask has been achieved

- functionality of a field ionization detector as a GC systems end detector has been confirmed

- manufacturability of the proposed detector for future micromachined gas chromatography system with standard fabrication processes has been proven experimentally

7•3 Further Research

For further research, it is recommended for the detector fabricated in this thesis. It is required to test more gases. The next step would be to integrate the detector with the proposed micromachined gas chromatography column for an ultimate miniaturized gas chromatography system and test its functionality.

Appendix A

Microfabrication Processes

For the microfabrication of micromachined field ionization detector, the following microfabrication processes were used in addition to those discussed in Chapter 4.

A•1 RCA Cleaning

target: prepare wafers for oxidation/diffusion
equipment: wet sinks
recipe highlights:

A.1.1 RCA SC-1 Clean (Organics)
temperature: 80±5°C,
time: 10 minutes,
solution: H_2O(1000mL)+NH_4OH(200mL)+H_2O_2(200mL) in ratio 5:1:1,

A.1.2 DI Water Rinse
time: 3 minutes in running DI water,

A.1.3 HF Dip (Native Oxide Strip)
temperature: room temperature,
time: 30 seconds,
solution: H_2O(1500ml)+HF(150ml) in ratio 10:1,

A.1.4 DI Water Rinse
time: 3 minutes in running DI water,

A.1.5 RCA SC-2 Clean (Metals)
temperature: 80±5°C,
time: 10 minutes,
solution: H_2O(1050ml)+HCL(175ml)+H_2O_2(175ml) in ratio 6:1:1,

A.1.6 DI Water Rinse
time:5 minutes in running DI water,

A.1.7 Spin Dry
Spin at maximum RPM until dry,

A•2 Thermal Oxidation

target: oxidize wafer
equipment: oxidation furnace
recipe highlights:

A.2.1 Prepare Furnace (Tube 1)
N_2 flow 4 scfh. O_2 at 0 scfh,
Ramp temperature to 800°C,
Fill bubbler with DI water,
Start water heater and tape heaters,

A.2.2 Load Wafers into Boat
Use correct boat and white elephant
Use wafer forceps

A.2.3 Push Boat into Furnace
temperature: 800°C,
Use gloves and quartz rod. Max push rate 4in/min,

A.2.4 Ramp Furnace Up
Set operation temperature to desirable,

A.2.5 Oxidation
Furnace at the desired temperature,
N_2 at 4 scfh and O_2 at about 0.5 scfh for good steam action in bubbler,

A.2.6 Ramp Furnace Down
Set operation temperature to 400°C,

A.2.7 Pull Boat and Unload
Pull out (<4 in/min) when all zones < 800°C,

A.2.8 Return Furnace to Idle
Bubbler and tapes off. O_2 off and N_2 at 0.5-1.0 scfh,
Close bottle valve,

A•3 Boron Diffusion

target: boron diffusion
equipment: diffusion furnace
recipe highlights:

A.3.1 Prepare Furnace (Tube 2)
Set N_2 at 10 scfh and O_2 at 0 scfh,
Ramp temperature to 800°C,

A.3.2 Load Wafers into Boat
Two wafers/source, in slot next to source, facing it,
Place dummy wafers in unused slots,

A.3.3 Push Boat into Furnace
N_2 at 5 scfh and O_2 at 5 scfh,
Temperature at 800°C, push < 4in/min,

A.3.4 Ramp Furnace to 900°C
N_2 at 10 scfh and O_2 at 0.5 scfh,

A.3.5 Stabilization at 900°C
N_2 at 5 scfh and O_2 at 5 scfh,
Time=10min,

A.3.6 Ramp to Operating Temperature
Set N_2 at 10 scfh and O_2 at 0 scfh,
A.3.7 Diffusion
N_2 at 10 scfh and O_2 at 0 scfh,
Time=10min Temperature=900°C,
A.3.8 Ramp Temperature Down
N_2 at 10 scfh,
Set temperature to 400°C,
A.3.9 Pull Boat and Unload
Pull out (<4 in/min) when all zones < 800°C,
A.3.10 Return Furnace to Idle
O_2 off and N2 at 0.5-1.0 scfh,

A•4 Oxide Etch

target: etch oxide
equipment: wet sinks
recipe highlights:

A.4.1 Oxide Etch
Transene buffered oxide etchant,
Slight agitation,
Room temperature,
Etch rate=0.1 micrometer/minute,
A.4.2 DI Water Rinse
10 minutes rinse in running DI water,
A.4.3 Spin Dry
Spin at max. RPM until dry,
A.4.4 Inspect and Measure
Use microscope to ensure etch is complete,
A.4.5 Photoresist Strip
Soak in room temperature in acetone,
Time=5 minutes,
A.4.6 DI Water Rinse
3 minutes in running DI water,
A.4.7 Spin Dry
Spin at max. RPM until dry,
A.4.8 Inspect
Use microscope to look for remnant of photoresist,

A•5 Photolithography Process

target: patterning photoresist
equipment: wet sinks

recipe highlights:

A.5.1 Prebake
Temperature=100°C, time=25 minutes,
Cool to room temperature before spinning photoresist,

A.5.2 Spin Photoresist
Shipley SPR2,
Flood surface, spin at 4000 rpm for 30 seconds,

A.5.3 Soft Bake
Temperature=100°C, time=25 minutes,

A.5.4 Align and UV Exposure
Time=30 seconds,

A.5.5 Develop
MF319, undiluted,
Room temperature with slight agitation,
About 60 seconds,

A.5.6 Rinse
Running DI water for 3 minutes,

A.5.7 Spin Dry
Spin at max. RPM until dry,

A.5.8 Inspect
Under microscope,

A.5.9 Hard Bake
Temperature=120°C, time=25 minutes,

A.5.10 Inspect
Under microscope,

A•6 Sputtering

target: sputter deposition of metal
equipment: DC sputtering machine
recipe highlights:

A.6.1 Weigh Substrate (optional)
For thickness calculation,

A.6.2 Load Substrate
Secure to holders in chamber,

A.6.3 Rough Pump
Evacuate chamber to 50 mTorr,

A.6.4 High Vacuum Pump
T0 3e-6 torr or lower,

A.6.5 Sputter Clean Source
500 W*min at 0.2A in current mode at 3 mTorr Ar pressure,

A.6.6 Sputter Deposit Aluminum

About 8000 W8min at 0.2A at 3 mTorr Ar pressure depending on thickness

A.6.7 Shut Down Process

Stop process (6), close high vacuum valve. bleed chamber to atmosphere,

A.6.8 Remove Substrates

Open chamber. Remove substrates carefully,

A.6.9 Shut Down System

Turn down per procedures,

A.6.10 Inspect

Visual, weight, thickness, adhesion,

A•7 EDP Etching

target: anisotropic etching of silicon wafer
equipment: wet sinks
recipe highlights:

A.7.1 Set Up Apparatus

Place reactor on stirrer/hot plate,
Run cooling water line,

A.7.2 Fill Apparatus

Fill reactor,
Usually use Transene PSE 300 (water, ethylenediamine, pyrocatechol),

A.7.3 Prepare Apparatus

Insert stir bar,
Start cooling water,
Start heating to 95°C,

A.7.4 Prepare Sample

Remove native SiO_2 with brief etch in 2% HF solution,
Rinse 3 minutes in running DI water,

A.7.5 Place Sample in Apparatus

With etchant at temperature, remove sample from DI rinse and place it while still wet into reactor,

A.7.6 Etch

Place sample in etchant,
Start timing immediately,
Etch rate at 95°C is about 0.8 micrometer/minutes,

A•8 TMAH Etching

target: anisotropic etching of silicon wafer
equipment: wet sinks
recipe highlights:

A.8.1 Set Up Apparatus

Place reactor on stirrer/hot plate,
Run cooling water line,

A.8.2 Fill Apparatus
Fill reactor,
Usually use water,

A.8.3 Prepare Apparatus
Insert stir bar,
Start cooling water,
Start heating to 80°C,

A.8.4 Prepare Sample
Remove native SiO_2 with brief etch in 2% HF solution,
Rinse 3 minutes in running DI water,

A.8.5 Place Sample in Apparatus
With etchant at temperature, remove sample from DI rinse and place it while still wet into reactor,

A.8.6 Etch
Place sample in etchant,
Start timing immediately,
Etch rate at 80°C is about 0.8 micrometer/minutes,

A•9 Metal Etching

target: etching metal with Aluminum as the example
equipment: wet sinks
recipe highlights:

A.9.1 Aluminum Etch
Transene Aluminum etchant,
Temperature= 50°C with a etch rate 100A/second,

A.9.2 DI Water Rinse
5 minutes in running DI water,

A.9.3 Dry
Blow dry N_2,

A.9.4 Inspect and Measure
Inspect under microscope,

A.9.5 Photoresist Strip
Soak at room temperature in acetone,
Time=5 minutes,

A.9.6 DI Water Rinse
minutes in running DI water,

A.9.7 Dry
Spin at max. RPM until dry,

A.9.8 Inspect
Inspect under microscope,

Appendix B

Non-Linear Least-Square Fit

This appendix deals with description of the non-linear least-squares curve fitting MATLAB[1] routines used to fit the experimental data obtained in this research. This method of fitting a function to experimental data was used by Reston [24] to calculate the percentage error in his experimental data generated by his micromachined gas detector. MATLAB's source code will be described first. The description of the individual commands can be looked up in the MATLAB manuals [114] and [115].

B•1 Fitting Function

The micromachined field ionization gas detector's sample gas exposure evaluation requires determining a mathematical function to use in the curve fitting. It is assumed that any of the gas peaks produced by the sample valve would be Gaussian in nature (due to the longitudinal diffusion of the sample as it propagates through the column and interconnect tubing). Furthermore, the micromachined field ionization gas detector is observed to behave as an integrating detector just like most gas detectors, e.g. chemiresistor, (its response to injected pulses of the sample gas would gradually change from its baseline response and plateau, remaining stable for approximately one hour. Thus, the response to the sample gas could potentially be the integral of a gaussian-shaped gas concentration peak.

---

1. The MathWorks, Inc., 24 Prime Park Way, Natick, MA 01760, USA (version 4.2c).

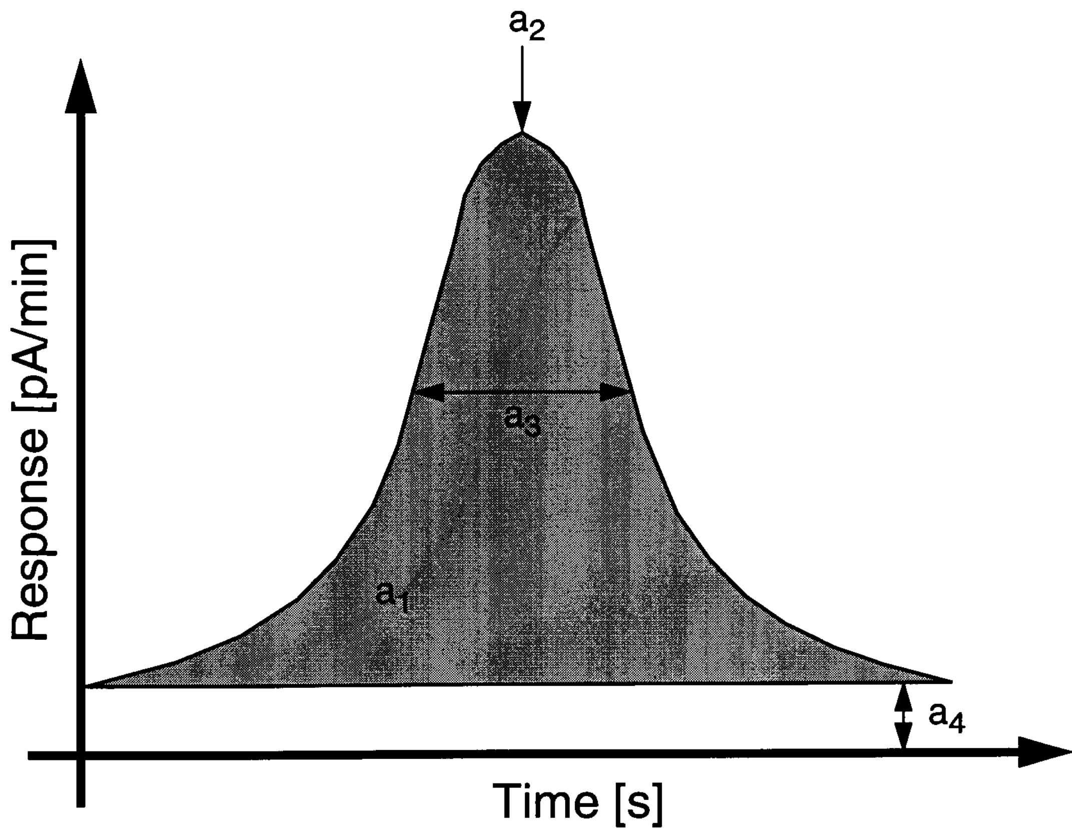

Figure B.1 A gaussian peak.

B•1•1 Response Function

If a_1 is the area under a gaussian peak, a_2 the location of the center of the peak, and a_3 the width (standard deviation) of the peak, the gaussian peak's behavior with respect to time (see Figure B.1), $f(t)$, can be defined by the following equation:

$$f(t) = \frac{a_1}{a_3\sqrt{2\pi}}\exp\left[\frac{-(t-a_2)^2}{2a_3}^2\right] \quad \text{(C.1)}$$

Integrating from $t = 0$ to some arbitrary time, τ, yields:

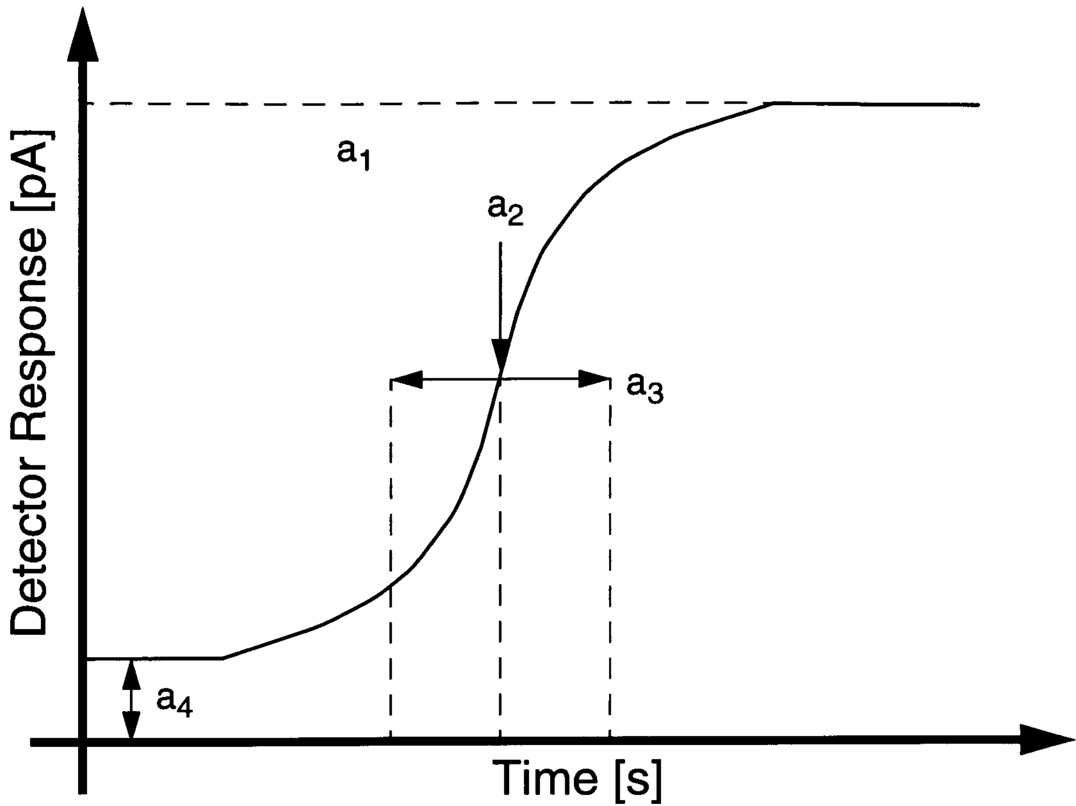

Figure B.2 Erf function response of the detector.

$$\int_0^{\tau} f(t)dt \approx a_4 + \frac{a_1}{2}\left[erf\left(\frac{\tau - a_2}{a_3\sqrt{2}}\right) + 1\right] \tag{C.2}$$

for $(a_2/a_3) > 0$. This function is depicted in Figure B.2. Hence, relative to the prior discussion concerning the micromachined field ionization gas detector, the right side of (C.2) is the basis for the fitting for the micromachined field ionization gas detector's data.

The equation (C.2) is implemented by MATALB source code and is described in the next section

B•2 MATLAB Source Code

The main MATLAB's source codes are illustrated below. MATLAB has a command called `leastsq` which starts at the matrix X_0 and finds a minimum to the sum of squares of the functions described in the command. The function is usually an M-file which returns a matrix of objective functions.

```
% Define the data sets that you are trying to fit the desired
% function to.
load <SPA data file name>.txt -ascii
save temp -ascii
load temp -ascii
```

These code instructions will enable MATLAB to download the collimated data points, generated by the semiconductor parameter analyzer, for further processing.

```
X=temp(:,2);
Y=temp(:,3);
```

The previous lines will assign the contents of column 2 to vector X and column 3 to vector Y. This is because the data file generated by the SPA contains three columns.

```
% Initialize the coefficients of the function.
X0=[128e-12 1300 2 1.1283e-10]';
```

These are the initial values of the fitting coefficients in (C.2). They are approximate values and are worked out from the individual graphs. However, as the program progress these will be re-calculated for improvements. The values mentioned above correspond to graph given in Chapter 6.

```
% Calculate the new coefficients using leastsq.
x=leastsq('fit_simp',X0,[],[],X,Y);
```

The calculation of the initial coefficients of the function (C.2) is performed by the subroutine called `fit_simp`. This subroutine is stored in a separate file and is called to

perform the task. The subroutine appears below.

```
function diff = fit_simp(x,X,Y)
% This function is called by leastsq.
% x is a vector which contains the coefficients of the
% equation.  X and Y are the option data sets that were
% passed to leastsq.

a1=x(1);
a2=x(2);
a3=x(3);
a4=x(4);
diff = a4+(a1./2).*(erf((X-a2)./(a3.*sqrt(2)))+1)-Y;
```

The experimental and the fitted function are plotted for comparison of the two with the code below.

```
% Plot the original and experimental data.
Y_new = x(4)+(x(1)./2).*(erf((X-x(2))./(x(3).*sqrt(2)))+1);
plot(X,Y,'.r',X,Y_new,'b')
```

For the purpose of quantifying the noise level (to incorporate error bars in the evaluation graphs), the standard deviation between the experimental data and fitted function was determined by subtracting the fitting function from the experimental data. The new set of data is stored in a column-oriented matrix. The standard deviation is then calculated using the code in the lines below.

```
std_data=Y-Y_new;
s_dev=std(std_data);
```

The following script will enable the experimental data as well as the fitted data to be stored in the file.

```
z=[X,Y_new];
c=[X,Y];
save <name of the fitted file>.txt   z -ascii
save <name of the measured file>.txt c -ascii
end
```

References

[1] N. Yamazoe, N. Miura, "Environmental gas sensing", *sensors and actuators*, vol. B20, pp. 95-102, 1994.

[2] S. C. Terry, J. H. Jerman and J. B. Angell, "A gas chromatographic air analyzer fabricated on silicon wafer", *IEEE-ED*, vol. 26, no. 12, 1979.

[3] W. Gopel, "Ultimate limits in the miniaturization of chemical sensors", *sensors and actuators*, vol A 56, pp. 83-102, 1996.

[4] Committee on New Sensor Technologies: Materials and Applications, National Materials Advisory Board, Commission on Engineering and Technical Systems, National Research Council, "Expanding the vision of sensor materials", Washington, D.C.: National Academy Press, 1995.

[5] D. Rocklin, "Electrochemical detection", *A practical guide to HPLC detection*, edited by D. Parriott, San Diego, CA: Academic Press, Inc., 1992.

[6] W. Brattain and Bardeen, , *Bell System Technical J.*, vol. 32, p. 1, , 1953.

[7] S. R. Morrison, "Chemical sensors", *Semiconductor sensors*, edited by S. M. Sze, New York, USA: John Wiley & Sons, Inc. 1994.

[8] P. T. Moseley, A. M. Stoneham and D. E. Williams, "Oxide semiconductors: patterns of gas response behaviour according to material type", *Techniques and mechanisms in gas sensing*, edited by P. T. Moseley, J. Norris and D. E. Willams, Bristol, England: Adam Hilger, 1987.

[9] From Motorola sensor data sheet.

[10] B. Bott and S. C. Thorpe, "Metal phthalocyanine gas sensors", *Techniques and mechanisms in gas sensing*, edited by P. T. Moseley, J. Norris and D. E. Willams, Bristol, England: Adam Hilger, 1987.

[11] A. J. Crocker, "Metal-oxide-semiconductor gas sensors", *Techniques and mechanisms in gas sensing*, edited by P. T. Moseley, J. Norris and D. E. Willams, Bristol, England: Adam Hilger, 1987.

[12] I. Lundström and C. Svensson, "Gas-sensitive metal gate semiconductor devices", *Soild-state chemical sensors*, edited by J. Janata and R. J. Huber, New York, NY: Academic press, 1985.

[13] D. Blackwwod and M. Josowicz, "Work function and spectroscopic studies of interactions between condcting polymers and organic vapours", *J. Phys. Chem.*, vol. 95, pp. 493-502, 1991.

[14] I. Lundström, S. Shivaraman, C. Svensson and L. Lundkuist, "A hydrogen sensitive MOS field-effect transistor", *Appl. Phys. Lett.*, vol. 26, pp. 55-57, 1975.

[15] P. Bergveld, "Development of an ion-sensitive solid-state device for neurophysiological measurements", *IEEE Trans. Biomed. Eng.*, vol. 19, pp. 70-71, 1970.

[16] P. Bergveld, "Exploiting the dynamic properties of FET-based chemical sensors", *J. Phys. E.: Sci. Instum.*, vol. 22, pp. 678-683, 1989.

[17] M. J. Madou and S. R. Morrison, *Chemical sensing with solid state devices*, Boston, MA, USA: Academic Press Inc., 1989.

[18] J. W. Gardner, *Microsensors: Principle and Application*, Chichester, England: John Wiley & Sons, 1994.

[19] J. O. W. Norris, "Optical fiber gas sensing", *Techniques and mechanisms in gas sensing*, edited by P. T. Moseley, J. Norris and D. E. Willams, Bristol, England: Adam Hilger, 1987.

[20] C. G. Fox and J. F. Alder, "Surface acoustic wave sensors for atmospheric gas monitoring", *Techniques and mechanisms in gas sensing*, edited by P. T. Moseley, J. Norris and D. E. Willams, Bristol, England: Adam Hilger, 1987.

[21] R. R. Reston and E. S. Kolesar, "Silicon-micromachined gas chromatography system used to separate and detect ammonia and nitrogen dioxide-part i: design, fabrication, and integration of the gas chromatography system", *J. MEMS,* vol. 3, pp. 134-146, 1994.

[22] Private communication with Professor Mehrdad Saif, School of Engineering Science at Simon Fraser University, Burnaby BC.

[23] E. S. Kolesar and R. R. Reston, "Silicon-micromachined gas chromatography system used to separate and detect ammonia and nitrogen dioxide-part ii: evaluation, theoretical modeling of the gas chromatography system", *J. MEMS,* vol. 3, pp. 147-154, 1994.

[24] R. R. Reston, "Design and performance evaluation of a gas chromatograph micromachined in a single crystal silicon substrate", Ph.D. Dissertation, Air Force Institute of Technology, Wright-Patterson AFB, OH, 1993.

[25] M. G. Ingham and R. Z. Gomer, *Chem Phys*. vol. 22, pp. 1279-1280, 1954.

[26] M. J. Madau and S. R. Morrison, "High-field operation of submicrometer devices at atmospheric pressure", *Transducers '91*, pp. 145-149, 1991.

[27] C. A. Spindt, C. E. Holland and R. D. Stowell, "Recent progress in low-voltage field-emission cathode development", *Journal de Physique*, vol. 45, no. 12, pp. c9-269-c9-278, 1984.

[28] C. A. Spindt, "Microfabricated field-emission and field ionization source", *surface science*, vol. 266, pp. 145-154, 1992.

[29] L. H. Henrich, "Detectors and data handling", *Modern Practice of Gas Chromatography,* (Third Edition), edited by R. L. Grob, New York, NY: John Wiley & Sons, 1995.

[30] E. Sullivan, "Detectors Part I.", *Modern Practice of Gas Chromatography,* (Third Edition), edited by R. L. Grob, New York, NY: John Wiley & Sons, 1977.

[31] A. B. Littlewood, *Gas Chromatography: Principle, Techniques and Applications,* (Second Edition). New York, NY: Academic Press, 1970.

[32] B. M. Tissue, http://www.scim.edia.com/, 1996.

[33] J. C. Stenberg, "Detector devices for gas chromatography", *Gas chromatography,* edited by L. Fowler, London, England: Academic Press Inc., 1963.

[34] R. L. Grob, "Theory of gas chromatography", *Modern Practice of Gas Chromatography,* (Third Edition), edited by R. L. Grob, New York, NY: John Wiley & Sons, 1995.

[35] K. E. Kaissling and J. Thorson, "Receptors for neurotransmitters, hormones and pheromone in insects", D. B. Satelle *et al.* editors, Elsevier/North-Holland Biomedical Press, pp. 261-282, 1980.

[36] L. Wadhams, "The coupled gas chromatography - single cell recording technique", pp.179-189, in: H. E. Hummel and T. A. Miller (eds.) Techniques in Pheromone Research, Springer Verlag, 1984.

[37] B. Ghodsian, M. Syrzycki, G. Gries and M. Parameswaran, "Microelectromechanical probe for an integrated electroantennographic system", *IEEE Innovative Systems in Silicon*, Austin Texas, 9-11 October, pp. 89-97, 1996.

[38] M. J. Daneman, N. C. Tien, O. Solgaard, A. P. Pisano, K. Y. Lau, and R. S. Muller, "Linear microvibromotor for positioning optical components", *IEEE Conference on Micro Electro Mechanical Systems (MEMS '95)*, Amsterdam, January 29- February 2, pp. 7-12, 1995.

[39] W. C. Tang, T. -C. H. Nguyen, M. W. Judy, and R. T. Howe, "Electrostatic-comb drive of lateral polysilicon resonators", *Sensors and Actuators*, vol. A21-23, pp. 328-331, 1990.

[40] E. W. Müller and K. Bahadur, "Field ionization of gases at a metal surface and the resolution of the field ion microscope", *Physical Review*, vol. 102, no. 3, pp. 624-631, 1958.

[41] H. D. Beckey, *Principles of field ionization and field desorption mass spectrometry*, Elmsford, NY: Pergamon Press Inc., 1977.

[42] D. S. Boudreax and P. H. Cutler, "Theory of atom-metal interactions. I. application of quantum-mechanical collision theory to field-ionization process", *Physical Review*, vol. 149, no. 1, sepetember, pp.170-178, 1966.

[43] R. Gomer, "Work function in field emission. chemisorption", *J. Chem. Phy.*, vol. 21, no. 10, october, pp. 1869-1872, 1953.

[44] H. -R. Schulten, H. D. Beckey, E. M. Bessel, A. B. Foster, M. Jarman and J. H. Westwood, chem. comm., p. 416, 1973.

[45] M. J. Madau and S. R. Morrison, "High-field operation of submicrometer devices at atmospheric pressure", *International conference on Solid-State Sensors and Actuators (Transducers '91)*, San Francisco, June 25-29, pp. 145-149, 1991.

[46] C. A. Spindt, C. E. Holland and R. D. Stowell, "Recent progress in low-voltage field-emission cathode development", *Journal de Physique*, vol. 45, no. 12, pp. c9-269-c9-278, 1984.

[47] M. J. Madau and S. R. Morrison, *Chemical sensing with solid state devices*, San Diego, CA: Academic Press, Inc., 1989.

[48] S. R. Morrison, *Electrochemistry at Semiconductor and Oxidized Metal Electrodes*, New York, NY: Plenum Press, 1980.

[49] A. J. Bard and L. R. Faulkner, *Electrochemical Methods: Fundamentals and Applications*, New York, NY: Wiley, 1980.

[50] W. H. Ko and J. T. Suminto, "Semiconductor integrated circuit technology and micromachining", *Sensors: a comprehensive survey, volume 1: fundamentals and general aspects*, edited by W. Gopel, et al., New York, NY: VCH Publishers, Inc., 1989.

[51] R. Zengerle, S. Kluge, M. Richter, A. Richter, "A bidirectional silicon micro pump", *Proc. of IEEE MEMS workshop*, Amesterdam, January 29-February 2, pp. 19-24, 1995.

[52] A. D. Johnson and E. Shahoian, "Recent progress in thin film shape memory microactuators", *Proc. of IEEE MEMS workshop*, Amesterdam, January 29-February 2, pp. 216-220, 1995.

[53] F. Rudolf, "A micromechnical capacitive accelerometer with a two-point inertial-mass suspension", Sensors and Actuators, vol. 4, pp. 191-198, 1982.

[54] E. Stemme, J. Ekelof and L. Nordin, "Measuring liquid density with a tuning fork transducer", *IEEE Trans. Instrumentation and Measurement*, vol. 32, pp. 432-437, 1983.

[55] C. S. Sander, J. W. Knutti and J. D. Meindle, "A monolithic capacitive pressure sensor with pulse-periode output", *IEEE Trans. ED*, vol. 17, pp. 927-930, 1980.

[56] J. V. Hatfield, D. Lomas, J. Goldfinch, P. J. Hicks and J. Comer, "An intergrated multi-channel charged particle sensing system", *Transducers 95*, Stokholm, June 25-29, pp. 152-155, 1995.

[57] M. Mehregany, "Microfabricated silicon electric mechanisms", Ph. D. Thesis, MIT, Cambridge, MA, May 1990

[58] K. Tanaka, Y. Mochida and S. Sugimoto, "A micromachined vibrating gyroscope", *Proc. of IEEE MEMS workshop*, Amesterdam, January 29-February 2, pp. 216-220, 1995.

[59] B. Ghodsian, J. Chen, M. Parameswaran and M. Syrzycki, "Towards an integrated sub-nanogram mass measurements system", *IEEE Innovative Systems in Silicon*, Austin Texas, 9-11 October, pp. 71-80, 1996.

[60] R. Williams, *Modern GaAs processing methods*, Boston, MA: Artech House Inc., 1990.

[61] K. E. Petersen, "Silicon as a mechanical material", Proc. IEEE, vol. 70, pp. 420-457, 1982.

[62] W. S. Ruska, *Microelectronic processing: an introduction to manufacturing of integrated circuits*, New York, NY: McGraw-Hill Book Company, 1987.

[63] F. Shimura, *Semiconductor Silicon Crystal Technology*, San Diego, CA: Academic Press, Inc., 1989.

[64] S. M. Sze, *Semiconductor Devices: Physics and Technology*. New York, NY: John Wiley & Sons, 1985.

[65] R. M. Finne and D. L. Klein, "A water-amine-complexing agent system for etching silicon", *J. Electrochem. Soc.*, vol. 114, pp. 965-970, 1967.

[66] H. Seidel, L. Csepregi, A. Heuberger and H. Baumgartel, "Anisotropic etching of crystalline silicon in alkaline solutions, I. orientation dependence and behavior of passivation layers", *J. Electrochem. Soc.*, vol. 137, pp. 3616- , 1990.

[67] D. B. Lee, "Anisotropic etching of silicon of silicon", *Journal of Applied Physics*, vol. 40, no.?, pp. 4569-?, 1969.

[68] H. Muraoka and T. Y. Sumitomo, "Controlled preferential etching technology", in *Semiconductor Silicon*, ed. H. R. Huff and R. R. Burgess, The Electrochemical Society, vol. ?, no. ?, pp. 327-?, 1973.

[69] K. D. Bean, "Anisotropic etching of silicon", *IEEE Trans. ED*, vol. 25, no. ?, pp. 1185-1193, 1978.

[70] A. Reisman, M. Berkenbilt, S. A. Chan, F. B. Kaufman and D. C. Green, "The controlled etching of silicon in catalyzed ethylenediamine-pyrocatechol-water solution", *Journal of Electrochemical Society*, vol. 126, pp. 1406-1415, 1979.

[71] M. P. Wu, Q. H. Wu and W. H. Ko, "A study on deep etching of silicon using ethylenediamine-pyrocatechol-water", *Sensors and Actuators*, vol. 9, pp. 333-343, 1986.

[72] O. Tabata, R. Asahi, H. Funabashi and S. Sugiyama, "Anisotropic etching of silicon in $(CH_3)_4NoH$ solutions", *International conference on Solid-State Sensors and Actuators (Transducers '91)*, San Francisco, June 25-29, pp. 811-814, 1991.

[73] U. Schnakenberg, W. Benecke and P. lange, "TMAHW etchants for silicon micromachining", *International conference on Solid-State Sensors and Actuators (Transducers '91)*, San Francisco, June 25-29, pp. 815-818, 1991.

[74] M. Declercq, L. Gerzberg and J. Meinol, "Optimization of the hydrazine-water solution for anisotropic etching silicon in integrated circuit technology", *Journal of Electrochemical Society*, vol. 122, p. 545, 1975.

[75] A. I. Stoller, "The etching of deep, vertical walled patterns of silicon", *RCA Rev.*, vol. 31, p. 271, 1970.

[76] D. L. Kendall, "On etching very narrow grooves in silicon", *Appl. Phys. Lett.*, vol. 26, p. 195, 1975.

[77] X. P. Wu and W. H. Ko, "A study on compensating corner undercutting in anisotropic etching of (100) silicon", *Transducers 1987*, Tokyo, p.126, 1987.

[78] L. D. Clark, Jr., J. L. Lund and D. J. Edell, "Cesium hydroxide (CsOH): a useful etchant for micromachining silicon", *Tech. Digest, IEEE Solid State Sensor and Actuator Worksho*p, Hilton Head Island, SC, pp.5-?, 1988.

[79] H. Seidel, "The mechanism of anistropic silicon etching and its relevance for micromachining", *Tech. Digest, IEEE Solid State Sensor and Actuator Worksho*p, Hilton Head Island, SC, pp. 86-91, 1990.

[80] H. Miyajima and M. Mehregany, "High-aspect-ratio photolithography for mems applications", *J. MEMS*, vol. 4, no. 4, pp. 220-229, 1995.

[81] A. B. Frazier and M. G. Allen, "Metallic microstructures fabricated using photosensitive polyimide electroplating molds", *J. MEMS*, vol. 2, no. 2, 1993.

[82] J. Gobet, F. Cardot, J. Bergqvist and F. Rudolf, "Electrodeposition of 3D microstructures on silicon, "*J. Micromech. Microeng.*, vol. 3, p. 123, 1993.

[83] J. W. Judy, R. S. Muller and H. H .Zappe, "Magnetic microactuation of polysilicon flexure structures", *J. of MEMS*, vol. 4, no. 4, pp. 162-169, 1995.

[84] W. H. Ko, "Bonding techniques for microsensors", *Micromachining and Micropackaging of Transducers*, edited by D. F. Clifford, *et al.*, The Netherlands: Elsevier Science Publishers, 1985.

[85] A. Brener, *Electrodeposition of Alloys*, New York, NY: Academic Press, 1963.

[86] J. W. Judy, "Magnetic microactuators with polysilicon flexures", M.Sc. Research Project, University of California at Berkeley, CA, 1994.

[87] B. Ghodsian, M. Parameswaran, M. Syrzycki and N. Tait, "Fabrication of affordable metallic microstructures by electroplating and photoresist molds", *Canadian Conf. on Electrical and Computer Engineering*, Calgary, 26-29 May, pp. 68-71, 1996.

[88] W. Ehfeld, P. Bley, F. Götz, P. Hagmann, A. Maner, J. Moher, H. O. Moser, D. Münchmeyer, W. Schelb, D. Schmidt and E. W. Becker, "Fabrication of microstructures using the LIGA process", *Proc. IEEE Micro Robots and Teleoperators Workshop*, Hyannis, MA, Nov. 1987.

[89] B. Ghodsian, M. Parameswaran and M. Syrzycki, "Simple technology for fabricating micromechanical 3D structures using electroplating without photoresist mold", *SPIE's Symp. on Micromach. and Microfab.*, Austin, Texas, 14-15 October, vol. 2832, pp. 194-203, 1996.

[90] M. A. Brimi and J. R. Luck, *Electrofinishing*, New York, NY: American Elsevier Publishing Company Inc., 1965.

[91] ATHENA user's manual, 2D process simulation software, SILVACO International, version 3.0, June, 1995, USA.

[92] H. Z. Massoud, "Thermal oxidation of silicon in dry oxygen-growth kinetics and charge characterization in the thin Regime", Ph.D. dissertation, Stanford University, 1993.

[93] Bruce E. Deal, *J. Electrochem. Soc.*, vol. 25, p. 576, 1978.

[94] K. L. Jensen, E. G. Zaidman, M. A. Kodis, B. Goplen and D. N. Smithe, "Analytical and semi numerical models for gated field emitter arrays. I. theory", *J. Vac. Sci. Technol.*, B 14(3), pp. 1942-1951, 1996

[95] Private communication with Dr. J. Akido from MEL, Japan.

[96] R. S. Smith, L. E. Godycki and J. C. Lloyd, "Effects of saccharin on the structural and magnetic properties of iron-nickel films", *Journal of The Electrochemical Society*, vol. 108, no. 10, pp. 996-998, 1961.

[97] S. C. Terry, J.H.Jerman and J.B.Angell, "A gas chromatographic air analyzer fabricated on silicon wafer", *IEEE-ED*, vol. 26, no. 12, 1979.

[98] C. A. Spindt, "A thin-film field-emission cathode", *J. Appl. Phys.*, vol. 39, No. 7, pp. 3504-3505, 1968.

[99] C. A. Spindt, K. R. Shoulders and L. N. Heynick, "Field emission cathode structures and devices utilizing such structures", *U.S. Patent 3755704*, 1973.

[100] A. Wistsora-at, W. P. kang, J. L. Davidson, M. Howell, Q. Li, J. F. Xu and D. V. Kerns, "Gated diamond field emitter array with ultra low operating voltage and high emission current", *Device Research Conference*, Colorado, June, pp 150-151, 1997.

[101] C. A. Spindt, L. N. Heynick, "Field ionizer and field emission cathode structures and methods of production", *U.S. Patent 3665241*, 1972.

[102] W. Orvis, D. Ciarlo, C. McConaghy, J. Yee, E. Hee, C. Hunt and J. Trujillo, "A progress report on the livermore miniature vacuum tube project", *in IEDM Tech. Dig.*, pp. 529-532, 1989.

[103] R. B. Marcus, T. Ravi, T. Gmitter, K. Chin, D. Liu, W. Orvis, D. Ciarlo, C. Hunt and J. Trujillo, "Formation of atomically sharp silicon needles" *in IEDM Tech. Dig.*, pp. 884-886, 1989.

[104] S. M. Zimmerman and W. T. Babie, "A fabrication method for the integration of vacuum microelectronic devices", *IEEE-ED*, vol. 38, no. 10, pp. 2294-2303, 1991.

[105] S. M. Zimmerman, "Structure and processes for fabricating field emission cathode tips using secondary cusp", *U.S. Patent 5334908*, 1994.

[106] Jensen et al., "Analytical and semi numerical models for gated field emitter arrays. I. theory", *J. Vac. Sci. Technol.*, vol. B 14, no. 3, 1996.

[107] B. Ghodsian, M. Parameswaran and M. Syrzycki, "Gas detector with Low-Cost Micromachined Field Ionization Tips", *submitted to IEEE-ED*, MS# JB97051, September 1997.

[108]B. Ghodsian, M. Parameswaran and M. Syrzycki, "Low-Cost Methods for Manufacturing Field Ionization and Emission Structures with Self-Aligned Gate Electrodes", US Patent pending, September 1997.

[109]S. K. Gandhi, "*VLSI fabrication principles*", John Wiley and Sons, New York, USA, 1983.

[110]R. B. Marcus and T. T. Sheng, "The oxidation of shaped silicon surfaces", J. *Electrochem. Soc. Solid State Science & Tech.*, pp.1278-1282, June 1982.

[111]B. Ghodsian, M. Parameswaran and M. Syrzycki, "Low-cost micromachined field ionization tips for an integrated gas detector", submitted to *Sensors and Actuators*, MS# , (September 1997).

[112]A. E. O'Keeffe and G. C. Ortman, "Primary standards for trace gas analysis", *Analytical Chemistry*, vol. 38, no. 6, pp.760-763, 1966.

[113]F. P. Scaringelli, A. E. O'Keeffe, E. Rosenberg and J. P. Bell, "Preparation of known concentrations of gases and vapors with permeation devices calibrated gravimetrically", *Analytical Chemistry*, vol. 42, no. 8, pp.760-763, 1970.

[114]*Student edition of MATLAB, user's guide*, Englewood Cliffs,NY: Prentice Hall, 1995.

[115]*MATLAB high-performance numeric computation and visualization software, reference guide*, Englewood Cliffs, NY: Prentice Hall, 1992.